



SAIMM

THE SOUTHERN AFRICAN INSTITUTE
OF MINING AND METALLURGY

VOLUME 120 NO. 6 JUNE 2020

Mining Africa's Experts

Get a clear perspective of your mining needs from mine to market and pit to port.

#WeDoMining
www.ukwazi.co.za



UKWAZI
we do mining

More than just words

W E D O

M I N I N G

From

A - Z

Our expert team can advise you every step of the way from independent advisory services, onsite technical support, digital systems integration and contract mining operations across the mining value chain.

Your mining technical and execution partner.
www.ukwazi.co.za

UKWAZI
we do mining

CONNECT WITH US ON



OFFICE BEARERS AND COUNCIL FOR THE 2019/2020 SESSION

Honorary President

Mxolisi Mgojo
President, Minerals Council South Africa

Honorary Vice Presidents

Gwede Mantashe
Minister of Mineral Resources, South Africa

Ebrahim Patel
Minister of Trade and Industry, South Africa

Blade Nzimande
Minister of Science and Technology, South Africa

President

M.I. Mthenjane

President Elect

V.G. Duke

Senior Vice President

I.J. Geldenhuys

Junior Vice President

Z. Botha

Incoming Junior Vice President

W.C. Joughin

Immediate Past President

A.S. Macfarlane

Co-opted to Office Bearers

S. Ndlovu

Honorary Treasurer

V.G. Duke

Ordinary Members on Council

B. Genc	S.M Rupprecht
W.C. Joughin	N. Singh
G.R. Lane	A.G. Smith
E. Matinde	M.H. Solomon
G. Njowa	A.T. van Zyl
B. Ntsoelengoe	E.J. Walls

Co-opted Members

T. Makgala R.C.W. Webber-Youngman

Past Presidents Serving on Council

N.A. Barcza	J.L. Porter
R.D. Beck	S.J. Ramokgopa
J.R. Dixon	M.H. Rogers
H.E. James	D.A.J. Ross-Watt
R.T. Jones	G.L. Smith
C. Musingwini	W.H. van Niekerk
S. Ndlovu	

G.R. Lane-TPC Mining Chairperson
Z. Botha-TPC Metallurgy Chairperson

G. Dabula-YPC Chairperson
S. Manjengwa-YPC Vice Chairperson

Branch Chairpersons

Botswana	Vacant
DRC	S. Maleba
Johannesburg	D.F. Jensen
Namibia	N.M. Namate
Northern Cape	F.C. Nieuwenhuys
Pretoria	S. Uludag
Western Cape	A.B. Nesbitt
Zambia	D. Muma
Zimbabwe	C.P. Sadomba
Zululand	C.W. Mienie

PAST PRESIDENTS

*Deceased

* W. Bettel (1894-1895)	* M. Barcza (1958-1959)
* A.F. Crosse (1895-1896)	* R.J. Adamson (1959-1960)
* W.R. Feldtmann (1896-1897)	* W.S. Findlay (1960-1961)
* C. Butters (1897-1898)	* D.G. Maxwell (1961-1962)
* J. Loevy (1898-1899)	* J. de V. Lambrechts (1962-1963)
* J.R. Williams (1899-1903)	* J.F. Reid (1963-1964)
* S.H. Pearce (1903-1904)	* D.M. Jamieson (1964-1965)
* W.A. Caldecott (1904-1905)	* H.E. Cross (1965-1966)
* W. Cullen (1905-1906)	* D. Gordon Jones (1966-1967)
* E.H. Johnson (1906-1907)	* P. Lambooy (1967-1968)
* J. Yates (1907-1908)	* R.C.J. Goode (1968-1969)
* R.G. Bevington (1908-1909)	* J.K.E. Douglas (1969-1970)
* A. McA. Johnston (1909-1910)	* V.C. Robinson (1970-1971)
* J. Moir (1910-1911)	* D.D. Howat (1971-1972)
* C.B. Saner (1911-1912)	* J.P. Hugo (1972-1973)
* W.R. Dowling (1912-1913)	* P.W.J. van Rensburg (1973-1974)
* A. Richardson (1913-1914)	* R.P. Plewman (1974-1975)
* G.H. Stanley (1914-1915)	* R.E. Robinson (1975-1976)
* J.E. Thomas (1915-1916)	* M.D.G. Salamon (1976-1977)
* J.A. Wilkinson (1916-1917)	* P.A. Von Wielligh (1977-1978)
* G. Hildick-Smith (1917-1918)	* M.G. Atmore (1978-1979)
* H.S. Meyer (1918-1919)	* D.A. Viljoen (1979-1980)
* J. Gray (1919-1920)	* P.R. Jochens (1980-1981)
* J. Chilton (1920-1921)	* G.Y. Nisbet (1981-1982)
* F. Wartenweiler (1921-1922)	* A.N. Brown (1982-1983)
* G.A. Watermeyer (1922-1923)	* R.P. King (1983-1984)
* F.W. Watson (1923-1924)	* J.D. Austin (1984-1985)
* C.J. Gray (1924-1925)	* H.E. James (1985-1986)
* H.A. White (1925-1926)	* H. Wagner (1986-1987)
* H.R. Adam (1926-1927)	* B.C. Alberts (1987-1988)
* Sir Robert Kotze (1927-1928)	* C.E. Fivaz (1988-1989)
* J.A. Woodburn (1928-1929)	* O.K.H. Steffen (1989-1990)
* H. Pirow (1929-1930)	* H.G. Mosenthal (1990-1991)
* J. Henderson (1930-1931)	* R.D. Beck (1991-1992)
* A. King (1931-1932)	* J.P. Hoffman (1992-1993)
* V. Nimmo-Dewar (1932-1933)	* H. Scott-Russell (1993-1994)
* P.N. Lategan (1933-1934)	* J.A. Cruise (1994-1995)
* E.C. Ranson (1934-1935)	* D.A.J. Ross-Watt (1995-1996)
* R.A. Flugge-De-Smidt (1935-1936)	* N.A. Barcza (1996-1997)
* T.K. Prentice (1936-1937)	* R.P. Mohring (1997-1998)
* R.S.G. Stokes (1937-1938)	* J.R. Dixon (1998-1999)
* P.E. Hall (1938-1939)	* M.H. Rogers (1999-2000)
* E.H.A. Joseph (1939-1940)	* L.A. Cramer (2000-2001)
* J.H. Dobson (1940-1941)	* A.A.B. Douglas (2001-2002)
* Theo Meyer (1941-1942)	* S.J. Ramokgopa (2002-2003)
* John V. Muller (1942-1943)	* T.R. Stacey (2003-2004)
* C. Biccard Jeppe (1943-1944)	* F.M.G. Egerton (2004-2005)
* P.J. Louis Bok (1944-1945)	* W.H. van Niekerk (2005-2006)
* J.T. McIntyre (1945-1946)	* R.P.H. Willis (2006-2007)
* M. Falcon (1946-1947)	* R.G.B. Pickering (2007-2008)
* A. Clemens (1947-1948)	* A.M. Garbers-Craig (2008-2009)
* F.G. Hill (1948-1949)	* J.C. Ngoma (2009-2010)
* O.A.E. Jackson (1949-1950)	* G.V.R. Landman (2010-2011)
* W.E. Gooday (1950-1951)	* J.N. van der Merwe (2011-2012)
* C.J. Irving (1951-1952)	* G.L. Smith (2012-2013)
* D.D. Stitt (1952-1953)	* M. Dworzanowski (2013-2014)
* M.C.G. Meyer (1953-1954)	* J.L. Porter (2014-2015)
* L.A. Bushell (1954-1955)	* R.T. Jones (2015-2016)
* H. Britten (1955-1956)	* C. Musingwini (2016-2017)
* Wm. Bleloch (1956-1957)	* S. Ndlovu (2017-2018)
* H. Simon (1957-1958)	* A.S. Macfarlane (2018-2019)

Honorary Legal Advisers

Scop Incorporated

Auditors

Genesis Chartered Accountants

Secretaries

The Southern African Institute of Mining and Metallurgy

Fifth Floor, Minerals Council South Africa

5 Holland Street, Johannesburg 2001 • P.O. Box 61127, Marshalltown 2107

Telephone (011) 834-1273/7 • Fax (011) 838-5925 or (011) 833-8156

E-mail: journal@saimm.co.za

Editorial Board

S. Bada
R.D. Beck
P. Den Hoed
P. Dikgwatlhe
L. Falcon
B. Genc
R.T. Jones
W.C. Joughin
A. Kinghorn
D.E.P. Klenam
H. Lodewijks
F. Malan
R. Mitra
C. Musingwini
S. Ndlovu
P. Neingo
S. Nyoni
N. Rampersad
S. Rupprecht
K. Sole
T.R. Stacey

Editorial Consultant

R.M.S. Falcon

Typeset and Published by

The Southern African Institute of Mining and Metallurgy
P.O. Box 61127
Marshalltown 2107
Telephone (011) 834-1273/7
Fax (011) 838-5923
E-mail: journal@saimm.co.za

Printed by

Camera Press, Johannesburg

Advertising Representative

Barbara Spence
Avenue Advertising
Telephone (011) 463-7940
E-mail: barbara@avenue.co.za

ISSN 2225-6253 (print)

ISSN 2411-9717 (online)



Directory of Open Access Journals



THE INSTITUTE, AS A BODY, IS NOT RESPONSIBLE FOR THE STATEMENTS AND OPINIONS ADVANCED IN ANY OF ITS PUBLICATIONS.

Copyright © 2020 by The Southern African Institute of Mining and Metallurgy. All rights reserved. Multiple copying of the contents of this publication or parts thereof without permission is in breach of copyright, but permission is hereby given for the copying of titles and abstracts of papers and names of authors. Permission to copy illustrations and short extracts from the text of individual contributions is usually given upon written application to the Institute, provided that the source (and where appropriate, the copyright) is acknowledged. Apart from any fair dealing for the purposes of review or criticism under **The Copyright Act no. 98, 1978, Section 12**, of the Republic of South Africa, a single copy of an article may be supplied by a library for the purposes of research or private study. No part of this publication may be reproduced, stored in a retrieval system, or transmitted in any form or by any means without the prior permission of the publishers. **Multiple copying of the contents of the publication without permission is always illegal.**

U.S. Copyright Law applicable to users in the U.S.A.

The appearance of the statement of copyright at the bottom of the first page of an article appearing in this journal indicates that the copyright holder consents to the making of copies of the article for personal or internal use. This consent is given on condition that the copier pays the stated fee for each copy of a paper beyond that permitted by Section 107 or 108 of the U.S. Copyright Law. The fee is to be paid through the Copyright Clearance Center, Inc., Operations Center, P.O. Box 765, Schenectady, New York 12301, U.S.A. This consent does not extend to other kinds of copying, such as copying for general distribution, for advertising or promotional purposes, for creating new collective works, or for resale.



SAIMM

JOURNAL OF THE SOUTHERN AFRICAN INSTITUTE OF MINING AND METALLURGY

VOLUME 120 NO. 6 JUNE 2020

Contents

Journal Comment

by R.L. Paul iv

President's Corner: Lessons from 'rona'

by M.I. Mthenjane v-vi

STUDENT PAPERS

Identification of suitable areas for multi-reef operation at Thorncliffe Chrome Mine

L.L. Mthembu and L.D. Meyer 355

This paper focuses on identifying viable areas within the Middle Group Chromitite No.2 layer at Thorncliffe Mine that adheres to mining, geological, and rock engineering parameters for a safe multiple-reef operation, and establishing efficient ways of accessing and extracting the MG2 layer. It can be concluded that the MG2 layer can be mined viably in a safe manner along with the MG1 layer in a multi-reef environment.

An investigation into the permeability of a PGM slag freeze lining to sulphur

H. Steenkamp and A.M. Garbers-Craig 361

The aim of this study was to investigate the role of the freeze lining in the migration of sulphur to the copper cooler in a PGM smelter. This was done by measuring the permeability of gas through magnesia-chromite and graphite bricks, as well as through freeze lining samples. In order to form a freeze lining with optimum characteristics, furnace conditions must be controlled in such a way as to form a freeze lining with a thick, dense cold face with minimal pores. Furthermore, temperature fluctuations in the furnace must be avoided as they can result in the formation of cracks in the freeze lining, through which sulphur can penetrate.

Characterization of surface roughness and subsurface pores and their effect on corrosion in 3D-printed AlSi10Mg

S. Thuketana, C. Taute, H. Möller, and A. du Plessis. 369

The practicality of using additive manufacturing (AM) for industrial applications, considering its unique defects, was questioned. To investigate this, defects (surface roughness and porosity) associated with AlSi10Mg parts produced by laser powder-bed fusion were characterized. Smooth, polished samples were found to experience more corrosion than unpolished samples. Laser shock peening is suggested as a possible solution.

International Advisory Board

R. Dimitrakopoulos, McGill University, Canada
D. Dreisinger, University of British Columbia, Canada
M. Dworzanowski, Consulting Metallurgical Engineer, France
E. Esterhuizen, NIOSH Research Organization, USA
H. Mitri, McGill University, Canada
M.J. Nicol, Murdoch University, Australia
E. Topal, Curtin University, Australia
D. Vogt, University of Exeter, United Kingdom



STUDENT PAPERS (CONTINUED)

- On the interactions of iron sulphide with alumina and silica**
R.K. Hlongwa, B.M. Thethwayo, and A.F. Mulaba-Bafubiandi 377
- The supposition that matte will react with only certain constituents of the refractory brick, as opposed to the entire brick, was tested by observing the extent of reaction of iron sulphide (FeS) with silica (SiO₂) and alumina (Al₂O₃). One of the aims was to identify the component of the refractory brick that is most reactive towards matte. The postulation that brick constituents may individually be reactive towards matte was proven to be true.*

PAPERS OF GENERAL INTEREST

- Practical considerations in the modelling of resin-grouted rockbolts**
P. Tomasone, N. Bahrani, and J. Hadjigeorgiou 385
- Numerical models are widely used to demonstrate the effect of ground support in stabilizing underground excavations in rock. However, limited attention has been paid to the reliability of the employed models. This paper focuses on the simulation of resin-grouted rebar rockbolts to illustrate the sensitivity of numerical models to the stiffness of reinforcement elements, derived from in-situ pull tests.*
- The development of a time-based probabilistic sinkhole prediction method for coal mining in the Witbank and Highveld coalfields**
J.N. van der Merwe 393
- The paper describes the development of a method to predict the occurrence of sinkholes due to mining, caused by the progressive collapse of underground openings. If the top of the cavity reaches or extends beyond the base of weathering, sinkhole development is likely. Progression of the collapse may be terminated by various means, including the presence of a strong layer between the mining horizon and the base of the weathered material. The likelihood of failure of the strong layers is evaluated as a probability of failure over time. The end result is a method on which to base the probability of sinkhole occurrence with respect to time.*

Journal
Comment



‘It was the best of times, it was the worst of times, it was the age of wisdom, it was the age of foolishness, it was the epoch of belief, it was the epoch of incredulity, it was the season of Light, it was the season of Darkness, it was the spring of hope, it was the winter of despair, we had everything before us, we had nothing before us ...’ – the opening lines to *A Tale of Two Cities* (1859) by Charles Dickens. And I say Amen to that!

Those words written 161 years ago resonate across nations as we struggle against the COVID-19 pandemic and a ravaged world economy. Gold and palladium at record levels – coal and zinc bottoming. Lives or livelihoods – I would not like to be the decision-maker having to choose between these options in South Africa with 14 mineworkers having died from COVID-19, and with nearly 3000 cases within the sector having been recorded at the time of writing. It is apparent that the balance, even in the world’s wealthiest countries, has tipped in favour of livelihoods over lives.

My heart says that this decision is insensitive to the pain of families who have lost a cherished parent or grandparent, or have to confront the anguish of entering the workplace and worrying about the risk of infection, but my brain says the alternative is no better. Without going back to work and earning money to buy food, many will face the spectre of malnutrition affecting the youngest and weakest within their families. A similar dilemma is facing us regarding the reopening of schools and universities. Opening will spread the virus, but remaining closed will produce a generation of deprived students who will struggle to catch up – probably for the rest of their lives. Hoping that home schooling or online learning are viable alternatives ignores the fact that these options are really open only to families with well-educated parents and/or with the financial means to purchase electricity, computers, and bandwidth, and will inevitably perpetuate and grow existing inequalities in our society.

This copy of the *Journal* is the Student Edition, containing the research output of students completing their final year of their chosen engineering course at local universities in both mining and metallurgical disciplines. Of the seven papers, three are on mining topics, and four on metallurgical topics, and there is no common theme among the papers. As members of the SAIMM, we can take some pleasure in reading the student papers in this copy of the *Journal* and feeling that the human resource capability required to sustain the mining industry is already in the making. I therefore encourage you to read the papers, or at least the abstracts, to get some feel for the research currently being undertaken at our universities. The research, though published in this copy of the *Journal*, was completed last year. Given the pandemic and its impact on the student body, I can only hope that we have sufficient papers this time next year to continue the tradition of issuing a Student Edition!

Five of the papers originate from the universities of Johannesburg, Pretoria, and the Witwatersrand, one from North West, and one from Stellenbosch. I don’t place any significance on this finding, as the distribution tends to vary significantly from year to year, depending upon the student body in that year and the selections made on where to publish their papers. I mention this only because I studied at the University of Natal, Durban (now the University of KZN), and I was hoping to see a paper from my alma mater. In my student years, the late 1960s and early 1970s, the departments of Chemistry and Chemical Engineering were positioned side-by-side, and were the last buildings on the south side of the campus before descending to Logan’s bookshop.

The Department of Chemistry, where I studied and graduated with my PhD, has since relocated to the Westville campus. The first-year chemistry course, and a small part of the second-year course, was shared by both departments, so I had many friends in engineering. Most left after 4 years, but I continued my loose association with engineering as I became a laboratory demonstrator for the first- and second-year engineering students in the chemical laboratories. I have since met many of those students who remembered the generally disliked three-hour laboratory afternoons, and recalled that I was intimidating as I stalked the benches looking over their shoulders at their mostly inept attempts to master practical chemistry. Really, me? – Never, you must be confusing me with someone else!!

The Department of Chemical Engineering was dominated at that time by two giants of South African academia and metallurgy: Professor Peter King and Professor Ted Woodburn. I knew of them by reputation only at that time, but I had the pleasure of meeting them later on many occasions in ‘real life’. I would like to quote an extract written by Professor Mike Moys of Wits (but a postgraduate student at Durban around that time): ‘They supported and competed intensely. Allow me to reminisce briefly about Ted. Ted would arrive in the morning in his Mini Minor. Those of you who knew Ted – a very large man – can imagine Ted extricating himself from the Mini! Ted’s other idiosyncrasy was his habit of management by walking around chewing his tie. Ted also had a remarkable laugh which defies description and echoed through the building every now and then. Peter kept his cool!’

Memories linger, and some seem to become more vivid with the passage of time. As Dickens wrote: ‘It was the best of times ...’, or that was what I recall from my student days. Does anyone else remember those days in Durban, or am I alone with these memories? Is it not human nature that our youth was always the best of times? But will this still apply to today’s students growing up in the midst of the COVID-19 pandemic? Perhaps to them, in years from now, looking back, ‘it was the worst of times’. I hope not!

R.L. Paul



Lessons from 'rona'



As the first week of June 2020 approached, the 'R' word had adapted to a more positive form with the 'Recession of Lockdowns' in many countries around the world – the number of coronavirus ('rona') infections were beginning to slow down and so the curves were flattening and lockdowns being lifted. However, South Africa, despite the increasing number of infections (as more people were being tested), moved from level 4 to level 3 in terms of the National Disaster Act, driven by the need to alleviate the effects of the lockdown on economic activity.

As we emerged, hesitantly, from the frustrations of self-imposed isolation into a semblance of normality and greater mobility, I reflected on the many webinars that I listened to and asked myself the question – what lessons have I learnt? Quite a few, and I've captured them into five distinct messages for this letter.

Before laying out the lessons, let me set the context with a quote from a book that I'm restarting¹ to read: '... creating community, the most valuable form of social capital – the intimate, supportive relationships that spur collaboration while deeply satisfying our human need for connection, belonging and meaning'. Otherwise put, 'a life-long community of colleagues, contacts, friends, and mentors social science research tells us

that satisfying these relational needs isn't just about some soft notion of "the good life"; these are the hard prerequisites for creativity, innovation, progress – and, at the end of that chain, profit.'²

The excerpt provides a backdrop and reference for key human traits that we at times take for granted. These are the traits which, in my humble view, have been temporarily suspended by the presence of 'rona' in our lives.

Thus, the first lesson from 'rona' was the imperative of our time: to safeguard lives and livelihoods. In the absence of a vaccine, adhering to appropriate protocols to ensure safety and hygiene is our only chance of preventing further infections and transmission of the disease. The ability of people to live normal lives has been shattered as if by the force of Thor's hammer. It is *public, private, and civil society leadership*, in an unprecedented response, that has been carrying these imperatives, high above the shoulders, in either hand – the balance maintained while we trudge towards a vaccine will determine the 'new normal'.

The pandemic is described firstly as a humanitarian crisis and secondly an economic disaster. The former arises from the extent of devastation on the poor and destitute; the inadequacy of health facilities and potential increase in poverty and inequality. However, the response to these challenges was amazing. The unbounded combined action to save lives has never been witnessed on this scale and depth in South Africa. This brought to mind the second lesson and confirmed that *life is a value* – we have realized what matters most, *viz.*, safety and health, wellbeing, love and care for ourselves and others ... all the emotional and mushy stuff that we often forget about.

¹This is this common ... right?

²Excerpt from 'Never Eat Alone ... and Other Secrets to Success, One Relationship at a Time'. Keith Ferrazzi and Tahl Raz., Penguin Random House.

Lessons from ‘rona’ (continued)

At the same time, we must show care for what we have become and created as a society, the economy – our livelihoods and source of purpose. This creates the connections beyond family, gives us hope, and it is where innovation happens and where we seek fulfilment because what we do in this realm makes a difference – not only to our own lives, but to others’ lives too. ‘Rona’ has been the sobering antithesis to this life experience.

Now enter lesson number three – *politics are the other side to the economy on the social coin*, and therefore one cannot exist and act without the other. A thriving economy makes for political gain and the economic recession expected for the balance of 2020 and into 2021 will make for interesting politics over the next twelve to twenty-four months, both domestically and in several other countries around the globe.

Then there was the lesson of *what the new normal may look like*. While we await a viable vaccine to be found, we will need to learn to live with ‘rona’. An interesting lesson from Wuhan, the epicentre of the virus, is how the population has been colour-coded into red, amber, and green depending on the extent of exposure to the virus, which then determined the degree of mobility allowed by the state. Enter the surveillance society, where with the use of technology our every movement will be monitored, for better or for worse. Further, given the unprecedented levels of stimulus funding provided, the role of government in markets will be different, but how different only time will tell. Business will be a more active and responsive participant in society to address key issues, *viz*:

- An inclusive approach to economic development that ensures a meaningful reduction in inequality. Pay parity will become an area of public scrutiny; co-investment in infrastructure that enables greater mobility and reduces the cost of living, to name a few. Business will be judged by its impact in a way that changes lives.
- ‘Rona’ has elevated the urgency for response to climate change – the cumulative and systemic impacts from climate change and ‘rona’ demand a coordinated regional and global response. ‘Rona’ has demonstrated the ability for collaboration, which will be expected in relation to climate action.
- The tech race will intensify, but all participants will win. Based on the coordination and cooperation witnessed in response to ‘rona’, technical collaboration should enable developing nations to transcend current challenges and progress for the benefit of their citizens.

Lastly, I believe we are moving towards *an era of increasing engagement* because of a combination of the factors that I’ve described earlier, such as the state of the fiscus and debt troubles faced by governments post the lockdowns, the recessionary state of the global economy and social consequences, and policy response and effectiveness to manage economies out of the economic trough. Government or business cannot manage this situation individually. For our society to emerge strong from the effects of the lockdown, the acknowledged imperative of safeguarding lives and livelihoods must persist. Leadership from the public and private sector, with the support of civil society, must strengthen even further to build a foundation of trust amongst these social players and in society in general, which will then provide for better collaboration.

M.I. Mthenjane
President, SAIMM



Identification of suitable areas for multi-reef operation at Thorncliffe Chrome Mine

L.L Mthembu^{1*} and L.D. Meyer¹

*Paper written on project work carried out in partial fulfilment of B.Eng (Mining Engineering) degree

Affiliation:

¹Department of Mining Engineering, University of Pretoria, South Africa.

Correspondence to:

L.L Mthembu

Email:

u15360319@tuks.co.za

Dates:

Received: 30 Nov. 2019

Revised: 4 Jun. 2020

Accepted: 7 Jul. 2020

Published: June 2020

How to cite:

Mthembu, L.L and Meyer, L.D.
Identification of suitable areas for multi-reef operation at Thorncliffe Chrome Mine.
The Southern African Institute of Mining and Metallurgy

DOI ID:

<http://dx.doi.org/10.17159/2411-9717/1043/2020>

ORCID ID:

L.L Mthembu
<https://orcid.org/0000-0002-2751-0305>

Synopsis

Thorncliffe Chrome Mine, one of Glencore's Eastern Chrome operations, is currently mining the Middle Group No.1 (MG1) chromitite layer and is conducting a pre-feasibility study for an expansion project to mine the Middle Group chromitite No.2 (MG2) layer. This paper focuses on identifying viable areas within the MG2 layer that adhere to the mining, geological, and rock engineering parameters for a safe multiple-reef operation; and establishing efficient ways of accessing and extracting the MG2 chromitite layer. The findings from the multi-reef project at Samancor's Tweefontein Mine (Gouvea, 2013) and Maritz (2015) emphasized that the best layout for a safe and stable multi-reef operation is one where pillars are superimposed.

The guidelines by Salamon and Oravecz (1976) were key in the selection criteria for pillar stability.

A stage gate analysis was used to identify mineable areas using the success selection criteria for mineability obtained from geotechnical and geostatistical analysis of the assay data and isopach plan. During this study, it was found that the most cost-efficient way of accessing the MG2 chromitite layer is from the MG1 mining horizon through a connecting ramp instead of sinking a shaft. Moreover, using the MG1 infrastructure during the development of the MG2 mining horizon will reduce the project development cost. A bord-and-pillar layout with superimposed pillars will assist in reducing the stress concentrations and interactions between the two mining horizons.

With all the considerations being satisfied, it can be concluded that the MG2 layer is viable to mine in a safe manner along with the MG1 layer in a multi-reef environment.

Keywords

multi-reef mining, chromite, superimpose pillars, mineable areas, Bushveld Complex, Middle Group No. 2 layer.

Introduction

This report is based on vacation work done by the author at Thorncliffe Chrome Mine during December 2018 and January 2019 to identify areas at Thorncliffe Chrome Mine that would be amenable to alternative layer mining. Thorncliffe, located in the eastern limb of the Bushveld Complex (BC), South Africa is one of Glencore's Eastern Chrome mining operations; it is a four-barrel decline system sunk on reef and produces 100 000 t/month on average from the Middle Group Chromitite No. 1 layer (MG1) using mechanized bord-and-pillar mining.

The Thorncliffe concentrator produces five main products, namely (in descending order of chromite content): foundry, metallurgical grade, low metallurgical grade, chips, and lump. The concentrates with a high chromite content are smelted to produce ferrochrome at either the Lydenburg or the Lion smelter.

The Middle Group chromitite layers are found in the Critical Zone of the Rustenburg Layered Suite of the BC (Figure 1). The chromitite reefs are fine-grained with prominent nodules throughout; the immediate footwall and hangingwall consist of pyroxenite. It is important to note that the Middle Group No.2 chromitite layer (MG2) is situated above the MG 1 layer as seen in Figure 2. The MG1 layer has a thickness of 1.87 m and dips between 10 and 14 degrees.

Motivation for the study

The ferrochrome industry is currently facing serious challenges, due to the trade war between the USA and China, as well as production cost due to mine closures and lack of new ferrochrome capacity (Pastour, 2019). However, chrome ore production is expected to grow at a compound annual growth rate (CAGR) of 7% in the period 2019 to 2029 (Technavio, 2019).

Identification of suitable areas for multi-reef operation at Thorncliffe Chrome Mine

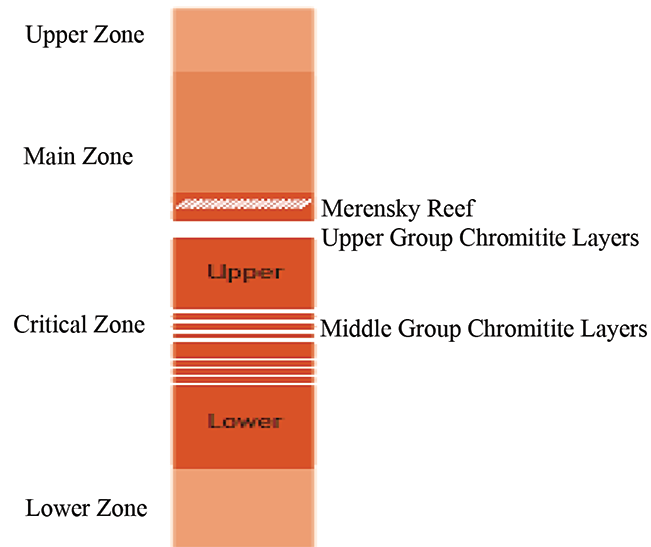


Figure 1—Stratigraphy of Rustenburg Layered Suite of the Bushveld Complex (Mthembu, 2019)

LAYER / UNIT - MG2 UNDIFFERENTIATED	Thickness	Lithology		Chromitite		MG2	Description
		Chr	PX	MG2C	MG2C/W		
70cm		CHR		MG2C		MG2	MG2 Chromitite Package (2A, 2B & 2C)
		PX		MG2C/W			
		CHR		MG2C			
10-20cm		PX				MG2	MG2 Chromitite Package (2A, 2B & 2C)
		CHR		MG2B			
		PX		MG2B/W			
13cm		CHR		MG2B		MG2	MG2 Chromitite Package (2A, 2B & 2C)
		PX		MG2B/W			
		CHR		MG2B			
1.53m		PX				MG2	MG2 Chromitite Package (2A, 2B & 2C)
25cm		CHR		MG2A		MG2	MG2 Chromitite Package (2A, 2B & 2C)
		PX		MG2A/W			
		CHR		MG2A			
15.25m		PX					Pyroxenite
11cm		PXCHRDISS		MG1L2	MG1L2		Disseminated Leader occur in PX
8.9m		PX		MG1HW2	MG1HW2		Pyroxenite
17cm		CHRDISS		MG1L1	MG1L1	MG1	Disseminated chromitite Leader band
45cm		PX		MG1HW1	MG1HW1		
1.3 - 1.7m(1.58m)		CHR		MG1			
		PX		MG1W			
		CHR		MG1			

Figure 2—Stratigraphic column showing the MG1 and the MG2 chromitite layers (Glencore, 2018)

According to Beveridge (2017), South African ore production is projected to need to increase to 2.5 Mt by 2021 in order to meet future market demands.

The projected increase in chrome ore demand affords Thorncliffe Chrome Mine the opportunity to increase output by exploiting the MG2 chromitite layer. This study was conducted to identify the viable areas within the MG2 that conform with the rock engineering, geological, and mining requirements.

The MG2 package varies from 1.85 m to 2.5 m in thickness

throughout the BC, and is subdivided into the MG2a, MG2b, and MG2c (see Figure 2). For the purpose of this study these will be treated a single layer, taking into consideration the inherent dilution that would be introduced by mining the intervening pyroxenite layers.

This paper outlines the process followed to ascertain the feasibility of mining the MG2, but does not include the financial implications of the expansion nor does it consider downstream smelting as the project is still in feasibility stage.

Identification of suitable areas for multi-reef operation at Thorncliffe Chrome Mine

Table I

Summary of the project approach

Objective	Methodology
Review various criteria for defining a mineable area	– Literature study
Investigate geological, rock engineering, and mining factors to be considered	– Collect geology geological rock engineering and mining reports – Interview the senior rock engineer, and geologist – Literature study
Evaluate the capacity of the current infrastructure	– Visit the Thorncliffe concentration plant
Establish efficient ways of accessing and extracting the MG2	– Literature study on similar projects and efficient ways of accessing alternative layers in a brownfield operation
Display the resultant mineable areas in a visual format	– Utilized MicroStation (AutoCAD) software and borehole data to map the mineable areas that adhere to the set mining parameters.

Method

The methodology used in this study is outlined in Table I.

Literature survey

Multi-reef mining in a hard-rock environment is an established practice as shown by the following case studies of similar projects.

Case study 1: Tweefontein Chrome Mine

Samancor's Tweefontein Mine is situated in close proximity to Thorncliffe Chrome Mine, and is thus benchmark for multi-reef mining due to the stratigraphy being similar to that at Eastern Chrome Mines. Tweefontein is currently mining the MG2 layer above the mined-out MG1 horizon. Multi-reef mining started in 2008.

Pillar stability and the influence of the MG2 horizon on the stability of the pyroxenite middling were assessed using numerical modelling to determine the best pillar layout, on the basis of induced tensile stress and excess shear stress, for a safe and stable operation (Gouvea, 2013).

The results conclusively indicated that the best layout was one with superimposed pillars. The stress due to the overburden on the MG2 mining horizon and the stress interactions between the MG2 and MG1 horizons were found to be insignificant and did not affect the overall stability of the operation. Due to the low average pillar stress, determined using the methodology proposed by Malan and Napier (2011), footwall punching was not expected

Case study 2: The effects of vertical stresses on pillar strength

The study (Maritz, 2015) focused on a mine situated in the eastern limb of the BC with a similar stratigraphy to Thorncliffe Chrome Mine. The mine's bord-and-pillar layout was simulated using Tabular Excavation Analysis (TEXAN) code. The author hypothesised a scenario for one section in which the pillars in the MG2 horizon and those in the MG1 mining horizon were superimposed (situated directly above each other), while in the other section the pillars not superimposed.

The effect of possible shear stresses on the pillar strength was evaluated.

The author argues that shear stress can be induced in pillars that are superimposed, while on the other hand, if pillars are not superimposed less stress is transferred to the MG2 pillars and the stresses on the MG1 pillars increase, as expected. However, the author emphasises that this scenario applied when the mining

spans in the MG2 horizon were small and the factor of safety of pillars was high. As mining progresses, pillar and beam failure might occur due to the difficulty in transferring stress because of the longer spans. Hence, it is vital that MG2 regional pillars are superimposed with MG1 regional pillars to assist with the transfer of stresses.

Maritz (2015) concluded, based on this specific study, that when identical pillars are perfectly superimposed in a multi-reef layout, shear stresses are induced. This is due to the slight reduction in the normal stress acting on pillars. However, he emphasised that the effects of shear stress on the stability of pillars was not quantified and requires further research.

Summary

The findings from these two case studies can be utilized by Thorncliffe Chrome Mine to understand the factors influencing the positioning of pillars. Moreover, they emphasise the importance of a superimposed pillar layout in a hard-rock multi-reef environment for a safe and stable operation.

Multi-reef mining

Zipf (1900) and Hill (2014) investigated the factors that control interactions in multi-seam mining including vertical stress concentration, stress re-direction, bedding plane slip bands, and horizontal stress concentrations. Other factors to be considered are mining geometry, mine design, mining sequence, and geology. Although these factors were established in a coal mining environment, they can be applicable in a hard-rock mining environment with the same mining layout. However, it is important to note how these factors will differ in a hard-rock environment.

The industry guidelines for superimposition (Salamon and Oravec 1976) were instrumental in the evaluation of mineable areas at Thorncliffe.

Results

Geostatistical and geotechnical analysis

The isopach chart illustrated in Figure 3, together with the assay data, was used to assess mineable areas. The isopach chart was compiled from borehole data and indicates the parting thickness between the MG1 and MG2.

During the evaluation of mineability, the MG2 was divided into 114 geological blocks.

The criteria used to assess the mineability of the blocks are detailed in Table II.

Identification of suitable areas for multi-reef operation at Thorncliffe Chrome Mine

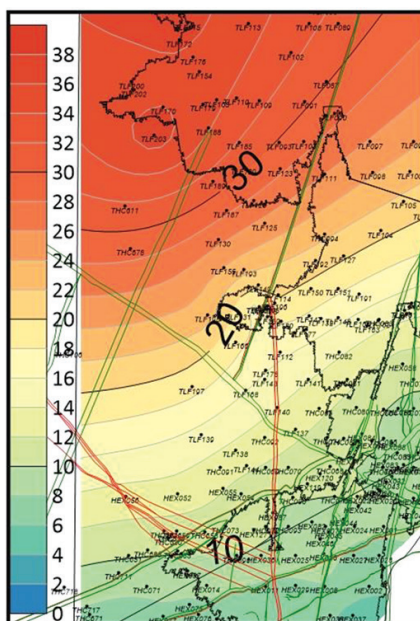


Figure 3—Isopach plan (Glencore, 2019)

Table II

Selection criteria for identifying mineable areas

Criterion	Description
Parting thickness	A minimum acceptable parting distance of 7 m between the MG1 and MG2.
Internal dilution	Maximum internal dilution of 15% (assumed)
Pillar strength	Superimposed pillars adhering to the Salamon and Oravec (1976) guidelines
Mining method	Bord -and -pillar mining (low extraction method)
Depth of cover	The thickness of overburden above the ore horizon. The orebody has to be within the desired relative location such that significant overburden stress concentrations are not included
Parting characteristics	This geotechnical characteristics of the parting between the MG2 and MG1
Regional geological features	Large faults, dykes, and potholes taken into accounted

Analysis of the selection criteria

Geostatistical and geotechnical analysis were conducted using the borehole data.

- The parting thickness between the MG1 and MG2 averaged 10 m over 95% of the production sections.
- The internal dilution due to the partings in the MG2 chromitite layer was less than the threshold of 15%, thus making 52% of the geological blocks economical for exploitation.
- 95% of working area had favourable parting characteristics.
- The case studies from the literature showed that bord-and-pillar mining will reduce the stress interactions in the MG2 mining horizons.
- The 54 geological blocks that can be mined economically allow for bord-and-pillar mining with a superimposed pillar layout, which does not influence the alternative mining horizons. There is a slight reduction in the normal stress concentration due to the generation of shear stress, which reduces the stress transfer between the pillars.

A stage gate process (Figure 4) was used to evaluate mineable blocks.

Mapping of the mineable area

MicroStation (3D CAD) was used to map the mineable area illustrated in Figure 5 that conforms to the selection criteria in Table II) within Thorncliffe Chrome Mine. The precise layout of the mineable area is withheld due to confidentiality reasons.

Summary

From the above evaluation criteria, it can be seen that approximately 47% of the potentially mineable MG2 reef is actually viable for extraction. This means that 53% of the geological block is not viable for extraction.

However, there are working areas that are borderline between viability and non-viability. Minimal changes can be made to make these areas viable for extraction. The characteristic that makes these areas nonviable is the parting thickness. By installing additional support and using relief mining, 16% of the borderline areas may be rendered viable. This would increase the area that can be exploited to 63% of the original block area, accounting for 72 of the original 114 blocks. Applying the mining method suggested and the appropriate method of access can increase the mine's reserves by 16.9 M reserves, and increase production by 50 kt/month.

Identification of suitable areas for multi-reef operation at Thorncliffe Chrome Mine

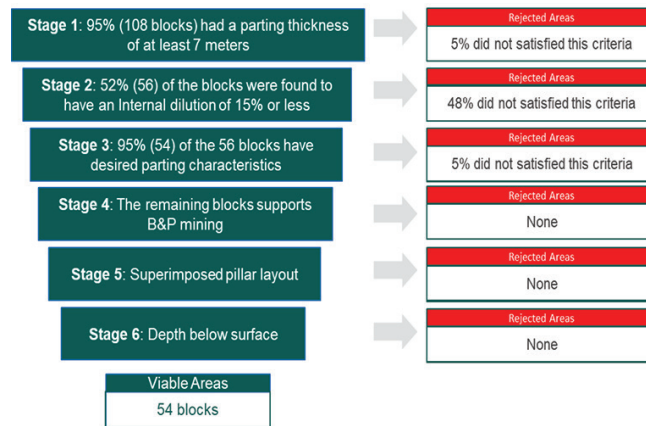


Figure 4—Stage gate process

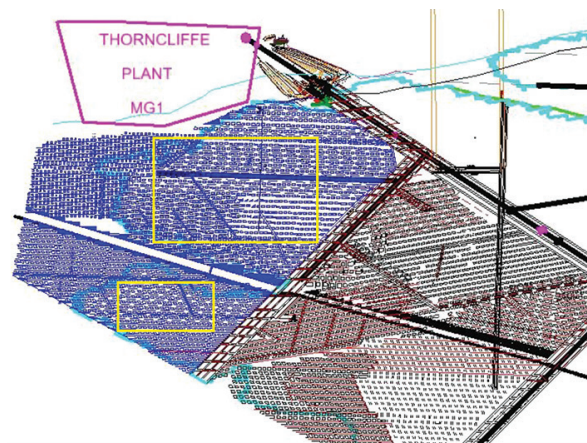


Figure 5—Area map showing the mineable area. Light blue – mine boundary, blue – the MG2 layer with approx. 47% of the geological blocks considered mineable, black/brown layout - MG1 layer, black lines – conveyor belts, yellow – mineable areas

Conclusion

A stage gate approach was used to evaluate criteria for the mineable areas. The criteria used the inherent geology required and the mining requirements for multi-reef operations as per operational standards. Fifty-four out of 114 geological blocks were found to be mineable.

The geological factors that were considered in the evaluation include depth of cover, rock characteristics, parting characteristics, and parting thickness. These were ranked from highest to lowest priority.

The production capacity of the current infrastructure was reviewed, and it was found that an additional production of 50 kt per month from the MG2 could be sustained.

Due to the fact that the infrastructure capacity supports mining from the main shaft, a secondary access will be used to access the reef as oppose to a new shaft being sunk from surface. This helps to improve the profitability, as the costs of sinking a new shaft clearly outweighs the revenue of mining the MG1.

With all the considerations being satisfied, it can be concluded that the MG2 layer is viable to mine in a safe manner together with the MG1 layer in a multiple reef environment.

Acknowledgements

I wish to extend my gratitude and appreciation to the following organizations and persons for their guidance and assistance during the course of the study.

Dr L.D. Meyer of the University of Pretoria (supervisor)
Mr W. du Preez of Glencore (Chief Geologist)

References

- BEVERIDGE, M. 2019. Ferrochrome Market Overview.2017. Merafe Resources. <https://www.meraferesources.co.za/pdf/presentations/2017/cru-market-overview.pdf> [accessed 10 October 2019].
- EDWARDS, A.C. 2001. Mineral Resource and Ore Reserve Estimation - The AusIMM Guide to Good Practice: (Monograph 23) - 36.2.2 Underground Mining. Australasian Institute of Mining and Metallurgy, Melbourne. 325 pp.
- GLENCORE. 2017. Mandatory Code of Practice. Thorncliffe Chrome Mine. DMR Number: 3057. Unpublished internal report.
- GLENCORE. 2018. Support Procedure. Thorncliffe Chrome Mine. DMR Number: 2595. Unpublished internal report.
- GOUVEA, J.P. 2013. Numerical modelling and analysis of the multi-reef mining layout at Tweenfontein Mine. Open House Management Solution (Pty) Ltd. Unpublished internal report.
- HILL, R.W. 1994. Multiseam design procedures. CSIR: Division of Mining Technology. Safety in Mines Research Advisory Committee, Johannesburg. pp. 4-5.
- MARITZ, J.A. 2015. The effect of shear stresses on pillar strength. *MEng thesis*, Department of Mining Engineering, University of Pretoria. pp. 40-50.
- MARTIN, C. and W. MAYBEE, W. 2000. The strength of hard-rock pillars. *International Journal of Rock Mechanics and Mining Sciences*, vol. 37, no. 8. pp. 1239-1246.
- PASTOUR, D. 2019. Chrome alloy global markets - challenges and prospects. <https://www.unichrome.ch/storage/20092019.pdf> [accessed 10 October 2019].
- TECHNAVIO. 2019. Global ferrochrome market analysis - size, growth, trends, and forecast 2019 -2023. https://www.technavio.com/report/global-ferrochrome-market-industry-analysis?utm_source=t10discount&utm_medium=bw_wk50&utm_campaign=businesswire [accessed 25 February 2019].
- AUSTRALASIAN INSTITUTE OF MINING AND METALLURGY. <https://app.knovel.com/hotlink/pdf/id:kt008VMPW2/mineral-resource-ore/underground-mining>
- ZIFF, R.K. 1900. Failure mechanics of multiple seam mining interactions. NIOSH-Pittsburgh Research Laboratory. pp. 93-94. ◆

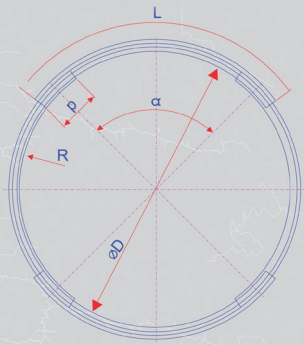


ELBROC
MINING PRODUCTS (PTY) LTD

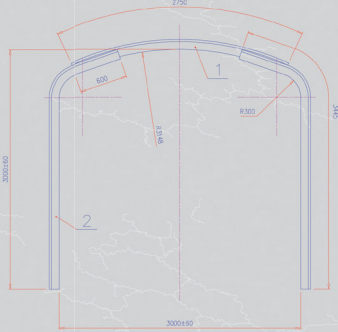
TH ARCH SUPPORT SYSTEMS

PROFILE SETS

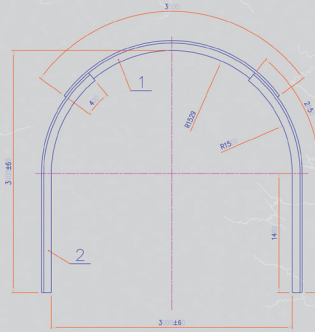
Ring Set



Semi Arch Set



Half Arch Set



PRODUCTION CAPABILITIES:

- Standard arch lengths from 1.8m to 5.5m
- Minimal curvature R 1000mm, at R 1200mm at R 1600mm

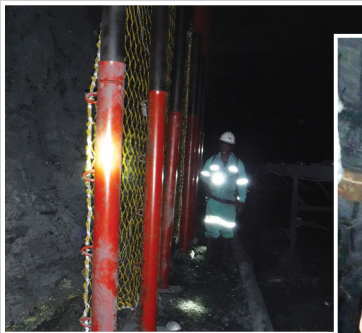
APPLICATIONS

- Tunnel junctions
- Over and under ore passes
- Haulage
- Incline shaft portals
- Active support through bad ground conditions, dykes, faults, friable ground

BENEFITS

- Simple and fast installation
- High load carrying capacity
- Long operational life
- Suitable for tunnels from 4.15m to 5.5m wide
- Upright support beams cater for tunnel heights from 3.1 to 6.5m
- Cost effective
- Dimensional and design flexibility

OMNI 150



APPLICATIONS

- Tunnel support
- Pillar rehabilitation
- Set construction on friable ground
- Active blast on support
- Used with backfill
- Travelling ways, mono ways and winch chambers

BENEFITS AND FEATURES

- Provides active roof support with controlled yielding
- Working load set to customer requirements (8 to 45 ton)
- Resilient in rockburst conditions
- Superb energy absorption
- Can accommodate numerous seismic events

- Constant and consistent support resistance
- Light, easy and quick to install
- Safe remote installation
- Cannot be over extended
- Reusable versions available on request
- Standard lengths available to 6 meters
- Longer lengths available on request

SABS
ISO 9001

a member of the

rbh
royal bafokeng holdings



**TO VIEW OUR FULL RANGE OF TUNNEL SUPPORT
PLEASE VISIT OUR WEBPAGE**

Tel: +27 010 534 5174 • sales@elbroc.co.za
www.elbroc.co.za





An investigation into the permeability of a PGM slag freeze lining to sulphur

H. Steenkamp^{1*} and A.M. Garbers-Craig¹

*Paper written on project work carried out in partial fulfilment of B.Eng (Metallurgy) degree

Affiliation:

¹Centre for Pyrometallurgy,
Department of Materials Science
and Metallurgical Engineering,
University of Pretoria.

Correspondence to:

A.M. Garbers-Craig

Email:

Andrie.Garbers-Craig@up.ac.za

Dates:

Received: 30 Nov. 2019

Revised: 22 Jun. 2020

Accepted: 23 Jun. 2020

Published: June 2020

How to cite:

Steenkamp, H. and
Garbers-Craig, A.M.
An investigation into the
permeability of a PGM slag freeze
lining to sulphur.
The Southern African Institute of
Mining and Metallurgy

DOI ID:

<http://dx.doi.org/10.17159/2411-9717/1044/2020>

Synopsis

Sulphur driven off from the sulphides in the black top of PGM smelters has in past years caused failure of copper coolers. When the magnesia-chromite bricks in the smelter were replaced with graphite blocks, however, copper cooler corrosion drastically decreased and furnace campaign lives improved. This study explores the role of the slag freeze lining in the permeation of sulphur to the copper cooler. This was done by measuring the gas permeabilities of two freeze linings and comparing them against the permeabilities of typical graphite and magnesia-chromite bricks that are used in PGM smelters; measuring the gas permeabilities of the different layers (hot face, crystalline layers, and cold face) of a freeze lining; and testing the permeation of liquid sulphur through freeze lining samples at 120 and 180°C. It was found that the freeze lining samples had gas permeabilities of 1.5 and 0.8 cd at a differential pressure of 32 kPa, compared to the permeabilities of the magnesia-chromite (10.0 cd) and graphite bricks (4.85 cd). The cold face layer of the freeze lining had the lowest permeability (1.8 cd), and the hot face layer the highest (2.4 cd). At 120°C liquid sulphur permeated the freeze lining through cracks. The freeze lining can therefore participate in preventing sulphur permeation towards the copper coolers, as long as its cold face remains intact and crack free. An added benefit of using graphite blocks in the smelter is that it establishes a glassy cold face layer in the freeze lining, which has a very low gas permeability.

Keywords

slag freeze lining, permeability, sulphidation of copper coolers, porosity.

Introduction

Copper coolers used in the primary smelting furnaces of the platinum group metal (PGM) industry fail due to chloride-accelerated sulphidation (Shaw *et al.*, 2013). This is caused by sulphur being driven off from sulphides in the green concentrate which, together with chlorine-bearing species in the presence of moisture, diffuses towards the copper cooler and reacts with it. The corrosion rate and morphology of the corrosion products that form on the copper coolers are functions of temperature and corrosive gas composition (H_2S , S_2 , and a combination of S_2 and HCl) (Thethwayo and Garbers-Craig, 2011, 2010). HCl was found to significantly increase the rate of sulphidation of the copper coolers at temperatures as low as 90°C.

The PGM slag freeze lining has a porous appearance which creates the expectation that it does not play a role in the prevention of sulphur migration to the copper coolers. Against this background, the purpose of this study was to determine what role the slag freeze lining plays in the migration of sulphur from the molten bath to the copper coolers. The research had three objectives: to determine the gas permeability of the freeze lining and to compare it to the permeabilities of refractory bricks used in the PGM industry; to determine which layer of the freeze lining (hot face, crystalline layers, or cold face) has the lowest gas permeability; and to determine the permeability of a PGM freeze lining to liquid sulphur.

The slag freeze lining samples that were investigated were taken from two primary PGM smelters owned by Anglo American Platinum in South Africa.

Background

PGM smelting and the use of copper coolers

Anglo American Platinum treats sulphide ores from three reefs within the Bushveld Complex, namely the Merensky, UG2, and Platreef (Jacobs, 2006). The ore is crushed and the base metal sulphides with which the PGMs are associated are upgraded through sulphide flotation. The concentrate is then smelted

An investigation into the permeability of a PGM slag freeze lining to sulphur

to allow for separation of the gangue and sulphides into slag and matte respectively, based on their different densities. In South Africa Anglo American Platinum has its smelting operations at the Waterval, Mortimer, and Polokwane plants (Hundermark *et al.*, 2011). After smelting, the furnace matte is further processed in a converter to remove iron and sulphur, after which the respective base metals and PGMs are separated into saleable products.

Copper coolers were first implemented in the furnace linings of PGM smelters in 1990. This allowed for a high enough heat flux to be generated across the furnace wall whereby a layer of molten slag could freeze onto the hot face of the refractory bricks in contact with the copper cooler, creating a freeze lining. The freeze lining protects the underlying refractory lining from chemical attack by slag, erosion, and thermal stress (Duncanson and Toth, 2004). Before freeze linings were used, furnace walls had to be rebuilt every two to three years, whereas the expected lives of the copper coolers are measured in decades (Shaw *et al.*, 2013).

Corrosion of the furnace lining became a major issue in the Anglo American Polokwane Smelter when the shift from the plate copper cooler design to the waffle copper cooler design was implemented (Shaw *et al.*, 2013). The greater efficiency of the waffle copper cooler facilitated a significant increase in furnace power input (from 34–42 MW to 68 MW). However, a new wear mechanism, the corrosion of the hot face of the copper coolers in the upper slag zone, led to a shortened campaign life of the waffle coolers (Figure 1). Since the cooling medium in the copper coolers is water, damage to the water channels led to a water leak and a subsequent steam explosion. Explosions can cause failure of the furnace wall, run-out of molten material, major infrastructural damage, and significant downtime of the furnace. Fatalities and injuries to personnel working in close vicinity of the furnace can also result.

According to Shaw *et al.* (2013) there was an abundance of elemental sulphur at the corroded hot face of the copper cooler removed from the Polokwane Smelter in 2004. The presence of sulphur was not a surprise as the base metal sulphide concentrate charged into the furnace was not roasted to remove sulphur before smelting, as in other sulphide smelting industries. Thermal decomposition of sulphides in the concentrate ('black top') and matte therefore occurs in the smelter, whereby sulphur is produced according to Equations [1] to [5] (Thethwayo, 2010; Mabiza *et al.*, 2011):



The corrosion products that formed at the hot face of the Polokwane copper cooler in 2004 were identified using EDS analysis. The various product layers are illustrated in Figure 2.

Shaw *et al.* (2013) reported that water-cooled copper can react with sulphur gas at temperatures as low as 25°C, while the presence of HCl gas greatly accelerates corrosion of the copper coolers. The corrosion mechanism was described as 'chloride-accelerated sulphidation', as it involves the corrosion of copper in the presence of sulphur- and chlorine-bearing species in the presence of moisture (Shaw *et al.*, 2013).

Measures that have been taken to monitor chloride-accelerated sulphidation include ultrasonic measurement of the thickness of the corrosion layer on the copper coolers and detection of water leaks which may be a result of copper cooler corrosion (Shaw *et al.*, 2013). Downtime during copper cooler replacement was shortened by separating the copper cooler into an upper and lower cooler, whereby the upper cooler could be replaced separately, requiring only partial drainage of the furnace. Corrosion layers do not protect the copper as the corrosion products have Pilling-Bedworth ratios of more than two (Shaw *et al.*, 2013). The corrosion products therefore flake off, exposing fresh copper and corrosion continues. Post-mortem analyses of magnesia-chromite and graphite bricks removed from PGM smelters confirmed that the refractory bricks together with the rammable (which ensures thermal contact between the refractory brick and the copper cooler) do not keep the sulphide corrosion product secured to the copper (Thethwayo and Garbers-Craig, 2010). Visual inspection of the magnesia-chromite lined smelter wall also indicated that the brick at the concentrate-slag interface was completely corroded away, leaving the freeze lining in direct



Figure 1—Corrosion of the copper cooler, characterized by the presence of copper sulphide in the upper slag zone close to the slag-concentrate interface (after Shaw *et al.*, 2013)

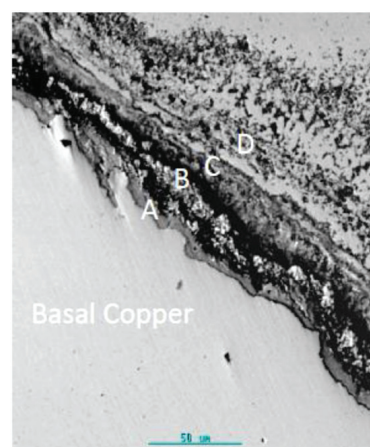


Figure 2—Backscatter electron image of the corrosion layers (A, B, C and D) at the interface of the 2004 Polokwane copper cooler. Layers C and D consisted mainly of copper sulphides. Layer B consisted of oxygen-bearing copper sulphides, chlorides, and sulphates. In direct contact with the basal copper (layer A) was a thin layer of copper chloride (after Shaw *et al.*, 2013)

An investigation into the permeability of a PGM slag freeze lining to sulphur

contact with the copper cooler. Magnesia-chromite bricks that were used in contact with the copper coolers were subsequently replaced with graphite blocks. The use of graphite-protected copper coolers in the concentrate-slag zone has significantly slowed the rate of copper cooler corrosion and drastically improved furnace campaign life (Shaw *et al.*, 2013).

The sulphur partial pressure in the smelter is a function of the sulphur content of the matte and the temperature (du Preez, 2009). If the PGM matte with a sulphur content of 22–30 wt% (Nolet, 2014) is assumed to behave like nickel matte, the sulphur partial pressure at the slag-concentrate interface in front of the hot face of the freeze lining will range between 10^{-5} and 10^{-4} atm. at 1400°C (Figure 3, du Preez, 2009). From the $\log P_{S_2}$ -temperature diagram published by Lyons (2008), it is clear that sulphur partial pressure above 10^{-5} atm. can be achieved when heating sulphur (S8) at temperatures above 100°C (Figure 3).

Microstructures of freeze linings

There are many factors that control the microstructural characteristics of a freeze lining. According to Crivits (2016) the efficiency of a freeze lining is best when the initial solidification is dominated by the rapid growth of interlocking crystals and the formation of a subsequent high-melting crystalline sealing layer.

Three major layers are discerned: the cold face adjacent to the refractory brick, the hot face in contact with the slag bath, and a series of crystalline layers in-between the cold and hot faces. The layers in a PbO-ZnO-FeO-Fe₂O₃-CaO-SiO₂-based freeze lining produced in laboratory experiments were identified and classified by Crivits (2016) in terms of their microstructures and compositions (Figure 4). The first two layers that formed on a cold finger probe were glassy in nature and are referred to as the 'cold face'.

The cold face consists of an amorphous phase with a homogeneous composition identical to that of the slag bath, followed by a glassy layer, which contains very fine crystals. The next few layers form part of the group of crystalline layers of the freeze lining. The first crystalline layer is the 'closed

crystalline layer', which consists of crystals that solidified directly from the melt and that effectively prevented the exchange of molten material between the bath and the freeze lining. The 'open crystalline layer' consists of large crystalline grains with a significant liquid fraction that is open for exchange of material with the slag bath. The last major layer is the 'hot face', which is a sub-liquidus layer that forms the interface between the freeze lining and the molten bath. It has a higher porosity than the dense cold face and an irregular surface. This sealing layer consists of primary crystals that continuously precipitate and dissolve directly from the bath. Crivits (2016) found that a thin layer of slag from the bulk slag bath formed the outer layer of the freeze lining (layer 6, Figure 4). The major layers, namely the cold face, crystalline layers, and hot face, are expected to have different gas permeabilities due to their different microstructures.

Theory of permeability

In this study, the permeability of a PGM slag freeze lining and other refractory materials were investigated as a measure of the ease with which sulphur can migrate towards the copper coolers. Permeability refers to the capacity of a porous material for transmitting a fluid (liquid or gas); it is expressed as the velocity with which a fluid of specified viscosity, under the influence of a given pressure, passes through a sample having a certain cross-section and thickness (Augustyn, *et al.*, 2018). Apparent porosity is the volume of open pores as a percentage of the bulk volume of a material and can be used to compare the expected corrosion resistance of different materials (Berger, 2010). A direct relationship between permeability and apparent porosity does not exist, as only connected open pores affect permeability and facilitate permeation of fluids through a material.

The ASTM Permeability Test Method C577-07 is used to measure the permeability of refractory bricks. The permeability is calculated according to Darcy's Law (Equation [6]):

$$K = \frac{MQL}{A\Delta P} \times 100 \quad [6]$$

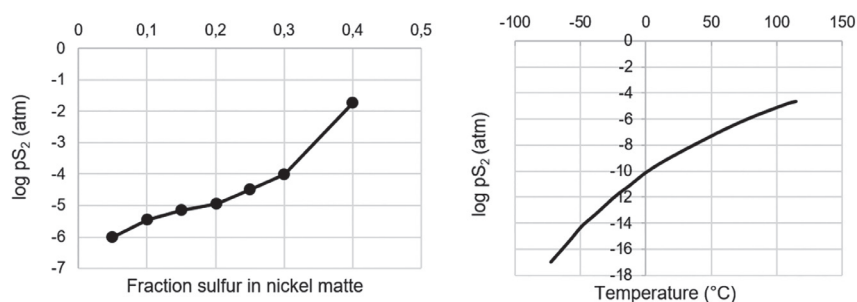


Figure 3—(Left) The partial pressure of sulphur as a function of the sulphur content of a nickel-based matte (after du Preez, 2009); (right) the partial pressure of sulphur (S₂) as a function of temperature (after Lyons, 2008)

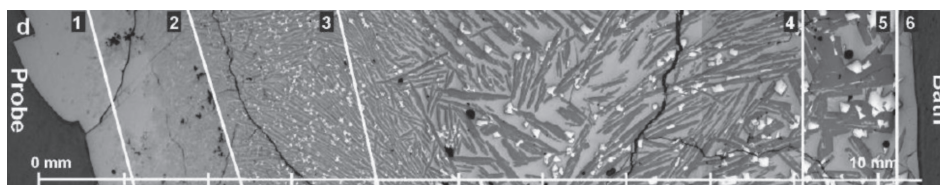


Figure 4—Cross-section of a freeze lining that formed from a PbO-ZnO-FeO-Fe₂O₃-CaO-SiO₂ slag on a cold finger probe, submergence time 120 min. (1) Glassy layer, (2) glass with fine crystals, (3) closed crystalline layer, (4) open crystalline layer, (5) layer of sealing crystals, (6) layer of entrained slag from slag bath (after Crivits, 2016)

An investigation into the permeability of a PGM slag freeze lining to sulphur

where

K : permeability, centidarcys

M : gas or liquid viscosity, cP (temperature- dependent)

Q : flow rate, cm³/s

L : sample length, cm

A : sample area, cm²

ΔP : absolute pressure drop across the sample, atm.

The permeability is expressed in darcys, where 1 darcy is equal to 10⁻¹² m². One centidarcy is a flow of 0.01 cm³/s of a fluid of 1 cP viscosity through a 1 cm cube under a pressure difference of 1 atm. The ASTM standard stipulates that the permeability be reported at a pressure differential of 32 kPa. Permeabilities at lower and higher pressure differentials were also measured in this study.

The permeability of a material constituted from a number of layers can be calculated from the permeabilities and thicknesses of the layers according to Equation [7] (Kantzas, Bryan, and Taheri, 2015). This calculated overall permeability of the material is called the harmonic-average permeability. For steady state, the flow rate through each layer is the same and the pressure drop across the entire system is therefore the sum of the pressure drops across each layer (Equation [8]).

$$K_{av} = \frac{L}{\left(\frac{L}{K}\right)_1 + \left(\frac{L}{K}\right)_2 + \left(\frac{L}{K}\right)_3} \quad [7]$$

$$\Delta P_t = \Delta P_1 + \Delta P_2 + \Delta P_3 \quad [8]$$

where

K_{av} = harmonic-average permeability

L = total thickness of the multi-layered material

$(L/K)_i$ = thickness to permeability ratio of layer i

ΔP_t = pressure drop across the multi-layered material

ΔP_i = pressure drop across layer i

In this study the harmonic-average permeability of the Mortimer freeze lining was calculated from the individually measured permeabilities and thicknesses of the cold face, crystalline, and hot face layers of the freeze lining.

Experimental

Sampling

Freeze lining samples were taken in 2018 and 2019 from the Anglo American Platinum Polokwane and Mortimer smelters respectively (Figure 5). These samples were taken from the sidewall at the slag-concentrate interface level, as this was the location of wear of the copper coolers (Figure 1). The morphology of the freeze lining is dependent on the conditions inside the furnace and may vary considerably over time. The Polokwane freeze lining sample was thinner than the Mortimer freeze lining sample (8 cm vs. 10 cm from the cold face to the hot face) and seemed less porous to the naked eye.

Magnesia-chromite and graphite bricks, typically used in the PGM smelters, were obtained from Anglo American Technical Solutions (at Crown Mines) in order to compare the permeabilities of the bricks with the freeze lining in the PGM smelter lining (Figure 6).

Bulk density and apparent porosity measurements

The bulk densities and apparent porosities of the freeze lining and brick samples were determined at Cermalab Materials Testing

Laboratory. The measurements were carried out according to the ISO 5016, ASTM C134, and ASTM D1895 test methods (Berger, 2010).

Sulphur penetration into the freeze lining

The Polokwane freeze lining sample was sectioned from the cold face to the hot face, whereby a 8 cm long and 3.5 cm wide sub-sample was taken for the sulphur penetration experiments. This 8 cm long sample was further sectioned in half through the crystalline layer, resulting in a top section (containing the hot face and part of the crystalline layer) and a bottom section (containing the rest of the crystalline layer and the cold face). In the first experiment a piece of sulphur was placed on top of the hot face of the top section, and on top of the crystalline face of the bottom section. Each freeze lining sample with the piece of sulphur was placed inside a graphite crucible, which in turn was placed inside a steel capsule. The capsule was then purged with argon, sealed (by welding a steel end cap onto the capsule and welding the perimeter of the purge screw) and placed in an autoclave. These assemblages were heated to 120°C and 180°C respectively and kept at the elevated temperature for 6 hours. These two temperatures were chosen so as to ensure that the sulphur was molten at the reaction temperature (melting point of sulphur is 115°C; Bello, 1988) and that the sulphur partial pressure was maintained above 10⁻⁵ atm. (Figure 3, Lyons, 2008). The temperature was monitored with a K-type thermocouple wrapped around the steel capsule. The sulphur melted and accumulated at the bottom of the crucible without penetrating the freeze lining.

For the next set of experiments 5 mm holes were drilled into the freeze lining specimens: through the hot face and partly into the crystalline layers, for the top section, and through the rest of

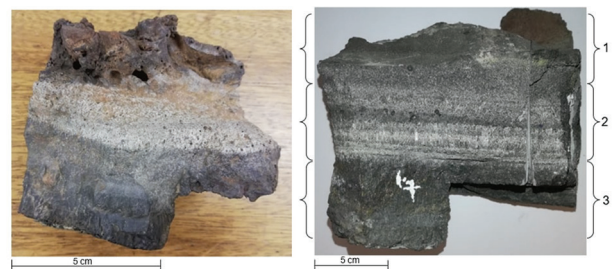


Figure 5—Photographs of the freeze lining samples retrieved from Polokwane Smelter in 2018 (left) and Mortimer Smelter in 2019 (right), with 1, 2, and 3 annotating the hot face, crystalline layer group, and cold face

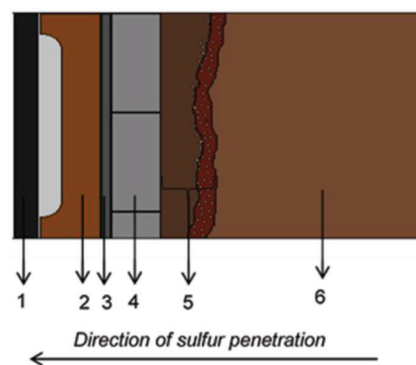


Figure 6—Schematic diagram of a section through the sidewall of a PGM smelter: (1) steel shell, (2) copper cooler, (3) ramming paste, (4) refractory brick layer, (5) freeze lining, and (6) molten slag bath

An investigation into the permeability of a PGM slag freeze lining to sulphur

the crystalline layer and partly into the cold face of the bottom section of the freeze lining specimen. The holes were filled with pulverized sulphur to determine whether sulphur would permeate into the freeze lining if the low wettability of sulphur on the freeze lining was overcome (Figure 7). The depth of penetration of sulphur into the freeze lining at the two temperatures was evaluated by examining a cross-section through the sulphur-filled specimen using SEM-EDS.

Permeability measurements

A permeability apparatus was constructed by adapting the ASTM C577-07 permeability test method to facilitate testing the freeze lining specimens as well as the refractory brick specimens (Figure 8).

The pressure drop across a specimen was measured with a Panasonic ADP 5140 gauge pressure sensor. The pressure sensor was connected to an Arduino UNO microcontroller board. The Arduino allowed the amplification of the output signal from the pressure sensor, which ranged from zero to five volts, to kPa. The amplification parameters were determined by calibration: a pressure was applied to both the pressure sensor and a U-tube manometer filled with mercury; the pressure was increased in increments and the level of the mercury in the manometer and the output voltage from the sensor recorded. The amplification parameters derived from the original pressure sensor output are stipulated in Equation [9]. Figure 9 shows the linear correlation between the output voltage and the pressure derived from the mercury manometer after calibration.

$$V = 0.0375P + 0.6033 \quad [9]$$

V : pressure sensor output in volts

P : pressure derived from mercury level in manometer

The ASTM standard recommends the use of a rubber gasket with a square aperture to seal off the edges of the sample during

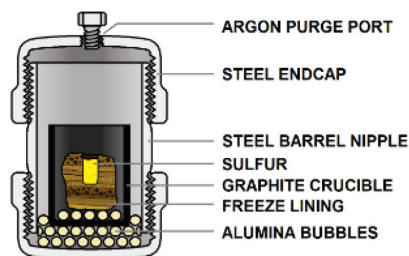


Figure 7—Test capsule with freeze lining filled with pulverized sulphur

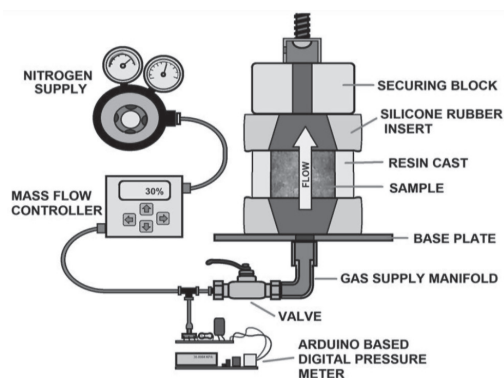


Figure 8—The permeability apparatus that was constructed according to the ASTM C577-07 standard

the permeability measurement. Although a square shaped aperture worked well when measuring the permeability of a refractory brick that can easily be sectioned into a cube, this was not the case with the freeze lining. The freeze lining had irregular faces and was brittle. This made it difficult to cut a sample into a regular shape such as a cube. To accommodate the uneven faces of the freeze lining, the method was adapted from the ASTM standard and samples were set in resin (to allow for sealing of the irregular edges of the freeze lining) and two silicone gaskets were made to seal onto the top and bottom surfaces of the resin (Figure 10).

Cubic specimens measuring $5.08 \times 5.08 \text{ cm}^2$ (2 in^2) of the magnesia chromite and graphite refractory bricks were prepared by setting in acrylic resin. The original surfaces (hot and cold faces) of the freeze lining samples were preserved during sample preparation, thus the length of the freeze lining samples was not 5.08 cm (as directed by the ASTM standard), but the as-received thickness of 10 and 8 cm for the Mortimer and Polokwane specimens. While the permeability was measured through all the composite layers of the Polokwane freeze lining, the Mortimer freeze lining sample was sectioned into its respective layers (Figure 5) whereby the respective contributions of each layer towards the overall permeability could be measured. The hot face, crystalline layers, and cold face had thicknesses of approximately 3, 5, and 2 cm respectively. The outer surface of the acrylic resin of each layer was sealed with a layer of silicone gasket sealant so that their individual permeabilities could be measured and the harmonic-average permeability of the layers in series could be calculated using Equation [7].

A 0.5 slm (standard litres per minute) mass flow controller was used to control the flow rate of nitrogen into the cavity bordering the lower surface of the sample. As these instruments are prone to error, the set flow rate was correlated to the actual flow rate by measuring the gas flow into a graduated cylinder submerged in a water bath.

For the gas permeability measurements, the samples (after being set in resin) were left in a drying oven at 110°C overnight

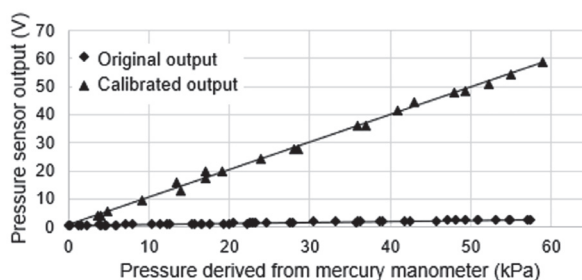


Figure 9—The amplification of the voltage output of the pressure sensor



Figure 10—(a) A sample of magnesia-chromite brick set in acrylic resin; (b) the profile of the custom silicone gasket

An investigation into the permeability of a PGM slag freeze lining to sulphur

to drive off any moisture. The sample for which the permeability was to be measured was secured between the two silicone gaskets and tightened at a set torque. The flow of nitrogen was increased in increments of 5% of the maximum flow rate, 0.5 slm. An average time of four minutes was allowed for the pressure to stabilize, after which it was assumed that the gas flow rate into the sample was equal to the flow rate out of the sample. The permeability was calculated using Darcy's Law (Equation [6]). The sets of measurements were repeated three times on each sample.

Results and discussion

Bulk densities and apparent porosities

The apparent porosities and bulk densities of the samples are summarized in Table I. The bulk densities of the Polokwane and Mortimer cold face layers were similar, and higher than the bulk density of the Mortimer hot face layer. This Mortimer hot face layer had the highest apparent porosity, and the cold face of the Polokwane freeze lining sample the lowest, confirming the macroscopic observations. The magnesia-chromite brick had a lower apparent porosity and higher bulk density than the graphite brick.

Penetration of liquid sulphur into the freeze lining

SEM-EDS analysis confirmed that liquid sulphur can penetrate into cracks inside the freeze lining at 120°C (Figure 11). During operation, cracks inside the freeze lining are expected to form due to thermal shock when level changes occur in the molten bath such as during tapping and downtime of the furnace. The cracks inside the specimens used in the experiments could have been introduced when the 5 mm hole was drilled. However, the freeze lining inside the smelter most certainly forms cracks as the freeze lining breaks off and re-forms. Thus, the experiment simulated the permeation of sulphur into a crack that formed in a freeze lining. The cracks seem to have propagated along the pores inside the freeze lining.

Although the degree of penetration by sulphur was expected to increase with an increase in temperature, the opposite was

observed. Compared to the penetration of sulphur into the freeze lining at 120°C (Figure 11), which was a few centimeters deep, there was virtually no penetration of sulphur into cracks of similar width at 180°C (Figure 12).

The lack of penetration of sulphur can be explained by the change in dynamic viscosity of liquid sulphur between 120 and 180°C. The four orders-of-magnitude increase in the dynamic viscosity of sulphur from 9×10^{-2} Pa.s to $93\,000 \times 10^{-2}$ Pa.s between 120°C and 187°C is shown in Figure 13 (Sofekun *et al.*, 2017). The maximum dynamic viscosity of sulphur at 187°C is 52 000 times the viscosity of water at 17°C, and sulphur was too viscous at 180°C to penetrate into cracks inside the freeze lining. Any liquid sulphur inside the furnace wall is expected to have a similar dynamic viscosity as the liquid sulphur in the first experiment at 120°C, due to the viscosity returning to 9×10^{-2} Pa.s at temperatures above 280°C (Figure 13). Thus, if cracks develop in a freeze lining during operation, they will become filled with sulphur. If these cracks have appropriate orientation

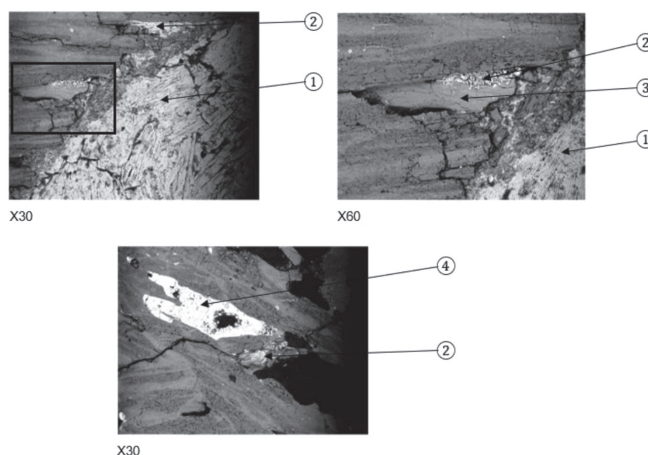


Figure 12—No penetration of sulphur into a cracked freeze lining at 180°C. (1) Primary sulphur inside drilled hole, (2) sulphur that penetrated into freeze lining, (3) iron, (4) entrained matte droplet

Table I

Bulk density and apparent porosity data of the brick and freeze lining samples

Sample	Bulk density (cm ³)		Apparent porosity (%)	
	Average	Standard deviation	Average	Standard deviation
Polokwane Smelter freeze lining: cold face	2.95	N/A	8.0	N/A
Mortimer Smelter freeze lining: cold face	2.92	0.12	10.8	1.8
Mortimer Smelter freeze lining: hot face	2.42	0.04	23.2	1.0
Magnesia - chromite brick	3.37	0.03	9.7	1.0
Graphite brick	1.90	0.03	20.0	0.3

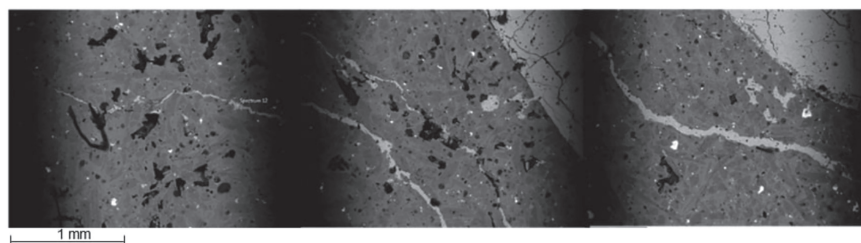


Figure 11—Penetration of sulphur into a cracked freeze lining at 120°C. The origin of the crack is below the drilled hole (right) and extended to the outer edge of the sample (left)

An investigation into the permeability of a PGM slag freeze lining to sulphur

(perpendicular to the hot face) and length, they can facilitate the permeation of sulphur through the layered freeze lining to the graphite block in front of the copper cooler. Sulphidation of the underlying copper coolers will then depend on the resistance of the graphite block to permeation by sulphur.

Gas permeability of a PGM furnace lining

The magnesia-chromite and graphite bricks have gas permeabilities of 10.0 and 4.85 cd respectively at a differential pressure of 32 kPa (Figures 14 and 15). The permeability of this graphite brick falls within the range of permeabilities (0.3–42 cd) reported by Eusner and Shapland (1959) for carbon-based materials that are used in blast furnaces. The standard deviations of the permeability measurements of the magnesia-chromite and graphite bricks across the three sets of measurements were 0.15 and 0.03 cd respectively. This provides confidence that the measurements obtained using the constructed apparatus were reproducible.

The permeabilities of the layers of the Mortimer freeze lining specimen as a function of pressure are shown in Figure 16. The hot face, crystalline layers and cold face had permeabilities of 2.4, 2.2, and 1.8 cd at a differential pressure (ΔP_i) of 32 kPa. The overall permeability of the composite freeze lining could be calculated as the harmonic-average permeability (described previously), which equalled 1.5 cd at a total differential pressure (ΔP_t) of 32 kPa (Figure 16).

The Polokwane and Mortimer freeze lining specimens had permeabilities of 0.8 and 1.5 cd respectively at 32 kPa. The freeze lining specimens therefore had significantly lower permeabilities than the refractory bricks that were tested (Figure 17), with the cold face controlling the overall permeability of the freeze lining (Figure 16). The Polokwane freeze lining specimen had almost

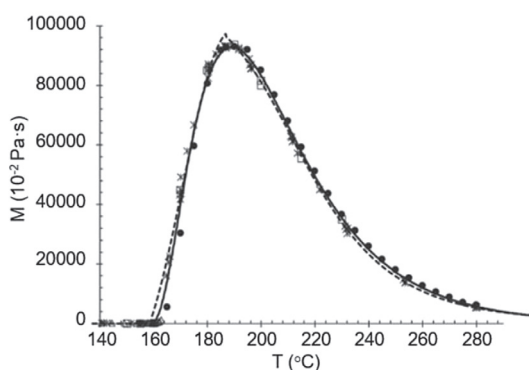


Figure 13—Dynamic viscosity of liquid sulphur as a function of temperature (Sofekun *et al.*, 2017)

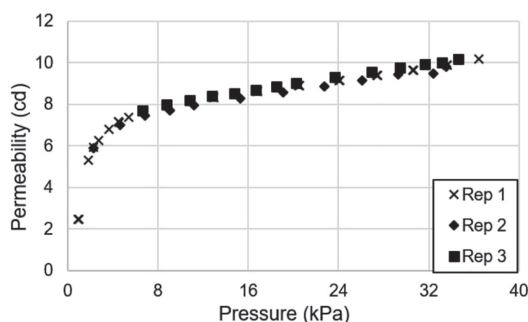


Figure 14—Permeability measurements on the magnesia-chromite brick

half the permeability of the Mortimer freeze lining specimen. The higher permeability of the Mortimer freeze lining (2019) is likely due to a combination of a thinner cold face (2 cm *vs.* 3 cm) and the higher apparent porosity which makes it prone to crack formation. The permeability of the graphite brick was lower than that of the magnesia-chromite brick (4.85 *vs.* 10.0 cd). This lower permeability is presumably one of the factors that contributed to an increase in the copper cooler campaign lives when graphite bricks replaced magnesia-chromite bricks in the PGM smelter. However, it is also assumed that the significantly higher thermal conductivity of the graphite brick, compared to the magnesia-chromite brick, altered the morphology of the freeze lining, *inter alia* by the formation of a thicker glassy cold face.

An uncracked PGM slag freeze lining will therefore impede sulphur and other corrosive fluids from permeating through the freeze lining to the refractory lining. The perception that the freeze lining is highly permeable due to its high apparent porosity

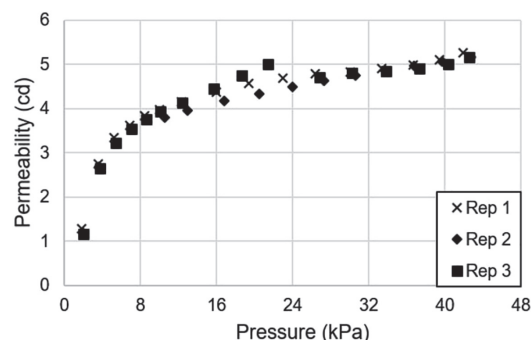


Figure 15—Permeability measurements on the graphite brick

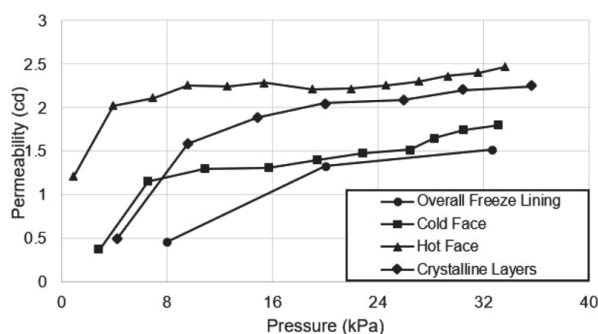


Figure 16—The permeabilities of the layers (K_i) that constituted the Mortimer freeze lining as a function of differential pressure (ΔP_i), as well as the permeability of the overall freeze lining (K_{avg}) as a function of total differential pressure (ΔP_t)

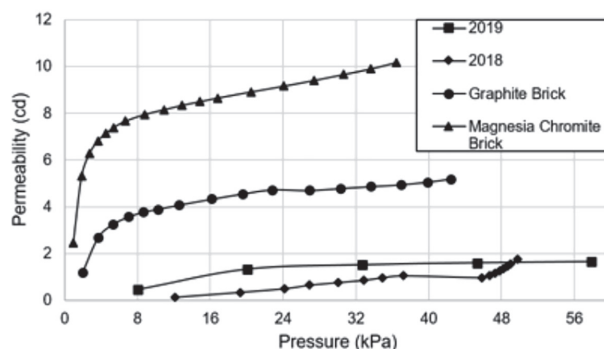


Figure 17—Permeabilities of the refractory bricks, Polokwane (2018) and Mortimer (2019) freeze lining samples

An investigation into the permeability of a PGM slag freeze lining to sulphur

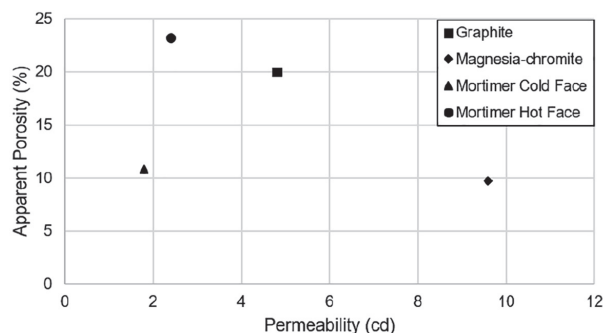


Figure 18—Comparison of the permeabilities of the samples tested and their apparent porosities

at the hot face was shown to be untrue since the hot face had the highest porosity (23.2%) but one of the lowest permeabilities (2.4 cd) compared to the refractory bricks (Figure 18). It is also important to acknowledge that the graphite brick, which has a significantly higher apparent porosity than the evaluated magnesia-chromite brick, has a significantly lower permeability than the magnesia-chromite brick that was previously used in front of the copper coolers.

Conclusions

- The permeabilities of the freeze lining specimens from Polokwane (0.8 cd) and Mortimer smelters (1.5 cd) were lower than those of the graphite (4.85 cd) and magnesia-chromite brick (10 cd) samples.
- The cold face, crystalline layers, and hot face layers of the sample of Mortimer freeze lining had permeabilities of 1.8, 2.2, and 2.4 cd respectively. The permeability of the cold face layer controls the overall permeability of the freeze lining.
- Liquid sulphur at 120°C is able to permeate through cracks in the slag freeze lining.
- An ideal slag freeze lining would be one that has a thick and crack-free cold face layer, as permeation of sulphur through the freeze lining to the refractory brick would then be minimized.

Acknowledgements

Anglo American Platinum is thanked for providing the University of Pretoria with the samples used in this project and for permission to publish the findings. The assistance of Dr Robert Cromarty (in the construction and calibration of the permeability test set-up) and Mr Dirk Odendaal (assistance in the laboratory) is also greatly appreciated. Cermalab is acknowledged for providing the University of Pretoria with the ASTM standard for testing the permeability of refractory bricks and for determining the bulk density and apparent porosities of the samples.

References

AUGUSTYN, A., BAUER, P., DUIGNAN, B., ALISON, E., GREGERSEN, E., MCKENNA, A., PETRUZZELLO, M., RAFFERTY, J.P., RAY, M., ROGERS, K., TIKKANEN, A., WALLENFELDT, J., ZEIDAN, A., and ZELAZKO, A. (eds.). 2018. Permeability. <https://www.britannica.com/science/permeability-physics> [accessed 8 May 2020].

BELLO, C. (ed.). 1988. Chemical Periodic Table. 2nd edn. Perma-Chart Science Series, Papertech Marketing Group Inc. Canada.

Berger, B.M. 2010. The importance and testing of density / porosity / permeability / pore size for refractories. *Proceedings of Refractories 2010 Conference*, Misty

Hills, Muldersdrift, South Africa, 16–17 March 2010. Southern African Institute of Mining and Metallurgy, Johannesburg. pp. 101–116.

CRIVITS, T. 2016. Fundamental studies on the chemical aspects of freeze linings. PhD thesis, University of Queensland, Australia.

DU PREEZ, R.C. 2009. Effect of lime additions on the chromium department in smelter matte-slag systems. MScEng thesis, University of Stellenbosch, South Africa.

DUNCANSON, P.L. and TOTH, J.D. 2004. The truths and myths of freeze lining technology for submerged arc furnaces. *Proceedings of the Tenth International Ferroalloys Congress, INFACON X*, Cape Town, South Africa, 1–4 February 2004. Southern African Institute of Mining and Metallurgy, Johannesburg. pp. 488–499. doi: 0-9584663-5-1

EUSNER, G.R. and SHAPLAND, J.T. 1959. Permeability of blast-furnace refractories. *Journal of the American Ceramic Society*, vol. 42, no. 10. pp. 459–464.

HUNDERMARK, R.J., MNCWANGO, S.B., DE VILLIERS, L.P.V.S., and NELSON, L.R. 2011. The smelting operations of Anglo American's platinum business: an update. *Proceedings of the Southern African Pyrometallurgy 2011 International Conference*, Misty Hills, Muldersdrift, South Africa, 6–9 March 2011. Jones, R.T. and den Hoed, P. (eds.). Southern African Institute of Mining and Metallurgy, Johannesburg. pp. 295–307.

JACOBS, M. 2006. Process description and abbreviated history of Anglo Platinum's Waterval Smelter. *Proceedings of the Southern African Pyrometallurgy 2006 International Conference*, Cradle of Humankind, South Africa, 5–8 March 2006. Jones, R.T. (ed.). Southern African Institute of Mining and Metallurgy, Johannesburg. pp. 17–28.

KANTZAS, A., BRYAN, J., and TAHERI, S. 2015. Harmonic - average permeability. *Fundamentals of Fluid Flow in Porous Media*. PERM Inc. <https://perm.com/resources/fundamentals-of-fluid-flow-in-porous-media/chapter-2-the-porous-medium/permeability/harmonic-average-permeability/> [accessed 8 May 2020].

LYONS, J.R. 2008. An estimate of the equilibrium speciation of sulfur vapor over solid sulfur and implications for planetary atmospheres. *Journal of Sulfur Chemistry*, vol. 29, no. 3. pp. 269–279.

MABIZA, L., PICAS, R., NELL, J., MATSETELA, B., and ERASMUS, G. 2011. Characterisation of SO₂ in off-gas at Zimplats Smelter. *Proceedings of the Southern African Pyrometallurgy 2011 International Conference*, Muldersdrift, South Africa, 6–9 March 2011. Jones, R.T. and den Hoed, P. (eds.). Southern African Institute of Mining and Metallurgy, Johannesburg. pp. 161–172.

NOLET, I. 2014. Tapping of PGM-Ni mattes: an industry survey. *Proceedings of the Southern African Furnace Tapping Conference 2014*, Muldersdrift, South Africa, 27–29 May 2014. Southern African Institute of Mining and Metallurgy, Johannesburg. pp. 223–232.

SHAW, A., DE VILLIERS, L.P., HUNDERMARK, R.J., NDLOVU, J., NELSON, L.R., PIETERSE, B., and MCKENZIE, A.D. 2013. Challenges and solutions in PGM furnace operation: High matte temperature and copper cooler corrosion. *Journal of the Southern African Institute of Mining and Metallurgy*, vol. 113, no. 3. pp. 251–261.

SOFEKUN, G.O., EVOY, E., LESAGE, K.L., CHOU, N., and MARRIOTT, R.A. 2017. The rheology of liquid elemental sulfur across the gamma-transition. *Journal of Rheology*, vol. 62, no. 2. pp. 469–476.

TETHWAYO, B.M. and GARBERS-CRAIG, A.M. 2010. Corrosion of copper coolers in PGM smelters. *Proceedings of the 4th International Platinum Conference: Platinum in Transition 'Boom or Bust'*, Rustenburg, South Africa, 11–14 October 2010. Southern African Institute of Mining and Metallurgy, Johannesburg. pp. 187–188

TETHWAYO, B.M. 2010. Sulphidation of copper coolers in PGM smelters. MSc thesis, University of Pretoria, South Africa.

TETHWAYO, B.M. and GARBERS-CRAIG, A.M. 2011. Laboratory scale investigation into the corrosion of copper in a sulphur-containing environment. *Corrosion Science*, vol. 53. pp. 3068–3074. ◆



Characterization of surface roughness and subsurface pores and their effect on corrosion in 3D-printed AlSi10Mg

S. Thuketana^{1*}, C. Taute¹, H. Möller¹, and A. du Plessis^{2,3}

*Paper written on project work carried out in partial fulfilment of B.Eng (Metallurgical Engineering)

Affiliation:

¹Department of Materials Science and Metallurgical Engineering, University of Pretoria, Pretoria, South Africa.

²Research Group 3DInnovation, Stellenbosch University, Stellenbosch, South Africa.

³Department of Mechanical Engineering, Nelson Mandela University, Port Elizabeth, South Africa.

Correspondence to:

H. Möller

Email:

Heinrich.moller@up.ac.za

Dates:

Received: 30 Nov. 2019

Revised: 2 May 2020

Accepted: 26 May 2020

Published: June 2020

How to cite:

Thuketana, S., Taute, C., Möller, H., and du Plessis, A. Characterization of surface roughness and subsurface pores and their effect on corrosion in 3D-printed AlSi10Mg. The Southern African Institute of Mining and Metallurgy

DOI ID:

<http://dx.doi.org/10.17159/2411-9717/1053/2020>

ORCID ID:

S. Thuketana
<https://orcid.org/0000-0002-8408-4429>

C. Taute

<https://orcid.org/0000-0001-5771-3915>

H. Möller

<https://orcid.org/0000-0001-6075-9965>

A. du Plessis

<https://orcid.org/0000-0002-4370-8661>

Synopsis

Denel Dynamics, a South African armaments development and manufacturing company, is interested in introducing additive manufacturing (AM) in the fabrication of missile components. The practicality of using AM for industrial applications, considering its unique challenges, was questioned. To investigate this, defects (surface roughness and porosity) associated with AlSi10Mg parts produced by laser powder bed fusion were characterized. In this case study, 40 rectangular, 30 mm × 20 mm × 4 mm samples, 20 of which were 'smooth' (3.7 µm *Ra*) and 20 'rough' (7.3 µm *Ra*), were analysed. The surface roughness, porosity volume percentage, and the porosity type were characterized using stereo, optical, and scanning electron microscopy as well as nano-CT scans. The pores were observed to be located in the subsurface of the samples. The smooth and rough samples were found to have subsurface pores mainly positioned between 100–650 µm and 220–600 µm from the surface, respectively. To improve the surface roughness, the samples were polished by centrifugal barrel finishing (CBF). Smooth (polished) and unpolished samples were corroded using potentiodynamic tests in a 3.5% NaCl solution. The smooth, polished samples were found to undergo more corrosion than the unpolished samples. This unexpected result could be explained by the subsurface pores of the polished samples being exposed after surface layers were removed during CBF. The location of porosity in 3D printed samples is therefore of high importance when surface polishing is done before exposure to a corrosive environment. Even though CBF decreases the surface roughness, subsurface pores that are exposed during polishing are detrimental to pitting corrosion resistance. Laser shock peening, which has been found to successfully close pores as deep as 700 µm without compromising the surface roughness, is suggested as a possible solution.

Keywords

additive manufacturing, laser powder bed fusion, surface roughness, porosity, corrosion.

Introduction

Additive manufacturing (AM) has the ability to produce complex structures directly from a design without the need for expensive tooling. The need to assemble multiple components is reduced and intricate parts can be produced in one step (Debroy, 2018). The standard terminology for AM, ISO/ASTM 52900:2015 (E), defines powder bed fusion (PBF) as a 'manufacturing process in which thermal energy selectively fuses regions of a powder bed'. PBF uses either a focused laser beam or an electron beam; this study will focus on laser powder bed fusion (L-PBF). L-PBF entails some challenges introduced by the repeated melting, rapid solidification thermal cycles, directional heat extraction, and repeated solid-state transformations during the printing process (Cabrin *et al.*, 2018). The challenges include, but are not limited to, the difficulty in producing dense parts, residual stresses which result in distortion and cracking, and high surface roughness and the subsequent requirement for post-processing (Aboukhair *et al.*, 2014). The powders used to fabricate the parts play an important role in determining their quality. The powders may be characterized in terms of morphology, density, and flowability. Spherical powders are used to produce dense parts in complex designs, particularly when the material of construction includes precious metals such as platinum (Pt), rhodium (Rh), iridium (Ir), and their alloys (Bisset and van der Walt, 2017).

AlSi10Mg powder is the most commonly used material to produce aluminium alloy parts via L-PBF. AlSi10Mg is a near-eutectic alloy in which the eutectic Si counters solidification shrinkage, hence reducing the printed part's susceptibility to cracking. The size distribution and particle shape of the powder play a critical role in determining the quality of the built part. Spherical particles give good flowability, resulting in uniform layers on the built part. The particle size distribution also affects the interaction between the laser and powder bed. Fine particles have an adverse influence on flowability, and large particles require higher laser energy to cause melting. Powder particles with internal porosity can introduce porosity to the built part (Lumley, 2018).

Characterization of surface roughness and subsurface pores and their effect on corrosion

Surface roughness in laser powder bed fusion

Depending on the process parameters and powder size used, the typical surface roughness of aluminium components produced by L-PBF ranges between 8 μm and 20 μm Ra (Cabrini *et al.*, 2016). Before polishing, the texture exhibits an excessive number of cavities and other surface imperfections such as limited bonding of particles to the substrate material (Leon and Aghion, 2017). According to Nasab *et al.* (2018) there are three main surface defects that cause L-PBF parts to have high surface roughness – balling, spatter particles, and partially melted powder. Balling is a result of a division effect of an elongated melt pool. Spatter particles are usually about 200 μm in size. When particles spatter from the melt pool and land within the powder bed surface, they are remelted together with the following layer. If, however, the spatters are close to the contour, they will only be partially melted and remain attached to the surface. The partially melted powder is the same size as the powder particles, which is typically between 20 μm and 50 μm .

Porosity in laser powder bed fusion

The scanning speed and energy density play opposing roles in the type of pores formed within a part. Energy density can refer to volumetric energy density (ψ), defined by the combined effect of laser power (P), scanning speed (v), hatch spacing (h), and powder layer thickness (t), as seen in Equation [1] (Lumley, 2018). It can also refer to linear energy density (Φ), defined by the combined effect of laser power and scanning speed, as seen in Equation [2] (Wang, 2011).

$$\psi = \frac{P}{v \times h \times t} \quad [1]$$

$$\Phi = \frac{P}{v} \quad [2]$$

At high scanning speeds, metallurgical pores (commonly known as 'lack of fusion' pores) have been observed. These pores are irregular in shape and are present due to incomplete melting. At low scanning speeds, keyhole pores have been observed. These are spherical in shape and are a result of trapped metal vapour in a deeply penetrating melt pool (Lumley, 2018). The number of pores can be minimized at intermediate energy densities and scanning speeds, but never completely eliminated (Tang, Pistorius, and Beuth, 2017). In a study by du Plessis (2019), a range of process parameter changes and their effect on subsurface pore distributions in L-PBF parts was demonstrated. Optimal parameters achieved up to 99.99% density (0.01% porosity). The different pore formation mechanisms and their resulting morphologies and 3D distributions were reported. The optimal energy densities differ from material to material and machine to machine.

Laser powder bed fusion parameters

There are many variables considered in L-PBF. Aboulkhair *et al.* (2014) categorize them as laser-, scan-, powder-, and temperature-related. When one of these variables is changed, the quality of the built part may be affected. The effect may be seen in the microstructure, crystallographic texture, surface roughness, and/or the density. An increase in hatch spacing has been found to cause pores to become more irregular in shape, thus decreasing the density of L-PBF parts. Balling increases with greater scanning speed, resulting in a lower surface quality

part (Aboulkhair *et al.*, 2014). Shielding gas flow has also been observed to affect the built part's quality (Philo, 2017). Shielding gas flow in L-PBF is used mainly to provide an inert atmosphere to reduce reactive gas pickup at the liquid metal, chiefly to avoid oxidation and nitration. This is particularly common during the production of aluminium alloys. Inhomogeneous gas flow over a build platform results in insufficient removal of by-products such as spatter, hence increasing the surface roughness.

Corrosion of aluminium alloys

Effect of surface roughness on corrosion

The rough surface from L-PBF causes some changes in corrosion behaviour. Cabrini *et al.* (2016) stated that the passive film formed on aluminium alloys during L-PBF is less protective than the oxide spontaneously formed in air. Leon and Aghion (2017) investigated the effect of AM surface roughness defects on corrosion after exposure of AlSi10Mg samples to 3.5% NaCl for 30 days. The study found that the polished samples showed better corrosion resistance than the unpolished samples. Corrosion attack at the unpolished surface was manifest by multiple sites of pitting and an increase in corrosion products. The polished samples displayed shallow pits, whereas the unpolished samples showed deeper and more irregularly shaped pits. The study linked the reduced corrosion resistance of unpolished samples to increased surface roughness in the form of large cavities and other surface defects that were caused by the L-PBF process.

Effect of porosity on corrosion

Pores act as preferential initiation sites for localized corrosion (Cabrini *et al.*, 2016). Leon, Shirizly, and Aghion (2016) compared AlSi10Mg produced through L-PBF and a gravity-cast alloy. The corrosion fatigue endurance of the L-PBF alloy was found to be better than that of the gravity cast alloy. This was attributed mainly to the significant differences between the microstructure and porosity. It is believed that the accelerated cracking in the cast alloy was due to the synergistic effect of the corrosive environment and the stress concentration from the irregular pores in the gravity-cast alloy. Although the printed alloy had the best corrosion resistance of the two alloys, it was concluded that the AM porosity defect affected the corrosion resistance of the alloy adversely due to the corrosion attack progressing along the melt pool overlap, which lacked fusion pores caused by L-PBF. Due to the significant influence of porosity on corrosion resistance, the effect of the different microstructures was not ascertained conclusively.

Principle objective and scope of work

South Africa had a late start with AM, the first system becoming available in 1991. Now, however, a complete value chain has developed, with a well-balanced mix of basic and applied research (de Beer, 2011). As AM continues to grow and develop in South Africa, more industries have shown interest in the technology. Denel Dynamics, a South African armaments development and manufacturing company, is interested in introducing AM in the fabrication of missile components. The company produces stand-off weapons, air-to-air, ground-to-air, and armour-piercing missiles. These missiles, especially the air-to-air and stand-off weapons, can be exposed to a salt atmosphere. This makes good corrosion resistance an important factor in determining whether to adopt AM technology. This project aimed to characterize the

Characterization of surface roughness and subsurface pores and their effect on corrosion

defects associated with AlSi10Mg parts produced through L-PBF that could possibly limit industrial applications. This was done by investigating the location of pores in the built parts, as this affects both corrosion resistance and fatigue life. The analysis was completed using nano-CT scans and optical, stereo, and scanning electron microscopy. Post-processes to improve surface roughness and porosity were also explored. This study was conducted as a final year undergraduate research project in the Department of Materials Science and Metallurgical Engineering at the University of Pretoria. Further research is planned and the topic will be expanded to include related in-depth aspects in future

Materials and methods

Tests were carried out on 40 L-PBF AlSi10Mg samples obtained using a SLM250 metal 3D printer (Wuibox, China). The build-direction of the samples was in the X-Y plane. Half of the printed samples were received as 'rough' ($7.3 \mu\text{m } Ra$) and the other as 'smooth' ($3.7 \mu\text{m } Ra$) in surface. The smooth samples were placed closer to the gas outlet, which is believed to have caused the difference in the surface roughness. The laser, scan, powder, and temperature parameters were kept constant. All the samples were $30 \text{ mm} \times 20 \text{ mm} \times 4 \text{ mm}$ in size, as shown in Figure 1.

All samples were weighed and dimensions and surface roughness measured upon arrival. Half the smooth and rough samples were polished by CBF using a HZ-40 machine (Mass Finishing Incorporated, USA). A representative number (>50%) of each sample type (as-received and polished) was measured. Each sample was measured at least three times for validity and repeatability. Surface roughness was measured using a mobile surface roughness machine (Zeiss Surfcom Flex Measuring System, ACRRETECH, Japan) that was calibrated and the stylus checked before the start of measuring. The surface quality was analysed using stereomicroscopy (Olympus SZX7 spectroscope, Japan). Porosity analysis was carried out by optical microscopy (Olympus BX51M, Japan) and nano-computer-aided tomography (CT) scans (du Plessis, le Roux, and Guelpa, 2016). The use of X-ray computed tomography in the field of additive manufacturing has been reviewed in detail by du Plessis *et al.* (2018). Surface roughness defects were then analysed using scanning electron microscopy (Jeol JSM-IT300LV, Japan).

Smooth, polished, and unpolished samples were corroded in a 3.5% NaCl solution by a potentiodynamic test using a potentiostat (PGSTAT302N, Metrohm, Switzerland). This was done to show the corrosion behaviour of the samples in an extreme corrosive

environment. A three-electrode cell was used. The reference electrode was Ag/AgCl and platinum was the counter-electrode. Scanning was from -0.3 V to $+0.3 \text{ V}$ relative to the open circuit potential with a scanning rate of 0.125 mV/s . After the tests were completed, the sample surfaces were examined using optical microscopy (Olympus BX51M, Japan).

Results

Surface roughness

Figure 2 shows cross-sections of smooth and rough as-received samples from the Y-Z plane. The top black part (a) is Bakelite resin and the grey part (b) is the sample (all cross-sections in this report show the resin as black). In both the samples, 'valleys and peaks' were observed, with those in the rough sample being more prominent.

The surface roughness of the smooth samples measured from the X-Z plane ranged from $2.8 \mu\text{m}$ to $4.0 \mu\text{m } Ra$ with an average of $3.7 \mu\text{m } Ra$. A surface defect, encircled in Figure 2 (2), and shown in a close-up view in Figure 3, was identified on the rough sample surface. The defect was identified as partially melted powder due to its size being between 20 and $50 \mu\text{m}$ (Nasab *et al.*, 2018). These types of defect, together with the 'valleys' and 'peaks', caused a higher surface roughness in the rough samples. The rough sample surface roughness ranged from $5.5 \mu\text{m}$ to $9.5 \mu\text{m } Ra$, with an average of $7.3 \mu\text{m } Ra$, as measured from the X-Z plane.

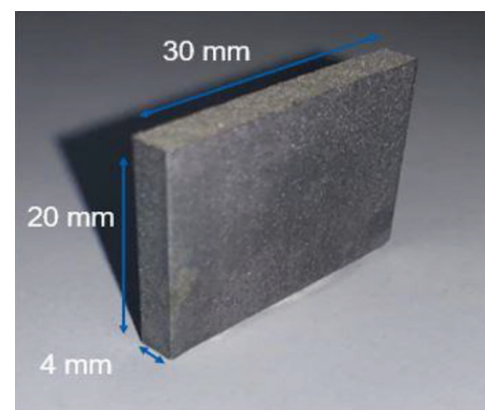


Figure 1 – Schematic representation of sample dimensions

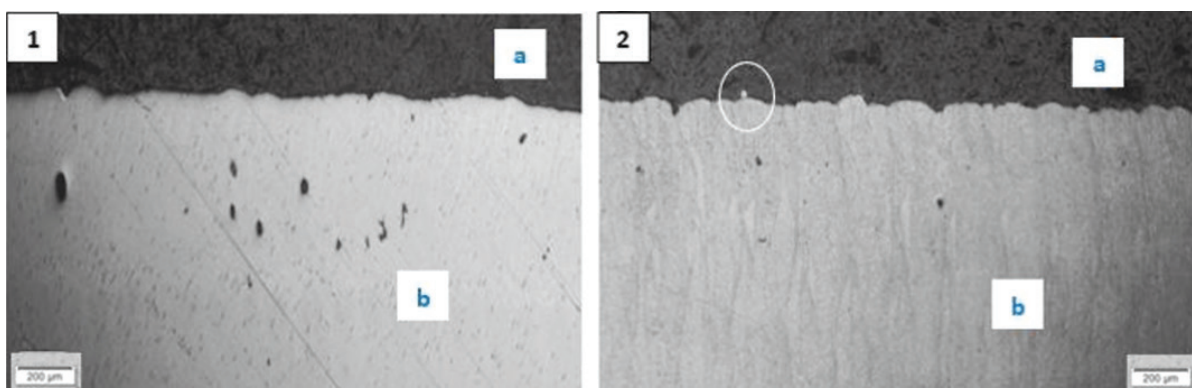


Figure 2 – Cross-sections of smooth (1) and rough (2) AlSi10Mg samples

Characterization of surface roughness and subsurface pores and their effect on corrosion

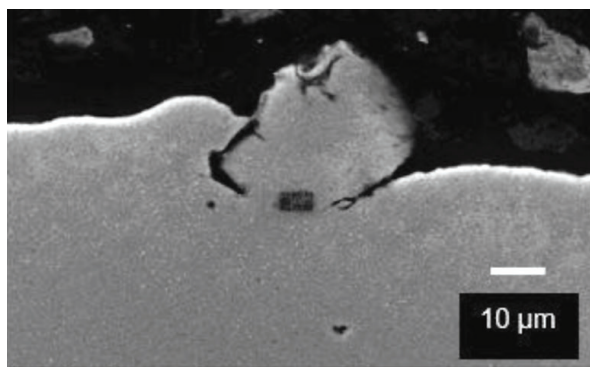


Figure 3—Partially melted powder identified on a rough sample surface

Porosity

Nano-CT scans were used for the 3D quantification of porosity. Figure 4 is a nano-CT image of one of the ‘smooth’ samples that shows characteristics of both the smooth and rough samples. The size range of the pores and the porosity volume percentage for both types of sample are given in Table I. The porosity volume percentage of the smooth samples were observed to be slightly higher (by 0.02%) than for the rough samples. The pores for the X-Y plane built-direction samples were identified as subsurface, contour pores (du Plessis and le Roux, 2018). Figure 5 depicts both a nano-CT scan and an optical microscope image to show that the pores mainly line up to form a porous layer. Large pores can be found outside the layer at the corners of the samples. The

encircled pore in Figure 5b presents a high risk for decreasing corrosion resistance as it is very close to the surface, and if exposed would act as an initiation site for localized corrosion.

Post-processing

As discussed in the literature, surface roughness associated with L-PBF can be detrimental to corrosion resistance (Leon and Aghion, 2017). In an attempt to prevent the adverse effects of the surface quality, centrifugal barrel finishing (CBF) was done. Table II summarizes the surface roughness of the different L-PBF samples before and after CBF.

Images of the L-PBF AlSi10Mg samples before and after CBF are shown in Figure 6. From visual inspection, it is apparent that CBF improves the poor surface finish; however, upon further analysis it is seen that a new problem may be introduced. The porous layers of the smooth and rough samples, as well as the layers removed during CBF, were characterized using optical and dimensional analysis. Assuming uniform removal of material, the removed layer described in Table III represents half the material removed per plane.

Table I

Porosity volume percentage and pore size ranges of samples

	Smooth	Rough
Porosity volume (%)	0.1	0.08
Size range (mm)	0.03–0.5	0.04–0.7

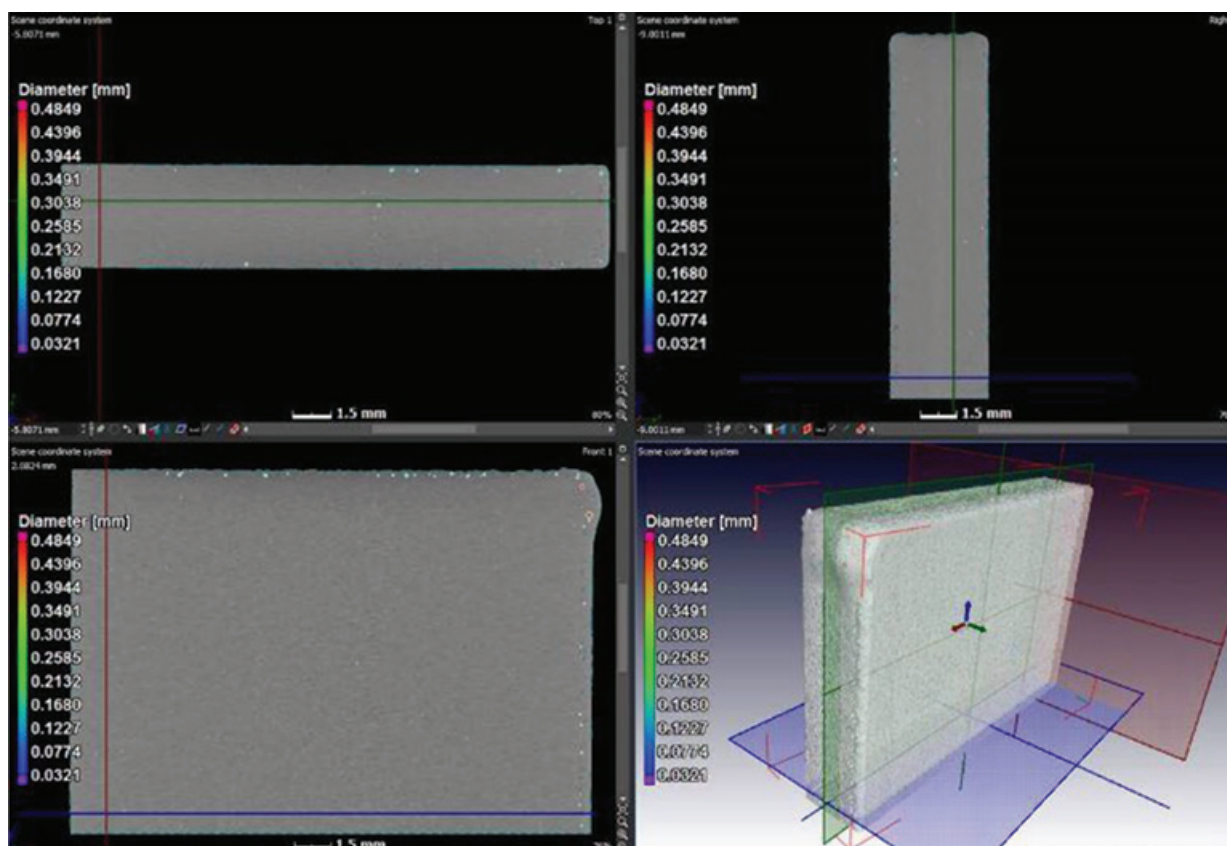


Figure 4—Nano-CT scan image showing subsurface contour porosity on smooth sample with a XY built-direction

Characterization of surface roughness and subsurface pores and their effect on corrosion

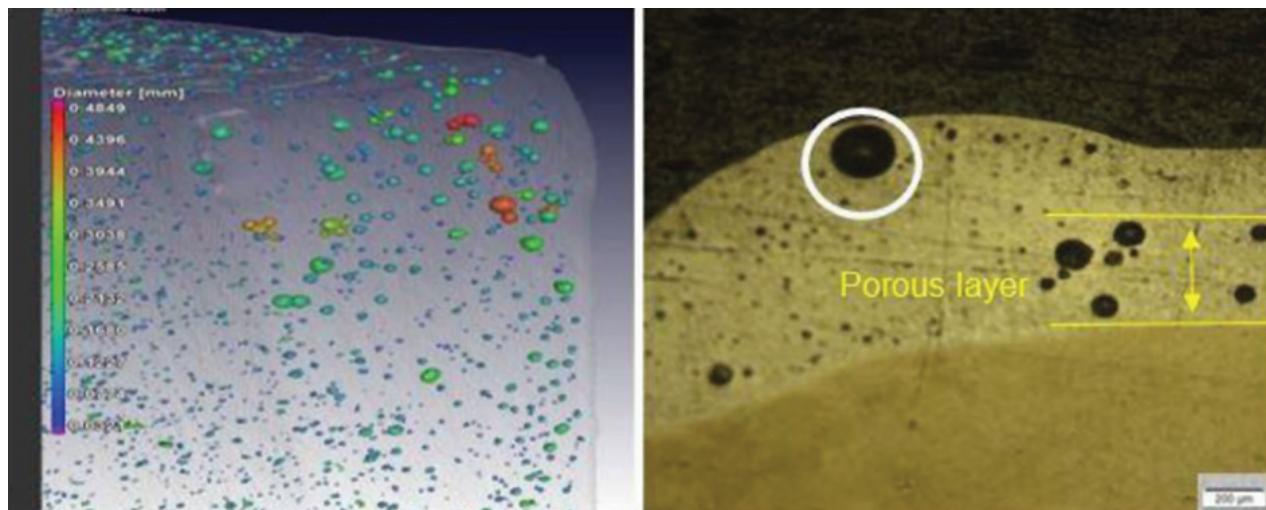


Figure 5—Nano-CT scan (a) and optical microscope (b) images showing the subsurface contour porosity

Table II
Surface roughness measurements

Samples	Smooth L-PBF AISi10Mg	Rough L-PBF AISi10Mg
As-received surface roughness R_a (μm)	3.7	7.3
After CBF surface roughness R_a (μm)	0.35	0.44

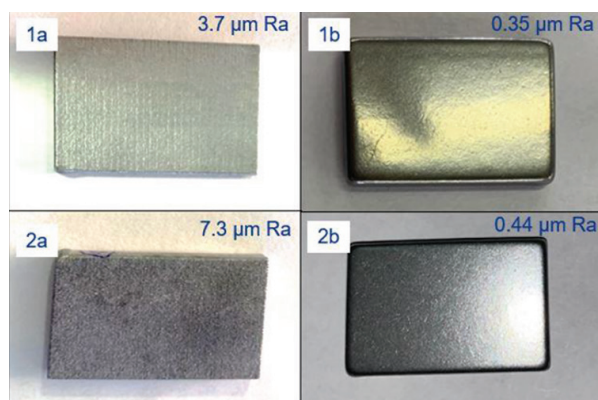


Figure 6—Smooth (1) and rough (2) L-PBF AISi10Mg before (a) and after (b) CBF

Table III
Porous and removed layer of samples

	Smooth	Rough
Distance from the surface (μm)	100–650	220–600
Layer removed from CBF (μm)	100–200	100–150

Table III reveals how the subsurface pores in the smooth samples were at risk of being exposed on the surface. To investigate this, cross-sections of the smooth samples were analysed using optical microscopy and nano-CT scans. Due to CBF, some surface material was removed, bringing the surface closer to the (initially) subsurface pores as shown in Figure 7.

The nano-CT scans showed that the porous layer remains in the subsurface for some samples, and on the surface for others. Some scans, such as the one in Figure 8, revealed some subsurface pore exposure on the surface. The porous layer can be seen on the right-hand side of the sample, with an encircled exposed pore.

To investigate whether the porous layer after CBF affects the corrosion resistance, smooth polished and unpolished samples were corroded using potentiodynamic tests. The visual results from optical microscopy revealed that the polished samples experienced more corrosion, with more prominent pits than the unpolished samples. This can be seen in Figure 9.

Discussion and recommendations

One of the challenges of L-PBF is the difficulty in producing repeatable part quality. This was observed from the difference in surface roughness between the samples. The difference may be due to more spatters being removed by the gas from the smooth samples than from the rough samples (Philo, 2017). This was because the smooth samples were placed closer to the gas outlet, improving the homogeneity of the gas flow.

Previous studies found that surface roughness and porosity influence corrosion resistance negatively; however, these studies analysed the effects of these defects separately (Leon and Aghion, 2017; Leon, Shirizly, and Aghion, 2016). In this investigation we looked at how both these defects together affect corrosion resistance. Based on previous studies, the unpolished samples were expected to experience the most corrosion; however, those studies did not specify where the porosity in the parts was situated. From the present study, in the case of subsurface contour pores it was seen that not just surface pores, but also subsurface pores, may be detrimental to corrosion resistance.

Although the surface roughness of the analysed samples was smoother than is typical for L-PBF surfaces (Cabrini *et al.*, 2016), the surface roughness was still too high for most industrial applications. To improve the surface roughness, layers of the samples had to be removed and in so doing, some subsurface pores were exposed on the surface. When pores are exposed, the chance of pitting corrosion increases and fatigue life is likely to decrease. The reason for the observed results, that

Characterization of surface roughness and subsurface pores and their effect on corrosion

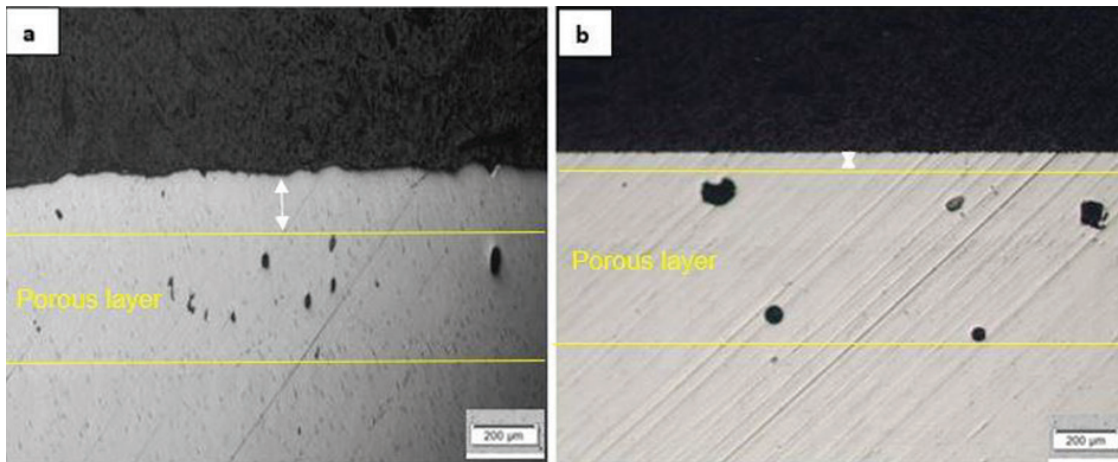


Figure 7—Optical microscopy images of before (a) and after (b) centrifugal barrel finishing of the smooth AISi10Mg samples



Figure 8—Nano-CT scan image showing the exposure of a pore within the porous layer of a smooth sample

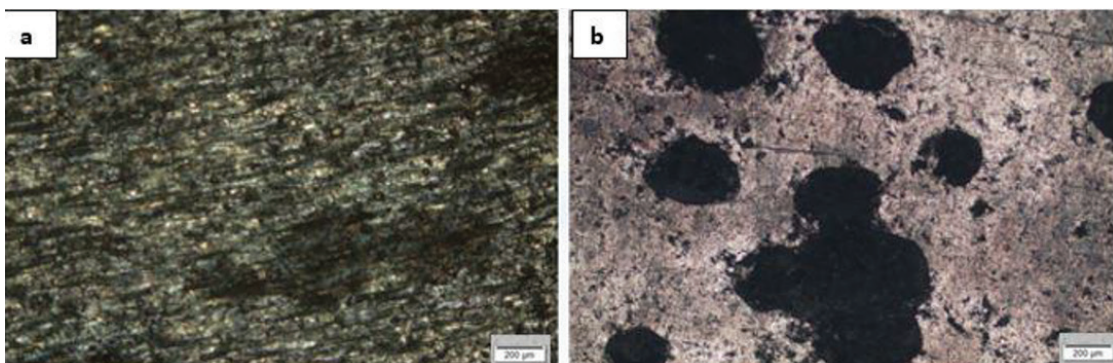


Figure 9—Corroded surface of unpolished (a) and polished (b) smooth L-PBF AISi10Mg

the polished samples suffer increased corrosion attack compared with the unpolished, may be the presence of potentially exposed pores. Should the pores be successfully closed, the use of AM to fabricate missile parts may be viable. The first recommendation is prevention. Process parameters should be improved in order to

remove all subsurface pores; these can be checked using X-ray tomography. Post-processing may be used.

Hot isostatic pressing (HIP) is a high-pressure (400–2070 bar) pore elimination process that uses high temperatures (up to 2 000°C). It can achieve 100% of maximum theoretical density,

Characterization of surface roughness and subsurface pores and their effect on corrosion

owing to the omnidirectional pressure that is applied and the high temperature that allows for easier deformation. The process also improves ductility and fatigue resistance. As AM is rapidly taking hold in demanding markets such as aerospace, many companies have considered applying post-build HIP treatment. Today HIP is the standard procedure to impart longer and predictable lifetimes to fan blades in aircraft engines, and is believed to be the way forward to optimize the material properties of AM parts (Quintus Technologies, 2019). It is recommended, however, that further investigations of this process be carried out as some studies have found the pores to reopen during heat treatments (Tamas-Williams, 2016).

Laser shock peening (LSP) is a process that introduces compressive residual stresses. It is traditionally done to improve fatigue properties in parts. In a study by du Plessis *et al.* (2019), this process was explored to close up pores. The technique proved successful and was able to close pores up to 700 μm subsurface while improving the surface roughness. At higher peening power, where the penetration was deeper than 700 μm , the surface roughness increased. A trade-off between how deeply the pores are closed and the surface quality was observed. It is recommended that further studies look at the effect of LSP on corrosion resistance and whether the pores remain closed during heat treatment.

Conclusion

CBF successfully ameliorated the high surface roughness defect. The roughness of the smooth samples improved from 3.7 μm to 0.35 μm R_a , and that of the rough samples from 7.3 μm to 0.44 μm R_a . However, by improving the surface roughness, the risk of subsurface pores becoming surface pores was introduced in the case of the smooth samples. The porous layer of the smooth samples' was between 100–653 μm , while the CBF process removed layers between 100 and 200 μm . This was believed to have caused the smooth, polished samples experiencing more corrosion than the unpolished samples. Therefore, the presence of surface pores is more detrimental to pitting corrosion resistance than high surface roughness for the samples in the environment investigated.

In contrast to some other studies, the improvement of surface roughness did not lead to a reduction in pitting corrosion. The novelty of this study is that it shows that subsurface pores become exposed by CBF, and then act as initiation sites for pitting corrosion. This study shows that the location of the pores in the samples is of importance. If there is significant subsurface porosity – as in this study – then surface polishing results in increased pitting corrosion by exposing the subsurface pores on the surface. Further investigations on the effects of porosity distribution on corrosion resistance in 3D printed samples, before and after surface polishing, is recommended. If there is no significant subsurface porosity in 3D printed samples, then a reduction in surface roughness is expected to reduce pitting corrosion.

If the pores are closed, the surface roughness may be improved with no risk of exposing pores and this may increase corrosion resistance (*e.g.* Leon and Aghion, 2017). The increased corrosion products on the polished samples were observed on 30 mm \times 20 mm \times 4 mm rectangular parts with a X-Y plane built-direction. The results are not necessarily true for all L-PBF parts. More corrosion tests should be completed to determine repeatability, and include the application of the suggested pore enclosure recommendations.

Acknowledgements

The authors would like to thank Denel Dynamics (Tlissetso Ramolobe), the University of Pretoria staff (Sibusiso Mahlalela, Ruzanne Engelbrecht, and Carel Coetzee), the Stellenbosch University CT scanner facility staff (Muofhe Tshibalanganda and Carlyn Wells), Carl Zeiss Vision SA (Loren Purcell), Mass Finishing Inc (Cole Mathisen), and Wiiboos (Cloud Lu).

Funding

The project was funded by the Collaborative Program on Additive Manufacturing (CPAM) from the Department of Science and Innovation in South Africa.

Authors' contributions

Heinrich Möller: organization of samples and tests, and supervision. Anton du Plessis: nano-CT scanning and supervision. Shonny Thuketana and Carlien Taute: sample preparation and optical analysis. The report was written by Shonny Thuketana and reviewed by all the authors.

References

- ABOULKHAIR, N.T., EVERITT, N.M., ASHCROFT, I., and TUCK, C. 2014. Reducing porosity in AlSi10Mg parts processed by selective laser melting. *Additive manufacturing*, vol. 1-4. pp. 77–86.
- BISSET, H. and VAN DER WALT, I.T. 2017. Metal and alloy spheroid for the advanced metals initiative of South Africa, using high-temperature radio-frequency plasmas. *Journal of the Southern African Institute of Mining and Metallurgy*, vol. 117. pp. 975–980.
- CABRINI, M., CALIGNANO, F., FINO, P., LORENZI, S., LORUSSO, M., MANFREDI, D., TESTA, C., and PASTORE, T. 2018. Corrosion behaviour of heat-treated AlSi10Mg manufactured by laser powder bed fusion. *Materials (Basel)*, vol. 11, no. 7. pp. 2–14.
- CABRINI, M., LORENZI, S., PASTORE, T., PELLEGRINI, S., FINO, P., AMBROSIO, E.P., CALIGNANO, F., and MANFREDI, D. 2016. Corrosion resistance of direct metal laser sintering AlSi10Mg. *Surface and Interface Analysis*, vol. 48, no. 8. pp. 818–826.
- DE BEER, D.J. 2011. Establishment of rapid prototyping/additive manufacturing in South Africa. *Journal of the Southern African Institute of Mining and Metallurgy*, vol. 111. pp. 211–215.
- DEBROY, T., WEI, H.L., ZUBACK, J.S., MUKHERJEE, T., ELMER, J.W., MILEWSKI, J.O., BEESE, A.M., WILSON-HEID, A. DE, A., and ZHANG, W. 2018. Additive manufacturing of metallic components – Process, structure, and properties. *Progress in Materials Science*, vol. 92. pp.112–224.
- DU PLESSIS, A. 2019. Effects of process parameters on porosity in laser powder bed fusion revealed by X-ray tomography. *Additive Manufacturing*, vol. 30. pp. 100871.
- DU PLESSIS, A., GLASER, D., MÖLLER, H., MATHE, N., TSHABALALA, L., MFUSI, B., and MOSTERT, R. 2019. Pore closure effect of laser shock peening of additively manufactured AlSi10Mg. *3D Printing and Additive Manufacturing*, vol. 6, no. 5. pp. 1–16.
- DU PLESSIS, A. and LE ROUX, S.G. 2018. Standardized X-ray tomography testing of additively manufactured parts: A round robin test. *Additive Manufacturing*, vol. 24. pp. 125–136.
- DU PLESSIS, A., YADROITSEV, I., YADROITSAVA, I., and LE ROUX, S.G. 2018. X-ray microcomputed tomography in additive manufacturing: a review of the current technology and applications. *3D Printing and Additive Manufacturing*, vol. 5, no. 3. pp. 227–247.

Characterization of surface roughness and subsurface pores and their effect on corrosion

- LEON, A., SHIRIZLY, A., and AGHION, E. 2016. Corrosion behavior of AlSi10Mg alloy produced by additive manufacturing (AM) vs. its counterpart gravity cast alloy. *Metals*, vol. 6, no. 7. pp. 148–157.
- LEON, A. and AGHION, E. 2017. Effect of surface roughness on corrosion fatigue performance of AlSi10Mg alloy produced by selective laser melting (SLM). *Materials Characterization*, vol. 131. pp. 188–194.
- LUMLEY, R. 2018. *Fundamentals of Aluminium Metallurgy – Recent Advances: 2. Additive Manufacturing of Aluminium Based Alloys and Composites*. 1st edn. Woodhead Publishing, VIC, Australia.
- NASAB, M.H., GASTALDI, D., LECIS, N.F., and VEDANI, M. 2018. On morphological surface features of the parts printed by selective laser melting (SLM). *Additive Manufacturing*, vol. 24. pp. 373–377.
- PHILO, A.M., SUTCLIFFE, C.J., SILLARS, S., SIENZ, J., BROWN, S.G.R., and LAVERY, N.P. 2017. A study into the effect of gas flow inlet design of the Renishaw AM250 laser powder bed fusion machine using computational modelling. *Proceedings of the*

28th Annual International Solid Freeform Fabrication Symposium, Austin, TX, 7–9 August 2017. Solid Freeform Fabrication, USA. pp. 1203–1219.

QUINTUS TECHNOLOGIES. 2019. Hot isostatic pressing (HIP) supporting the additive industry. https://quintustechnologies.com/hot-isostatic-pressing/applications/hip-supporting-the-casting-industry/?gclid=EA1aIQobChMltruLsdHi6QIVKYBQBh34vgsxEAAAYASAAEgJNRPD_BwE [accessed 28 November 2019].

TAMMAS-WILLIAMS, S., WITHERS, P.J., TODD, I., and PRANGELL, P.B. 2016. Porosity regrowth during heat treatment of hot isostatically pressed additively manufactured titanium components. *Scripta Materialia*, vol. 122. pp. 72–76.

TANG, M., PISTORIUS, P.C., and BEUTH, J.L. 2017. Prediction of lack-of-fusion porosity for powder bed fusion. *Additive Manufacturing*, vol. 14. pp. 39–48.

WANG, L., WEI, Q.S., SHI, Y.S., LIU, J.H., and HE, W.T. 2011. Experimental investigation into the single track of selective laser melting of IN625. *Advanced Materials Research*, vol. 233–235. pp. 2844–2848. ◆

UNIVERSITY OF PRETORIA DEPARTMENT OF MINING ENGINEERING

TOP FEATURES



Academic offering

Undergraduate students:
BEng Mining Engineering

Postgraduate students:
Honours, master's and doctoral degree programmes in mining engineering and applied science mining

**TOP
100**

The University of Pretoria is ranked among the top 100 universities for mining and mineral engineering in the world in the recent Academic Ranking of World Universities (ARWU) rankings

INTERACTIVE IMMERSIVE TECHNOLOGY

The Department's state-of-the-art Virtual Reality Centre forms the core of the Department's interactive immersive technology drive. This has been expanded to include a blast wall. These facilities provide training in a "practical" environment through the use of virtual reality.

INDUSTRY-RELEVANT SHORT COURSES

The Department makes its expertise available to members of industry for purposes of professional development, as well as skills development and capacity building.

View the mining short courses available:
www.enterprises.up.ac.za

LEADERSHIP DEVELOPMENT

The Department's Murray & Roberts Mining Engineering Leadership Academy (M&R MELA) was established with the aim of grooming students for the workplace. The programme focuses on working in teams, emotional intelligence and conflict management for young engineers.

www.up.ac.za/mining-engineering



Faculty of Engineering,
Built Environment and
Information Technology

Fakulteit Ingenieurswese, Bou-omgewing en
Inligtingsteun / Lefapha la Boetšenero,
Tikologo ya Kago le Theknološi ya Tshedimošo

#UPMiningMatters



On the interactions of iron sulphide with alumina and silica

R.K. Hlongwa^{*1}, B.M. Thethwayo¹, and A.F. Mulaba-Bafubiandi¹

^{*}Paper written on project work carried out in partial fulfilment of BTech (Metallurgical Engineering) degree

Affiliation:

¹University of Johannesburg, Mineral Processing and Technology Research Centre, Department of Metallurgy, School of Mining, Metallurgy and Chemical Engineering, Faculty of Engineering and the Built Environment, Johannesburg, South Africa.

Correspondence to:

B.M. Thethwayo

Email:

77mpilot@gmail.com

Dates:

Received: 28 Nov. 2019

Revised: 2 Jun. 2020

Accepted: 3 Jun. 2020

Published: June 2020

How to cite:

Hlongwa, R.K. Thethwayo, B.M., and Mulaba-Bafubiandi, A.F. On the interactions of iron sulphide with alumina and silica. The Southern African Institute of Mining and Metallurgy

DOI ID:

<http://dx.doi.org/10.17159/2411-9717/1035/2020>

ORCID ID:

B.M. Thethwayo,
<https://orcid.org/0000-0001-9929-8828>

A.F. Mulaba-Bafubiandi

<https://orcid.org/0000-0001-9752-3657>

Synopsis

The hypothesis that matte will only react with certain constituents of a refractory brick, as opposed to the entire brick, was tested by observing the extent of possible reactions between iron sulphide (FeS) and the refractory oxides silica and alumina. The main aim was to identify the components of the alumina-chrome refractory brick which are most reactive with the matte. Pellets comprised of FeS and either SiO₂ or Al₂O₃ were enclosed in a graphite crucible and reacted in a horizontal tube furnace for one hour at 1200°C, 1350°C, or 1500°C in an argon atmosphere. The specimens were analysed with SEM and XRD to determine the extent of any reactions. Results showed that FeS penetration into the silica grain was more prominent with increasing temperature, while alumina was not penetrated by FeS at all temperatures. At 1200°C, no significant reactions were observed for both reaction couples; however, at 1350°C and 1500°C intermediate products were observed. For example, an FeS-FeO mixture, SiS-O, and nonstoichiometric oxides with excess oxygen were detected in the products. SiO₂ was also more reactive towards FeS. Thus, the postulation that brick components may individually be reactive towards matte was proved to be true.

Keywords

FeS-FeO-SiO, FeS-Al₂O₃, matte-refractory interaction, oxide-sulphide reactions.

Introduction

Refractory bricks used in lining PGM smelters can be alumina-chrome or magnesia-chrome based. In modern PGM furnace linings, graphite blocks have replaced these oxide refractories in the feed and slag zones. The use of graphite has improved the service life of the refractory lining by obstructing migration of furnace contents towards the copper coolers (Thethwayo and Garbers-Craig, 2014, Thethwayo and Cromarty, 2015). The study of the interaction between the refractory bricks and matte at different temperatures enables informed decisions in refractory innovation and increases knowledge of materials which are less likely to react with and/or dissolve into the matte.

A typical industrial PGM matte consists of Cu-Fe-Ni-S compounds and up to 10% by weight of oxide inclusions (Thethwayo and Cromarty, 2015, Thethwayo, 2019). The structure of a typical industrial matte sample is shown in Figure 1, in which the mode of occurrence of the oxide inclusions in the matte is displayed. The matte and oxide inclusions for the current study were analysed with an electron probe micro-analyser to determine the chemical composition of the phases. The matte was composed of (Fe, Ni)₉S₈, FeS and Cu₅FeS₄, and no slag elements *i.e.* (Al, Ca, Cr, Mg, Na, and Si) were detected in the sulphide phases. The oxide inclusions were composed of (Al, Ca, Fe, Mg)Si₂O₅, (Al, Si)O₂, (Ca, Na) (Al, Si)₄O₈, (Fe, Mg)SiO₃, Fe₂SiO₄, FeCr₂O₄ (Thethwayo, 2019), CaAl₂Si₂O₈, and SiO₂ (du Toit, Cromarty, and Garbers-Craig, 2016). The oxide phases did not have elements associated with the matte, *i.e.* Cu, Ni, and S. Fe can either be in the matte as a sulphide or in the slag as an oxide/silicate (Thethwayo 2019, du Toit, Cromarty, and Garbers-Craig, 2016). Based on the composition and the occurrence of the oxides in Figure 1, the oxides appear to be inclusions in the matte, and there was no evidence of oxide dissolution in it.

The presence of oxide inclusions in the matte causes major challenges to furnace operations due to the formation of spinel phases which hinder matte-slag separation in converters. The presence of chromite increases the liquidus temperature of the slag, which necessitates elevated operating temperatures in the converting step (Eksteen, 2011; Hundermark, 2011). The high operating temperatures affect the operations and reduce the lifespan of the reaction vessels. The oxide inclusions are capable of reacting with the matte and altering its composition (Thethwayo and Cromarty, 2015). Contaminated matte also poses a challenge for the subsequent step in matte processing.

On the interactions of iron sulphide with alumina and silica

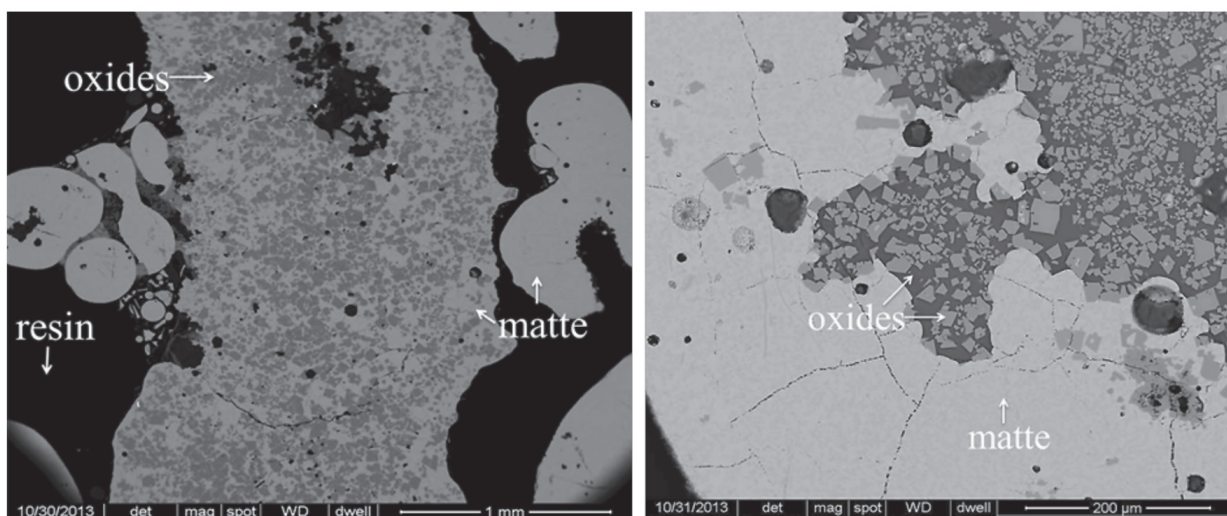


Figure 1—An SEM-BSE image illustrating the morphology of a typical industrial matte sample with oxide inclusions (Thethwayo, 2019)

The source of oxides in the matte can either be the slag or the oxide refractories (Thethwayo, 2019). A typical alumina-chrome brick consists of 75% Al_2O_3 , 20.7% Cr_2O_3 , 2.2% P_2O_5 , and 1% SiO_2 (du Toit, Cromarty, and Garbers-Craig, 2016). On the other hand, a magnesia-chrome brick contains 58% MgO , 19% Cr_2O_3 , 14% Fe_2O_3 , 6.5% Al_2O_3 , 1.1% CaO , and 0.6% SiO_2 (Eksteen, 2011).

Comparing the composition of the refractory brick and that of the oxide inclusions discussed above, there is a probability that the refractory brick is the source of some of the oxide inclusions in the matte. Above 1500°C the matte is capable of sulphurizing the magnesia-chrome brick. High temperatures and sulphidation reactions lead to the decomposition of the refractory, which is undesirable (Eksteen 2011). The destruction of the refractory brick causes furnace breakdowns, operational downtime, and loss of overall production due to maintenance and replacement of the damaged bricks.

The mechanism for oxide migration into matte has not been reported. Ramakobya, Thethwayo, and Mulaba-Bafubiandi (2019) studied the interaction of FeS with Cr_2O_3 and $\text{Fe/MgCr}_2\text{O}_4$. $\text{Fe/MgCr}_2\text{O}_4$ caused volume expansion of FeS at 1200°C; as the temperature increased to 1450°C, a new phase was observed (FeS Cr) with up to 8 weight % Cr (Ramakobya, Thethwayo, and Mulaba-Bafubiandi, 2019). The formation of FeS-Cr proved that FeS has a capability to destroy the refractory brick by extracting Cr into solution.

This project aimed to study the probability of FeS dissolving some refractory components into solution at typical matte operating temperatures of 1200°C, 1350°C, and 1500°C. Only FeS was used to represent the matte, and only Al_2O_3 and SiO_2 were tested as refractory components. This was to simplify the test work and to isolate the matte components since the entire matte has a complex composition and not all the matte components may be reactive. Similarly, two brick components were used instead of the entire brick to verify the hypothesis that PGM matte reacts chemically with certain refractory components, and not the entire brick.

Materials and experimental methods

The reactants used were iron sulphide, silica, and alumina, which

were acquired from Sigma Aldrich and Associated Chemical Enterprises. The as-received powders were characterized using X-ray fluorescence (XRF) and X-ray diffraction (XRD).

Diffraction patterns of as-received samples and generated products were acquired using a Rigaku Ultima IV instrument. The voltage and the current of the X-ray source were set to 40 kV and 30 mA respectively. The instrument had a CuK ($\lambda=1.54$) X-ray generator target with a maximum power of 3 kW.

As-received powder samples were pulverized to $\sim 75 \mu\text{m}$. For XRF analysis, the sample was mixed with wax and pressed into a pellet. The generated products were characterized with scanning electron microscopy (SEM), and XRD. A camera was used to acquire images of the pellets before and after exposure.

The SEM used was a TESCAN (Vega 3XMU) equipped with a tungsten filament as an electron source and was fitted with a backscattered electron (BSE) detector and an energy dispersive X ray spectroscopy (EDS) detector. The BSE detector used for image acquisition employed Vega software. EDS was used to determine the chemical composition of the detected phases using INCA software from Oxford Instruments. The standard for SEM calibration was pure copper, while the beam energy used was 20 keV.

SEM was used for analysing pellets after exposure. These were cut longitudinally to prepare a cross section. Samples were cold-mounted in epoxy resin and sections were polished to the finest size of 1 MD nap. They were then coated with carbon before SEM analysis.

Experimental procedure

The as-received powder samples were milled to less than 100 μm to ensure homogeneity of the sample. The ratio of the reactant mixture in each pellet was 10 g FeS to 2 g Al_2O_3 or SiO_2 . This ratio was selected based on the amount of oxide inclusions in the matte. The weighed aliquot powders were pressed into a 20 mm diameter pellet using a press and die. The pellet was enclosed in a graphite crucible with a lid to isolate the specimen from the environment. An alumina plate was placed between the crucible and the specimen to prevent contact between the specimen and the crucible. The specimen set-up is illustrated in Figure 2.

On the interactions of iron sulphide with alumina and silica

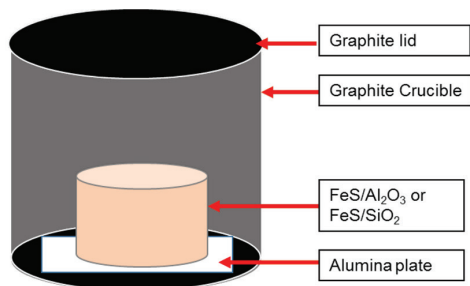


Figure 2—Experimental set-up

A horizontal tube furnace was heated with silicon carbide elements, and an alumina working tube was used for containment. The alumina tube was sealed with steel plates at both ends. In each steel plate was a gas line which served as an inlet/outlet for the purging gas. Argon was used to purge the set-up throughout the experiment to prevent the oxidation of the specimen.

Operating temperatures were 1200°C, 1350°C, and 1500°C, based on typical operating temperatures in PGM smelters. The holding time at a particular temperature was 1 hour; the aim of this was to study the interaction at the point of contact, because operating at longer contact times would introduce other factors such as loss of volatiles. The experiments were repeated twice at each temperature to determine the reproducibility of results. The FeS/Al₂O₃ and the FeS/SiO₂ specimens were placed simultaneously inside the furnace to minimize variability and error in the results. After each reaction, the specimens were cooled under an argon atmosphere and were then removed from the furnace. The images of the pellet post exposure were captured by a camera for optical analysis, and are reported under the results section.

Each pellet was cut longitudinally to produce two samples; one sample was pulverized in preparation for XRD analysis, while the remaining half was mounted for SEM analysis. The XRD patterns, BSE images, and EDS analyses of the reaction products are presented in the next section. Before exposure, the reactants were analysed by SEM-EDS and XRD to determine the composition of the starting materials and the level of impurities. XRD detects only crystalline phases, but the SEM would be able to detect all the possible phases.

Results

The EDS analysis of the as-received powders is presented in Table I. The chemical phases were estimated using atomic ratios. The chemical compositions of the alumina and the silica were close to the targeted reactants, and no impurities were detected in the oxide reactants. The chemical composition of the iron sulphide matched that of FeS₂. The target sulphide was Fe_(1-x)S, which is the constituent of PGM matte, and the XRD-pattern of the as-received iron sulphide powder is shown in Figure 3. As detected by the EDS, pyrite (FeS₂) was the only phase identified by XRD in the iron sulphide powder. The Fe-S phase diagram is depicted in Figure 4, with the data presented for a total pressure of 1 bar and temperatures above 400°. CFeS₂ converts to Fe_(1-x)S and sulphur at 743°C (Walder and Pelton, 2005, Tesfaye and Taskinen, 2010); at constant pressure sulphur is vaporized (Walder and Pelton, 2005). In the current work, the operating temperature was from 1200°C to 1500°C; at these

temperatures the FeS₂ would have converted to Fe_(1-x)S according the phase diagram. The FeS₂ was used as received, and the assumption was made that FeS₂ would convert to Fe_(1-x)S before the operating temperature is reached. The effects of starting with FeS₂ were assumed to be negligible.

The XRD patterns of the as-received alumina and silica powders are shown in Figure 5. The detected phases confirmed the SEM-EDS analysis in Table I. The alumina pattern depicted was that of corundum (Al₂O₃). SiO₂ has a number of polymorphs which have different crystallinity, and the XRD pattern fitted that of cristobalite which is slightly different from that of quartz. No impurities were detected in either the alumina and the silica.

Table I

SEM-EDS analysis of as-received Al₂O₃, FeS, and SiO₂ powders (weight %)

Element	Al ₂ O ₃	Fe _(1-x) S	SiO ₂
O	50.9	–	57.5
Al	48.5	–	–
Fe	0.6	46.4	–
S	–	53.6	–
Si	–	–	42.5

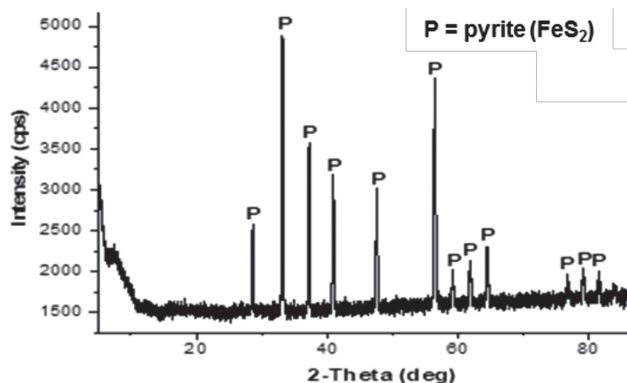


Figure 3—XRD pattern of as-received iron sulphide powder

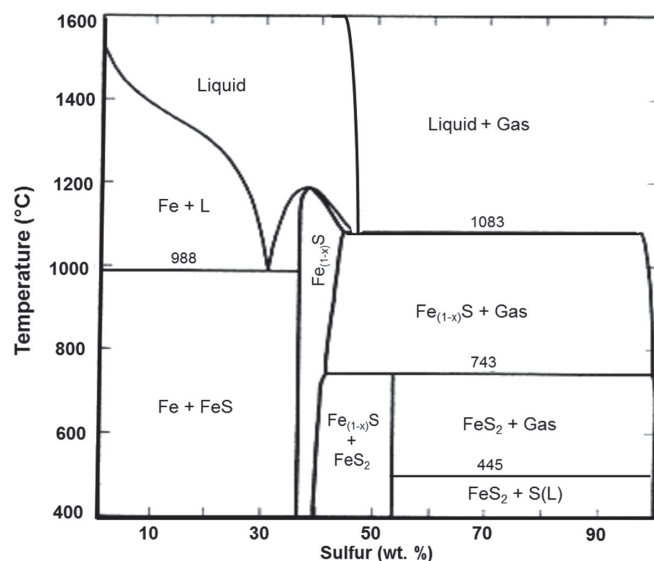


Figure 4—Calculated, optimized Fe-S phase diagram at a total pressure of 1 bar, for temperatures above 400°C (Walder and Pelton, 2005)

On the interactions of iron sulphide with alumina and silica

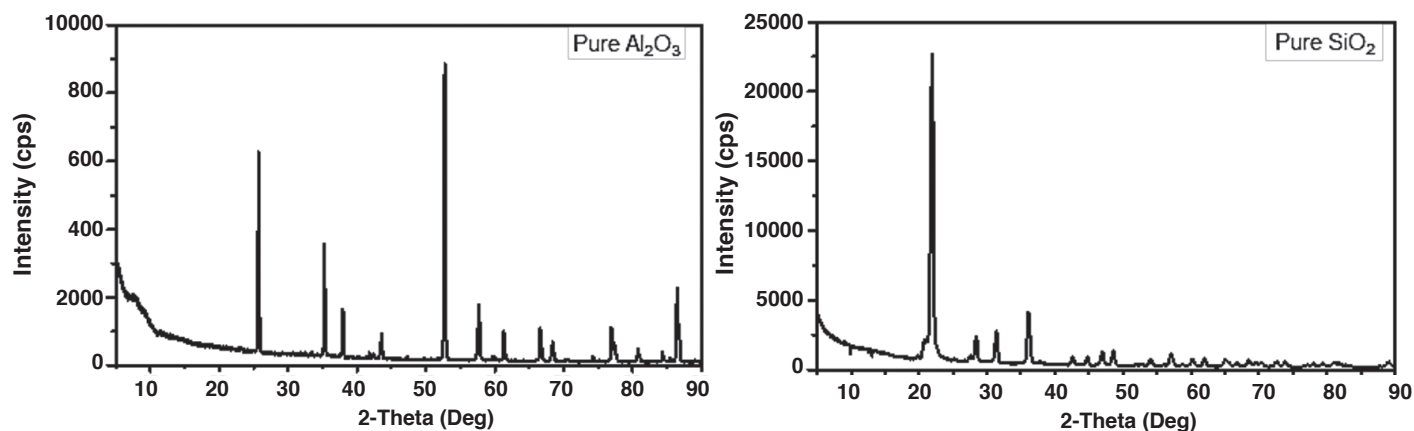


Figure 5—XRD patterns of as-received alumina and silica

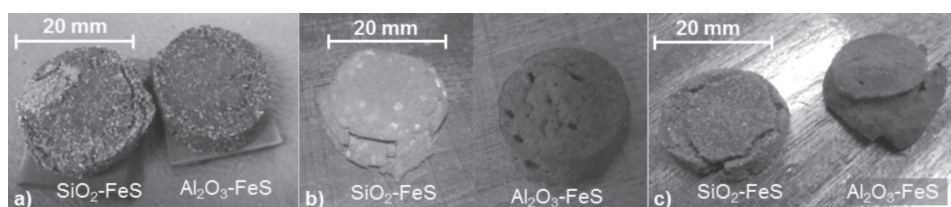


Figure 6—Images of the pellets after exposure at (a) 1200°C, (b) 1350°C, (c) 1500°C

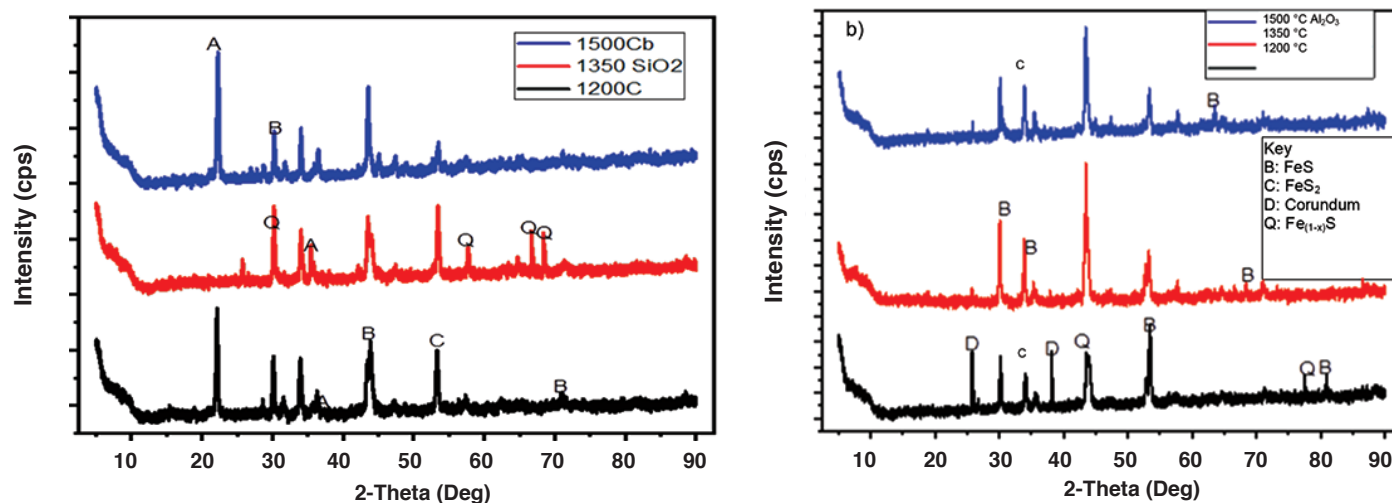


Figure 7—XRD patterns with identified peaks for (a) FeS/SiO₂ specimen and (b) FeS/Al₂O₃ specimen

Figures 6a, 6b, and 6c are images of the specimens after exposure at 1200°C, 1350°C, and 1500°C respectively. At 1200°C (Figure 6a), the SiO₂ pellet developed minor cracks, while the Al₂O₃ pellet did not show significant changes. At 1350°C (Figure 6b), the cracks on the SiO₂ pellet were more noticeable, and the colour of the pellet became light grey with whitish spots. The Al₂O₃ pellet developed pores, and a slight increase in volume was observed.

At 1500°C (Figure 6c) the cracks on the SiO₂ pellet enlarged. The diameter of the pellet increased by 0.2 mm, the colour became darker than at 1350°C, and the whitish spots were not as prominent as at 1350°C. The Al₂O₃ pellet deformed completely and the pores diminished after exposure at 1500°C.

The XRD patterns of the FeS/SiO₂ and the FeS/Al₂O₃ specimens for all temperatures are displayed in Figures 7a and

7b respectively. The patterns are arranged hierarchically; the bottom, middle, and top patterns are for the specimens at 1200°C, 1350°C, and 1500°C respectively. The identified phases are annotated on the graphs.

The FeS/SiO₂ products contained cristobalite (SiO₂) and iron sulphide phases (FeS, Fe_(1-x)S, and FeS₂). An interesting observation was the absence of the cristobalite peak at 1350°C; the other phases were detected at all the temperatures.

The FeS/Al₂O₃ products contained corundum (Al₂O₃) and iron sulphide phases (FeS, Fe_(1-x)S, and FeS₂). The corundum peak is notably absent at 1350°C and 1500°C; however, the sulphide phases were present at all temperatures.

The SEM-BSE images of the FeS/SiO₂ pellet are depicted in Figures 8a, 8b, and 8c for the specimens exposed at 1200°C, 1350°C, and 1500°C respectively. The SEM EDS analyses of the

On the interactions of iron sulphide with alumina and silica

phases annotated 1 to 9 in Figure 8 are presented in Table II. At 1200°C, two phases were identified, a nonstoichiometric SiO₂ and an iron sulphide mixture (Fe_(1-x)S/FeS₂). New products were not detected at 1200°C and it seemed that the SiO₂ had not melted at this temperature. However, cracks were observed in the SiO₂ grains.

At 1350°C, a new phase was observed, which is annotated 5 in Figure 8b. The chemical composition of the new phase was SiO₄; this was estimated using the weight percentages reported in Table II. The SiO₂ and the Fe_(1-x)S/FeS₂ mixture were still present at 1350°C; however, a slight penetration of the iron sulphide into the SiO₂ grain was observed. At 1500°C the penetration of iron sulphide through SiO₂ was more apparent, and the SiO₂ also contains more pronounced cracks. The SiO₄ phase that was observed at 1350°C was still present at 1500°C, and is annotated 6 in Figure 8c. A minor phase, annotated 7, consisted of sulphur-enriched SiO₂. The FeS/FeO mixture was detected (Figure 8c, annotated number 8), while the residual silica was oxygen-enriched, giving a chemical composition of SiO₄ (numbered 9 in Figure 8c). The nonstoichiometry of the oxide phases cast doubt on the accuracy of the EDS analysis, but the analysis gave an indication on the extent of the reaction. The BSE images illustrated the interaction between the oxide and the sulphide, and the presence of intermediate phases was apparent.

Figure 9 depicts the FeS/Al₂O₃ BSE images, and the products after exposure at 1200°C, 1350°C, and 1500°C are depicted in Figures 9a, 9b, and 9c respectively. The EDS analyses of the annotated phases are presented in Table III. At 1200°C, no significant interaction was observed and the phases detected were Al₂O₃ and the Fe_(1-x)S/FeS₂ mixture. At 1350°C, two new phases were detected, namely a nonstoichiometric Al₂O₃ and the FeS/FeO mixture, numbered 3 and 6 in Figure 9b respectively. The Al₂O₃

contained excess oxygen, but no sulphur or iron.

At 1500°C, two new phases were observed, a sulphur-deficient Fe_(1-x)S and an oxygen-enriched Al₂O₃ with up to 6 weight % of sulphur; these are phases 7 and 9 in Figure 9c respectively. Penetration of FeS into the Al₂O₃ was not observed at all temperatures.

Discussion

The effect of temperature on the interactions between FeS and the refractory oxides, SiO₂, and Al₂O₃ was comparable. At 1200°C no new phases were detected, but the FeS/SiO₂ was more prone to cracking than the FeS/Al₂O₃. The phases detected by XRD and SEM-EDS concur. For example, at 1350°C and 1500°C EDS detected nonstoichiometric Al₂O₃ and SiO₂ with excess oxygen, while XRD did not detect the oxide peaks at 1350°C. At 1500°C, SiO₂ was detected, but the Al₂O₃ peak was still not detectable. An oxysulphide (FeS/FeO mixture) was detected at 1350°C for the FeS/Al₂O₃ specimen and at 1500°C for the FeS/SiO₂. A sulphur-deficient iron sulphide (Fe_(1-x)S/Fe mixture) was detected in the FeS/SiO₂ specimen at 1500°C.

As shown in the Fe-S phase diagram (Figure 4), sulphur melts at 444.6°C, while above 450°C sulphur is a gas at a pressure of 1 bar (Walder and Pelton, 2005). In the current work, a sulphur-deficient Fe-S was observed in the FeS/SiO₂ specimen at 1500°C (phase 7 in Figure 9c). This phase could be formed due to vaporization of sulphur at high temperatures. If sulphur is vaporized it would be removed with the off-gas. Upon cooling, the composition of the condensed phases shifted towards the metal-rich end of the Fe-S system in the Fe_(1-x)S/Fe phase field.

Fe_(1-x)S is a solid solution, and the Fe content in Fe_(1-x)S can vary from 50 atom % to 46.7 atom %. A slight change in the Fe:S ratio results in variations in structural, chemical, and other

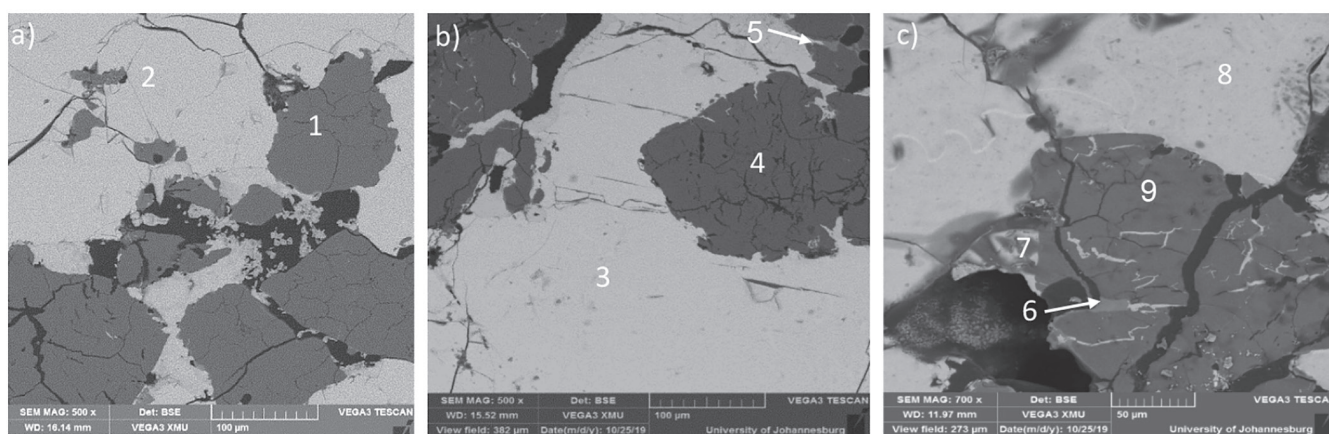


Figure 8—BSE images of the FeS/SiO₂ pellet after exposure at (a) 1200°C, (b) 1350°C, and (c) 1500°C (refer to the EDS analyses of the annotated phases in Table II)

Table II

EDS analysis of the FeS/SiO₂ couple after exposure at 1200°C, 1350°C, and 1500°C (refer to the BSE images in Figure 8) (weight %)

Element	1	2	3	4	5	6	7	8	9
O	62.4	—	—	55.4	70.3	76.4	66.1	11.7	69.2
Fe	0.2	45.3	40.3	2.3	—	0.9	2.4	31	0.1
S	—	54.7	59.7	2.9	—	0.4	12.4	57.3	—
Si	37.4	—	—	39.4	29.7	22.3	19.1	—	30.7
Phase composition	SiO ₃	Fe _(1-x) S+ FeS ₂	Fe _(1-x) S+ FeS ₂	SiO ₂	SiO ₄	SiO ₄	SiS-O	FeS+FeO	SiO ₄

On the interactions of iron sulphide with alumina and silica

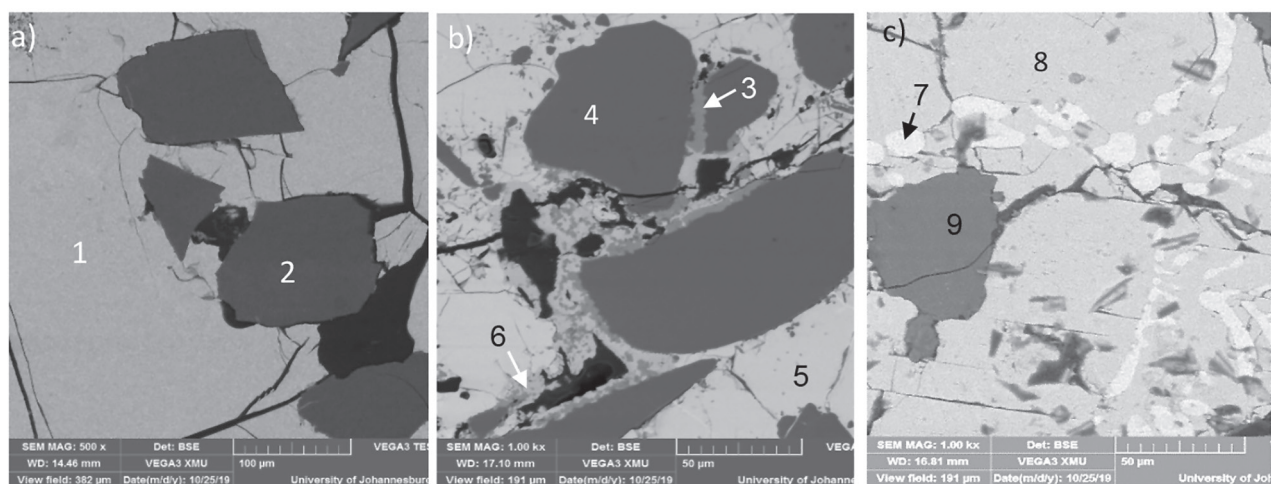


Figure 9—BSE images of the Al_2O_3 pellet after exposure at (a) 1200°C, (b) 1350°C, and (c) 1500°C. The EDS analyses of the annotated phases are in Table III

Element	1	2	3	4	5	6	7	8	9
O -	50.9	67.5	53.1	-	35.5	-	-	74	-
Al -	48.5	32.5	43.6	-	-	-	-	19.7	-
Fe 55.3	0.6	-	0.2	44.8	55.3	77.5	49	-	-
S 44.7	-	-	3.1	55.2	9.2	22.6	51	6.3	-
Phase composition	$\text{Fe}_{(1-x)}\text{S} + \text{FeS}_2$	Al_2O_3	Al_2O_3	Al_2O_3	$\text{Fe}_{(1-x)}\text{S} + \text{FeS}_2$	$\text{FeS} + \text{FeO}$	$\text{Fe}_{(1-x)}\text{S} + \text{Fe}$	$\text{Fe}_{(1-x)}\text{S} + \text{FeS}_2$	Al_2O_3

physical properties of $\text{Fe}_{(1-x)}\text{S}$. The polymorphs are FeS (troilite) and $\text{Fe}_{(1-x)}\text{S}$ (pyrrhotite). Pyrrhotite is Fe-deficient and is stable at various Fe to S ratios; Fe_8S_9 , Fe_9S_{10} , $\text{Fe}_{10}\text{S}_{11}$, and $\text{Fe}_{11}\text{S}_{12}$ (Li, 1997; Roberts *et al.*, 2018). These polymorphs present different diffraction patterns because the temperature of formation and the cooling/heating rate determine the final diffraction pattern (Roberts *et al.*, 2018). The FeS phase relations display extensive solid solution and several polymorphs, as discussed above. These attributes posed a challenge in explaining nonstoichiometric phases.

Al_2O_3 and SiO_2 are the only condensed oxide phases of Al and Si respectively (Haiste, 1978). This implies that the analyses of the nonstoichiometric oxide phases reported at 1350°C and 1500°C are not accurate. To improve these analyses a technique such as the electron microprobe might be more suited for determining the accurate stoichiometry of oxygen in the oxide phases.

Tridymite and cristobalite are polymorphs of SiO_2 ; tridymite is stable between 867°C and 1470°C, while cristobalite is stable from 1470°C to the melting temperature. The volatile species in the Si-O system include Si(g) , $\text{Si}_2\text{(g)}$, $\text{Si}_3\text{(g)}$, SiO(g) , and $\text{SiO}_2\text{(g)}$ (Haiste 1978).

In the Si-O-S system, the condensed phases are SiS (s,l) and SiS_2 (s,l); these sulphides melt at 1090°C, while solid SiS_2 forms in high-sulphur environments. SiS and SiS_2 are volatile, and this can lead to depletion of silicon in a system (Haiste, 1978). SiS_2 has been detected in a gas condensate after exposure of a typical PGM matte to a graphite crucible at temperatures up to 1450°C. Such SiS_2 formation was a result of sulphides interacting with oxide inclusions in matte, although the mechanism of formation was not investigated (Thethway and Cromarty, 2015).

In the FeO-FeS- SiO_2 system, the FeS can react with SiO_2 according to Equation [1] (Jo, Lee, and Kang, 2013). FeS can be oxidized to FeO and sulphur gas according to Equation [2] (Chen *et al.*, 2020).



The products in the FeS/ SiO_2 specimen comprised an FeS/FeO mixture and a phase with Si-O-S (phases 7 and 8 in Figure 8c). The formation of these phases can be explained by the reactions in Equations [1] and [2]. From the discussion above, it is apparent that SiS_2 melts at 1090°C and is highly volatile, therefore any SiS_2 formed would vaporize, leading to losses of Si and S in the residual melt. The vaporization of SiS_2 would also result in the formation of a nonstoichiometric oxide with excess oxygen, as observed at 1350°C and 1500°C. The off-gas stream was not analysed in the current work, but the vaporization of Si and S is a plausible mechanism that can lead to the loss of Si and S, resulting in sulphur-deficient residual sulphides.

An oxidized silicon sulphide has been reported by Li *et al.* (2019). SiS can accommodate from 0.1 to 1 atoms of oxygen in its structure (Li *et al.*, 2019). The formation of the SiS-O phase (phase 7 in Figure 8c) can thus be attributed to the dissolution of oxygen within the SiS (Li *et al.*, 2019).

FeS and FeO form a complete solid solution according to the phase diagram in Figure 10 (McLennan *et al.*, 2000). If the FeO formed according to Equations [1] and [2], it would dissolve in the FeS, thus forming a solid solution.

In the Al-O-S system, the condensed phases are Al_2O_3 , AlS, and Al_2S_3 . Al_2S_3 is the most stable sulphide at room temperature,

On the interactions of iron sulphide with alumina and silica

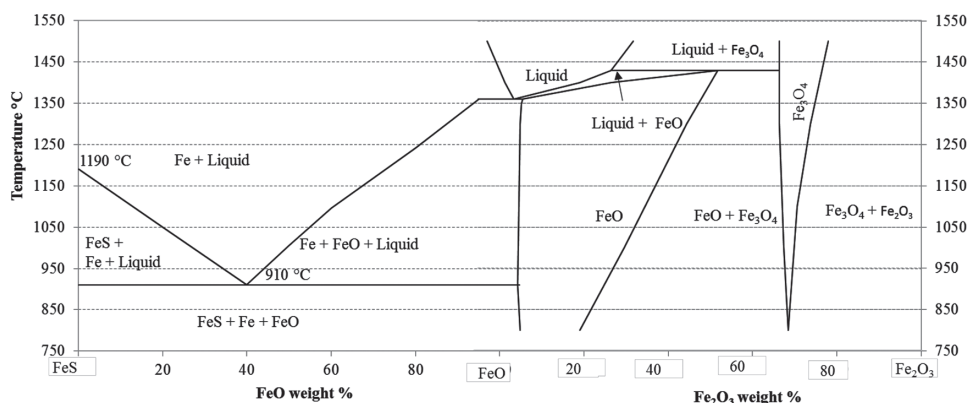


Figure 10—FeS-FeO-Fe₂O₃ equilibrium phase diagram vs. temperature (McLennan et al., 2000)

while AlS melts at 1197°C, and Al₂S₃ melts at 1097°C. The volatile species include Al, AlS, Al₂S, and Al₂S₂ (Haiste 1978). According to Huda et al. (2013), Al₂S₃ can form by the reaction of Al₂O₃ with any sulphur source in the presence of a reductant. Upon heating, Al₂S₃ can be converted to AlS and sulphur (Huda et al., 2016). Although the graphite crucible was used to house the specimen, an alumina plate was used to separate the specimen from the graphite. The prevailing environment inside the specimen was assumed to be slightly oxidizing, considering the formation of an oxysulphide. The mechanism responsible for the formation of the oxysulphide and the nonstoichiometric Al₂O₃ remains a mystery. Future work will focus on studying this system in depth using more controlled environments. The sulphur-deficient FeS could form as per the reaction in Equation [2].

Conclusions

The postulation was tested that refractory brick components may individually be reactive towards matte species. Temperature was found to have a significant effect on the reactivity between FeS and the tested oxides. At 1200°C there was no evidence of interaction apart from minor cracks in the FeS/SiO₂ specimen. At 1350°C an intermediate phase was observed at the boundary of the oxide grain, and penetration of FeS into SiO₂ was enhanced. The penetration of FeS through SiO₂ was noticeably more prominent at 1500°C, with the formation of oxidized SiS and an iron oxysulphide. Al₂O₃ was less reactive than SiO₂, and the detection of nonstoichiometric oxides and the scarcity of data on the FeS-Al₂O₃ system made it a challenge to study the mechanism of FeS/Al₂O₃ interaction. It is therefore concluded that, for the tested conditions, the oxide components of a refractory brick can react with the components of the matte such as FeS

References

- CHEN, M., AVARMAA, K., KLEMETTINEN, L., SHI, J., TASKINEN, P., and JOKILAAKSO, A. 2020. Experimental study on the phase equilibrium of copper matte and silica-saturated FeO_x SiO₂ based slags in pyrometallurgical WEEE processing. *Metallurgical and Materials Transactions B*. <https://doi.org/10.1007/s11663-020-01874-0>
- DU TOIT, J., CROMARTY, R.D., and GARBERS-CRAIG, A.M. 2016. Matte-tap-hole clay refractory brick interaction in a PGM smelter. *Journal of the Southern African Institute of Mining and Metallurgy*, vol. 116, no. 4. pp. 339–342.
- EKSTEEN, J. 2011. A mechanistic model to predict matte temperatures during the smelting of UG2 rich blends of platinum group metal concentrates. *Minerals Engineering*, vol. 24. pp. 676–687.

- HASTIE, J.W. 1978. Characterization of high temperature vapors and gases: *Proceedings of the 10th Materials Research Symposium*, National Bureau of Standards, Gaithersburg, MD, 18–22 September 1978, 1. pp. 1642–1655.
- HUDA, N., RHAMDHANI, M.A., BROOKS, G.A., MONAGHAN, B.J., and PRENTICE, L. 2016. Production of aluminum sulfide through carbo-sulfidation utilising H₂S. *Proceedings of Light Metals 2013*. Sadler, B. (ed.). Springer. pp. 1299–1304. <https://doi.org/10.1007>
- HUNDERMARK, R., MNCWANGO, S., DE VILLIERS, L., and NELSON, L. 2011. The smelting operations of Anglo American's platinum business: an update. *Proceedings of Southern African Pyrometallurgy*, Cradle of Humankind, South Africa, 6–9 March 2011. Jones, R. and den Hoed, P. (eds.). Southern African Institute of Mining and Metallurgy, Johannesburg. pp. 295–308.
- JO, Y., LEE, H.G., and KANG, Y.B. 2013. Thermodynamics of the MnO-FeO-MnS-FeS-SiO₂ system at SiO₂ saturation under reducing condition: Immiscibility in the liquid phase. *Iron and Steel Institute of Japan International*, vol. 53, no. 5. pp. 751–760.
- LI, F. 1997. Studies of structures and phase transitions in pyrrhotite (No. IS-T-1774). PhD dissertation, Ames Laboratory, Iowa State University. pp. 2.
- LI, Z., SONG, S., DONG, S., and GUAN, J. 2019. Oxidized silicon sulfide: stability and electronic properties of a novel two-dimensional material. *Journal of Physical Chemistry C*, vol. 123, no. 49. pp. 29986–29993.
- MCLENNAN, A.R., BRYANT, G.W., BAILEY, C.W., STANMORE, B.R., and WALL, T.F. 2000. Index for iron based slagging for pulverized coal firing in oxidizing and reducing conditions. *Energy and Fuels*, vol. 14. pp. 349–354.
- RAMAKOBYA, T., THETHWAYO, B.M., and MULABA-BAFUBIANDI, A.F. 2019. The interaction of refractory oxide with matte. *Proceedings of the 17th International Conference on Science, Engineering, Technology & Waste Management (SETWM-19)*, Johannesburg, South Africa, 18–19 November 2019. North West University, Potchefstroom, South Africa. pp. 15–17.
- ROBERTS, D.M., LANDIN, A.R., RITTER, T.G., EAVES, J.D., and STOLDT, C.R. 2018. Nanocrystalline iron monosulfides near stoichiometry. *Scientific Reports*, vol. 8, no. 1. pp. 1–10.
- TESFAYE, F. and TASKINEN, P. 2010. Sulfide Mineralogy-Literature Review. Aalto University Publications in Materials Science and Engineering, Espoo, Finland. TKK-MT-214, pp. 26–28.
- THETHWAYO, B.M. and GARBERS-CRAIG, A.M. 2014. Wear of graphite and micropore carbon by synthetic PGM matte. *Proceedings of the Unified International Technical Conference on Refractories (UNITECR 2013)*. Goski, D.G. and Smith, J.D. (eds.). Wiley. pp. 1067–1074.
- THETHWAYO, B.M. and CROMARTY, R.D. 2015. Compatibility of graphite with primary platinum group metals industrial matte. *Materials Research Innovations*, vol. 19 (sup5). pp. S5–948.
- Thethwayo B.M. 2019. Interaction of carbon-based refractories with liquid PGM-furnace melt. PhD thesis, University of Pretoria, South Africa.
- WALDER, P. and PELTON, A.D. 2005. Thermodynamic modeling of the Fe-S system. *Journal of Phase Equilibria and Diffusion*, vol. 26, no. 1. pp. 23–38. ◆

**When your
oxide minerals
gangue up on you**



AXISHOUSE
Reagent Experts

info@axishouse.co.za | www.axishouse.co.za
+27 11 463 4888



Practical considerations in the modelling of resin-grouted rockbolts

P. Tomasone¹, N. Bahrani², and J. Hadjigeorgiou³

Affiliation:

¹ Mining Plus, Toronto, ON, Canada.

² Department of Civil and Resource Engineering, Dalhousie University, Halifax, NS, Canada.

³ Lassonde Institute of Mining, University of Toronto, ON, Canada.

Correspondence to:

J. Hadjigeorgiou

Email:

john.hadjigeorgiou@utoronto.ca

Dates:

Received: 14 Nov. 2019

Revised: 17 Apr. 2020

Accepted: 21 May 2020

Published: June 2020

How to cite:

Tomasone, P., Bahrani, N., and Hadjigeorgiou, J.

Practical considerations in the modelling of resin-grouted rockboltst.

The Southern African Institute of Mining and Metallurgy

DOI ID:

<http://dx.doi.org/10.17159/2411-9717/1010/2020>

ORCID ID:

P. Tomasone
<https://orcid.org/0000-0003-0900-4430>

N. Bahrani
<https://orcid.org/0000-0001-6479-9577>

J. Hadjigeorgiou
<https://orcid.org/0000-0002-6047-3964>

Synopsis

Numerical models are widely used to demonstrate the effect of ground support in stabilizing underground excavations in rock. However, limited attention has been paid to the reliability of the employed models. This is surprising given that these models are often used to make important decisions on the selection or modification of ground support. This paper focuses on the simulation of resin-grouted rebar rockbolts to illustrate the sensitivity of numerical models to the stiffness of reinforcement elements. This was illustrated by employing *in-situ* pull test data from underground hard-rock mines. The numerical investigation demonstrated the implications for the performance of reinforcement as a function of input parameters based on pull tests undertaken in a range of ground conditions.

Keywords

rock reinforcement; pull tests; numerical modelling; distinct element.

Introduction

Rockbolts are the primary means of reinforcing rock masses in underground hard-rock mines using beam building, supporting incompetent strata, creation of a pressure arch, or by direct support of loose blocks (Hadjigeorgiou and Charette, 2001). Rockbolts can be either passive, with the bolt reacting to new loads to impede movement when stretched (Bobet and Einstein, 2010), or actively tensioned when installed. They can be broadly classified by anchoring mechanism as continuously mechanically coupled, continuously frictionally coupled, or discontinuously mechanically or frictionally coupled (Thompson, Villaescusa, and Windsor, 2012). Continuously mechanically coupled bolts include resin-grouted rebar (the focus of this paper), where a rebar tendon is in continuous intimate contact with the borehole using resin grout as a medium. Continuously frictionally coupled bolts include expandable bolts, where a thin-walled folded tube of steel is inflated in a borehole to expand and maintain a frictional coupling throughout the length of the borehole. Discretely mechanically or frictionally coupled bolts include mechanical bolts or a special case of other bolts, where the coupling mechanism has been restricted to a portion of the bolt length (*e.g.* only the toe of the hole is grouted for a rebar bolt).

The most popular reinforcement unit in Canadian underground mines is probably the resin-grouted rebar bolt. This type of reinforcement offers the ability to resist a high tensile load for a moderate cost with excellent corrosion resistance (Hadjigeorgiou and Charette, 2001). Installation is relatively straightforward and already familiar to the majority of the workforce. Furthermore, the use of variable resin setting times with the same bolt allows for a pre-tensioned bolt to be installed relatively quickly while offering full support. Gustafson *et al.* (2016) have demonstrated that resin-grouted bolts have considerable productivity advantages over concrete-grouted bolts.

The use of numerical models is increasingly popular as a tool to investigate the influence of ground support on the stability of excavations. Continuum, discontinuum, and hybrid continuum-discontinuum codes have all been used for these purposes. In theory, the choice of a particular numerical code is based on the type of the problem and the capacity of the code to represent the boundary conditions, and adequately capture the material behaviour and the pertinent failure mechanisms (Bahrani and Hadjigeorgiou, 2017). In practice, other factors such as user's familiarity with particular software, data availability and variability, perceived need for complexity, and computational constraints often drive the numerical modelling process.

There are no clear guidelines for identifying the dominant mode of failure around underground excavations in rock, although it is common to differentiate between weak and soft rocks, and brittle

Practical considerations in the modelling of resin-grouted rockbolts

and hard rocks. Lorig and Varona (2013) suggest that continuum methods are best applied to weak rock characterized by weak rock shear failure, while discontinuum methods are more appropriate for structurally controlled instability. Both continuum and discontinuum methods have been used with some success for brittle rock failure. They recognize, however, that our ability to rigorously analyse all potential failure modes by numerical models is currently limited.

Beyond the numerical modelling limitations, there are two further challenges in constructing representative models. The first is related to understanding the selection of rock mass and stress properties. This has been covered extensively elsewhere, *e.g.* Wiles (2006), Hadjigeorgiou (2012), Lorig and Varona (2013), and Joughin (2017). The second issue, which has received less attention, deals with selecting input data for ground support.

Although the investigations of influence of ground support on the stability of excavations are becoming routine, this is not matched by efforts to understand the significance of ground support input data. In particular, the selected ground support data is illustrated in this paper by focusing on a relatively simple loading mechanism: pull-out testing of a rock reinforcement element. This paper employs numerical models to investigate the behaviour of resin-grouted rebar bolts in a range of ground conditions. It addresses some of the challenges associated with the explicit representation of rock reinforcement elements in stress analysis models. The main focus of the paper is on accounting for the influence of using field data as input parameters for the models. For these purposes, we employed *in-situ* pull test data from underground hard rock mines in Ontario, Canada, as opposed to generic values provided by suppliers. The numerical models captured the load-displacement response and the failure mode of these bolts under axial loading conditions. This work highlights the impact of field data on the simulation of resin-grouted rebar bolts in mine-wide models.

Resin-grouted rebar bolts

Resin-grouted rebar bolts are used widely in underground hard-rock mines. The main difference between these and cement-grouted rebar bolts is the use of a cartridge polyester resin product as a bonding agent. Ideally, the resin forms a continuous column along the bolt length and therefore this bolt type is classified as a continuously mechanically coupled bolt (Thompson, Villaescusa, and Windsor, 2012). Failure of the rockbolt system can occur either along the steel rebar through yielding and eventual rupture, or in the grout medium leading to a pull-out type failure. Compared to cement-grouted rock bolts, the use of a polyester resin for the grout medium typically results in a stiffer bolt response and a higher pull-out capacity. Therefore, the resin-grouted rebar bolt is considered as a stiff reinforcement unit, which resists limited yield before rupture. While both resin- and cement-grouted rebar bolts are considered as continuously mechanically coupled bolts, the failure of the fully grouted resin rebar bolt in hard rock conditions usually occurs with the rebar dowel, rather than a pull-out type failure of the grout. Representative behaviour of the resin-grouted rebar to pull test conditions along with other types of rock reinforcement – cement-grouted rebar, expandable, mechanically anchored, and friction rock stabilizers (FRS) – can be seen in Figure 1.

Much of the earlier literature on grouted rebar bolts focuses on the cement-grouted rebar, rather than the resin-grouted rebar. Examples include the trilinear model suggested by Benmokrane,

Chennouf, and Mitri (1995) with subsequent investigations by Ren *et al.* (2010), Liu, Huang, and Li (2012), and Ma, Nemcik, and Aziz (2016), which focus on the pull-out failure of the cement grouted rebar. Li, Kristjansson, and Høien (2016) investigated the effects of water content of cement on the critical embedment length of rebar. He, An, and Zhao (2015) used the alternative grouted rebar model proposed by Li and Stillborg (1999) to analytically investigate the cement-grouted rebar under a variety of loading conditions, including pull-out tests.

Pull testing

In-situ pull test

Pull testing is a part of the QC/QA programme of many Ontarian underground mines. Pull tests are also undertaken prior to the introduction of new reinforcement products to verify the validity of axial load capabilities stated by the suppliers and demonstrate that the selected rockbolts can be successfully installed in local conditions. When performed at regular intervals, pull tests can alert mine personnel to changes in rockbolt behaviour or demonstrate continued capacity under changing ground conditions. Figure 2 shows an example of a typical *in-situ* pull test set-up.

Variations are numerous, though a variation of note is that the pull tests for resin-grouted rebar are not typically performed to failure. Testing personnel report a safety concern due to the possibility of the broken rockbolt being ejected at high speed in an enclosed area. A less dramatic concern is the potential for damage to the testing equipment and instrumentation with

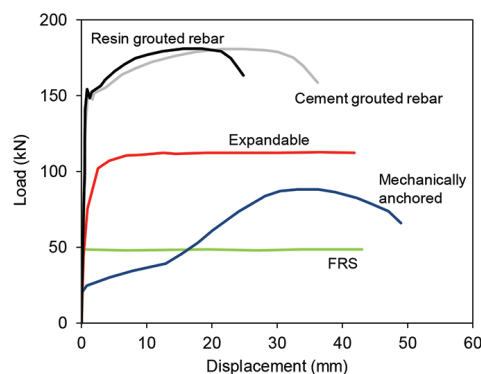


Figure 1—Idealized response of various types of rock reinforcement to axial load (after Li, Stjern, and Myrvang, 2014)



Figure 2—Example of a typical *in-situ* pull test set-up. Note that the rebar protruding from the hydraulic ram is not the rockbolt being tested, but is rather a pull rod connected via an adapter or claw type attachment

Practical considerations in the modelling of resin-grouted rockbolts

relaxation and movement of the loading system. Thus, a complete load-displacement curve with accompanying information about the ground condition of a resin-grouted rebar tested to failure is rarely available. Figure 3a shows the load-displacement curves of five *in-situ* pull tests from two underground mines in which the load was applied until failure. In these tests, the caliper used to measure the displacement was removed well before the bolt rupture and, therefore, the full load-displacement curves were not obtained. The failure load recorded from these tests was between 151 kN and 171 kN, with an average failure load being 165 kN.

Figure 3b shows the load-displacement curves of selected *in-situ* pull tests on 20 mm diameter resin-grouted rebar bolts in 'good', 'fair', and 'poor' quality rock masses (according to the Q-values provided by the mines). These tests were not carried out to the failure of the bolt, with the test performed in good quality rock not reaching the yield load. As can be seen in Figure 3b, the bolts' load-displacement responses are highly linear during the initial loading stages. The rebar bolt in 'good' ground demonstrates a much stiffer behavior than those in 'fair' and 'poor' grounds. These tests were conducted with representatives of the ground support supply company present in addition to mine personnel.

Laboratory pull test

A better understanding of the behavior of rockbolts under pull load conditions can be obtained using controlled laboratory experiments. Laboratory testing of rebar bolts follows four broad classes: pull, shear, combined pull and shear, and push tests. Laboratory pull tests use a loading frame to pull the bolts installed into blocks or cylinders of cement or rock (Stimpson, 1984; Korzeniowski, Skrzypkowski, and Herezy, 2016). A common approach for combined load tests is to install a rebar

orthogonally across two concrete blocks, which can be loaded with a combination of axial and shear loads (Stillborg, 1993; Stjern, 1995; Chen, 2014), though differing geometries have also been used (Grasselli, 2005). Push tests resemble laboratory pull tests, though the bolts are pushed and typically shorter lengths are used (Li, Kristjansson, and Høien, 2016; Ma, Nemcik, and Aziz, 2014; Cao, Ren, and Cook, 2013).

Unfortunately, the number of well documented *in-situ* pull test results is limited. Most of the available information on the performance of different rockbolt types comes from laboratory tests under simulated discontinuity conditions whereby a load is applied to a bolt embedded in two concrete blocks, *e.g.* Stillborg (1993), Chen (2014). Further complicating the issue is that most laboratory tests dealt with the cement-grouted rebar bolt rather than the resin-grouted rebar bolt. Nevertheless, the Stjern's (1995) data-set offers load-displacement curves of a variety of rockbolts, including resin-grouted rebar bolts, which were axially loaded to failure.

Figure 4a shows the full load-displacement curve from a laboratory pull test on a fully resin-grouted rebar bolt by Stjern (1995). As can be seen, under pull loading condition, the resin-grouted rebar bolt elongates elastically, then yields and hardens until it reaches the peak load. The bolt continues to elongate until rupture occurs. Figure 4b compares the load-displacement curves from a laboratory pull test on resin-grouted rebar bolt by Stjern (1995) and those of the *in-situ* pull test presented earlier. It is evident that the initial stiffness in the laboratory test corresponds with that of the *in-situ* pull test conducted in 'fair' ground, whereas the yield behaviour of the rebar bolt in the laboratory follows that of the *in-situ* pull-out test in 'poor' ground. It should be noted that the peak load obtained from the laboratory test (164 kN) is close to the average peak load obtained from *in-situ*

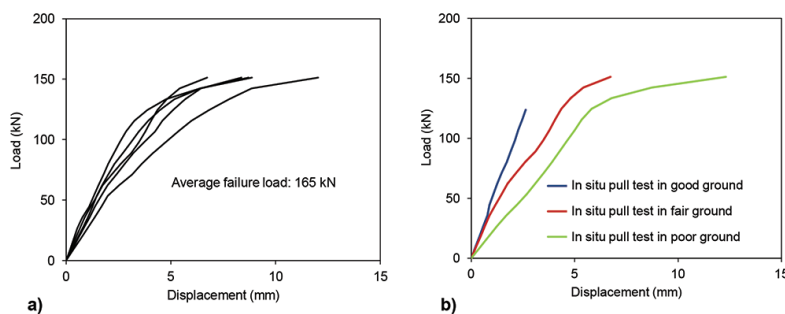


Figure 3—(a) Load-displacement curves of five *in-situ* pull tests on resin-grouted rebar bolts loaded to failure. Note that the calipers to monitor displacement were removed early on (before bolt failure) during the tests and therefore the full load-displacement curves could not be captured. (b) Selected load-displacement curves of resin-grouted rebar bolts from *in-situ* pull tests in 'good', 'fair', and 'poor' quality rock masses

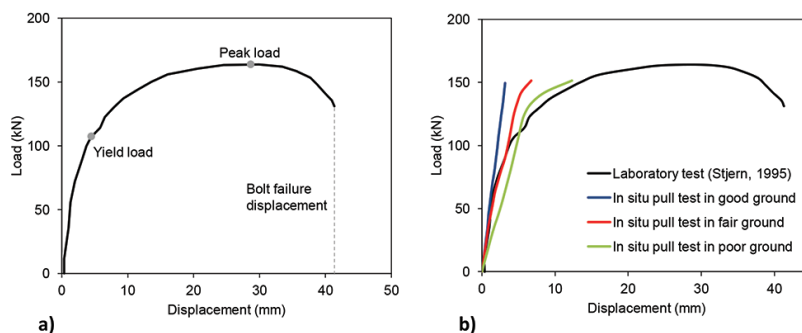


Figure 4—(a) Components of load-displacement curves for resin-grouted rebar bolts pull tested in the laboratory by Stjern (1995), and (b) comparison between the force-displacement curves of *in-situ* pull-out tests on resin-grouted rebar bolts in different ground conditions with that from a laboratory test by Stjern (1995)

Practical considerations in the modelling of resin-grouted rockbolts

tests (165 kN) presented in Figure 3a. Table I compares the results of the laboratory pull test from Stjern (1995), *in-situ* tests for different ground conditions (Figure 3b), and *in-situ* tests conducted until bolt failure (Figure 3a), in terms of the initial stiffness, yield load, peak load, and bolt rupture displacement.

In this article, the results of the laboratory pull test on fully resin-grouted rebar bolt reported by Stjern (1995) and presented in Figure 4, in terms of the peak load and rupture displacement values (Table I), were first used to extrapolate the full load-displacement curves of the *in-situ* pull tests for different ground conditions presented in Figure 3b and Figure 4b. The extrapolated load-displacement curves were then used to simulate *in-situ* pull tests using an explicit reinforcement element and extrapolate the load-displacement response of fully resin grouted rebar bolts in different ground conditions.

Numerical simulation of *in-situ* pull tests

Numerical modeling plays an important role in the stability analysis and design of underground excavations. Continuum, discontinuum, and hybrid continuum-discontinuum codes have been used to simulate surface and underground excavations and various types of rock reinforcement and surface support. The choice of a particular numerical code is based on the type of the problem and the capacity of the code to represent the boundary conditions, adequately capture the material behaviour, and the pertinent failure mechanisms (Bahrani and Hadjigeorgiou, 2017). Other factors such as user's familiarity with particular software, data availability and variability, perceived need for complexity, and computational constraints are also important.

In recent years, various types of rock reinforcement models have been developed and implemented into the numerical codes. Bahrani and Hadjigeorgiou (2017) investigated the applicability of both implicit and explicit rock reinforcement models for simulating laboratory pull and shear tests on cement-grouted rebar bolts. They concluded that although both types of model can be used to represent rock reinforcement, for most practical purposes the explicit rockbolt model provides a more realistic simulation of the failure of both the bolt and the grout under diverse loading conditions.

The focus of this work is on investigating a single loading mechanism (axial load) of a resin rockbolt installed in three different ground conditions. In particular, it illustrates the challenges in the extrapolation of explicit reinforcement models from laboratory to *in-situ* conditions. This was achieved by simulating the *in-situ* pull tests on fully resin-grouted rebar bolts in the three different ground conditions presented in the previous section (Figure 3b).

Choice of modelling software and reinforcement element

The numerical simulation of rock reinforcement can be

accomplished with material models (*e.g.* Ferrero, 1995; Grasselli, 2005; Aziz and Jalalifar, 2007) or by structural elements formulated in the software (*e.g.* Malmgren and Nordlund, 2008; Liu, Huang, and Li, 2012; Gao, Stead, and Kang, 2015; Karampinos, Hadjigeorgiou, and Turcotte, 2016; Karampinos, Hadjigeorgiou, and Pierce, 2018; Bahrani and Hadjigeorgiou, 2018). Both approaches are valid, although the fine mesh size requirements for simulating rock reinforcement via material models are computationally intensive. Consequently, structural elements are the preferred approach for the simulation of large-scale mining problems.

The two-dimensional Universal Distinct Element Code, UDEC, developed by Itasca Consulting Group (Itasca, 2014), was used in this study to simulate the *in-situ* pull test on a fully resin-grouted rebar bolt. UDEC offers three structural elements for simulating rock reinforcement; the 'local' reinforcement element, the 'global' shearing-resistant reinforcement element, and the 'global' bending- and shearing-resistant reinforcement element (Itasca, 2014). The 'local' and 'global' reinforcement elements are examples of implicit and explicit reinforcement models.

The 'local' reinforcement element does not act over intact rock, but only over the discontinuities in the modelled jointed rock mass. In this study, given the lack of information on discontinuities, the pull tests are simulated in an equivalent continuum rock mass, and this precludes the use of the 'local' reinforcement element. The 'global' reinforcement element in UDEC comes in two types: 'cable' and 'rockbolt' elements. The 'cable' element is a shearing-resistant element, which provides very little resistance to bending, while the 'rockbolt' element provides sufficient resistance to both shearing and bending. Both types of 'global' reinforcement elements require input parameters for the dowel (*e.g.* geometry, modulus of elasticity, yield load) as well as parameters for the grout and grout-rock interface (*e.g.* grout strength and stiffness). While both the 'cable' and 'rockbolt' elements can be used to simulate continuously mechanically coupled bolts, the 'rockbolt' element is well-suited to represent rock reinforcement in which the nonlinear effects of confinement, grout or resin bonding, or tensile rupture are important.

Bahrani and Hadjigeorgiou (2017) demonstrated that when the 'cable' element is used to simulate a rebar bolt, its capacity in the laboratory shear test is underestimated. This has implications for ground support design and stability analysis of underground excavations in jointed rock masses. The use of the 'cable' element instead of the 'rockbolt' element may result in an underestimation of the rebar bolt's bending capacity, which may lead to a conservative design of the support system.

Another advantage of the 'rockbolt' element over the 'cable' element, demonstrated by Bahrani and Hadjigeorgiou (2017), is its explicit representation of bolt failure. The 'rockbolt' element

Table I

Summary of *in-situ* and laboratory pull test results on resin-grouted rebar bolts

Parameters	<i>In-situ</i> pull-out tests				Laboratory pull-out test
	Good ground	Fair ground	Poor ground	Loaded until bolt failure (average of 5 tests)	Stjern (1995)
Stiffness (kN/mm)	46.9	28.6	21.4	27.2	18.9
Yield load (kN)	–	125	125	119	123
Peak load (kN)	–	–	–	165	164
Rupture deformation (mm)	–	–	–	–	41

Practical considerations in the modelling of resin-grouted rockbolts

can capture the actual bolt breakage based upon a user-defined tensile failure strain limit. Therefore, the 'rockbolt' element was chosen in this study to simulate the *in-situ* pull test.

Global reinforcement ('rockbolt' element)

As shown in Figure 5, the 'rockbolt' element is divided into a number of segments of length L , with nodal points located at each segment end. The 'rockbolt' element interacts with the surrounding rock medium *via* shear and normal coupling springs, which are connectors that transfer forces and motion between the 'rockbolt' element and the grid-points associated with the block zone, in which the nodes are located (Figure 5).

The 'rockbolt' element segments are treated as a linearly elastic material that may yield in the axial direction either in tension or compression. The tensile and compressive yield strengths are used to define the strength limits. Inelastic bending is simulated in this element by specifying a limiting plastic moment. This means that the 'rockbolt' elements behave elastically until they reach the plastic moment. In addition, segments may break and separate at the nodes, based on a user-defined tensile failure strain limit. A strain measure, called the 'total plastic tensile strain', based on adding the axial and bending plastic strains, is evaluated at each node. If this strain exceeds the tensile failure strain limit, the forces and moment in this segment are set to zero and the 'rockbolt' element is assumed to have failed (Itasca, 2014).

Figure 6 shows the grout parameters in reference to displacement and load for the 'rockbolt' element. Under an

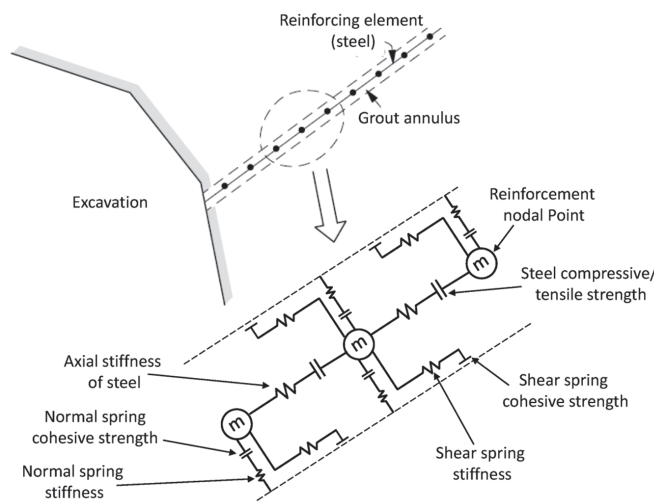


Figure 5—Conceptual mechanical representation of the global reinforcement ('rockbolt' element; after Bahrani and Hadjigeorgiou, 2017)

idealized pull test, as simulated numerically in this study, the loads are axial and therefore parameters regarding resistance to bending are not discussed.

The shear behavior of the interface during relative displacement between the element nodes and the grid-points is described numerically by the coupling spring shear stiffness (CS_{stiff} in Figure 6a) according to the following equation:

$$F_s/L = CS_{stiff} (u_p - u_m) \quad [1]$$

where F_s is the shear force that develops in the shear coupling spring, u_p and u_m are the axial displacement of the 'rockbolt' element and the medium (soil or rock), and L is the segment length. The limiting shear force (F_s^{max}) that can be developed along the 'rockbolt' element/grid-point interface is a function of the cohesive strength of the interface (CS_{coh}) and the stress-dependent frictional resistance (CS_{fric}) along the interface (Figure 6b) according to:

$$F_s^{max}/L = CS_{coh} + \sigma'_c \times \tan(CS_{fric}) \times \text{perimeter} \quad [2]$$

where the perimeter is the exposed perimeter of the rockbolt (*i.e.*, the length of the rockbolt surface that is in contact with the medium), and σ'_c is the mean effective confining stress normal to the 'rockbolt' element. Other parameters required for the simulation of rock reinforcement include the cross-sectional area, second moment of area, density, and elastic modulus of the bolt. Further details of the theoretical aspects of the 'rockbolt' element can be found in the UDEC manual (Itasca, 2014).

Model geometry and specification

The 'rockbolt' element has been successfully employed in the past by Ma, Nemcik, and Aziz (2014), Nemcik *et al.* (2014), and Bahrani and Hadjigeorgiou (2017) to investigate various aspects of rock reinforcement. Ma, Nemcik, and Aziz (2014) used the 'rockbolt' element to simulate resin-grouted rebar bolts in underground coal mine roadways. Nemcik *et al.* (2014) also used this reinforcement element to simulate progressive shear force distribution and debonding of a fully grouted rockbolt subjected to tensile loading. Bahrani and Hadjigeorgiou (2017) used the 'rockbolt' element to simulate laboratory pull and shear tests on cement-grouted rebar bolts reported by Stjern (1995).

Figure 7 shows the geometry and boundary conditions of the UDEC model used by Bahrani and Hadjigeorgiou (2017), along with a comparison between the force-displacement curve from the laboratory pull test reported by Stjern (1995) and that from the calibrated model. As shown in Figure 7a, the UDEC model consisted of two elastic blocks separated by a frictional joint. The pull test was simulated by applying a velocity boundary to the left side of the left block while the sum of reaction forces

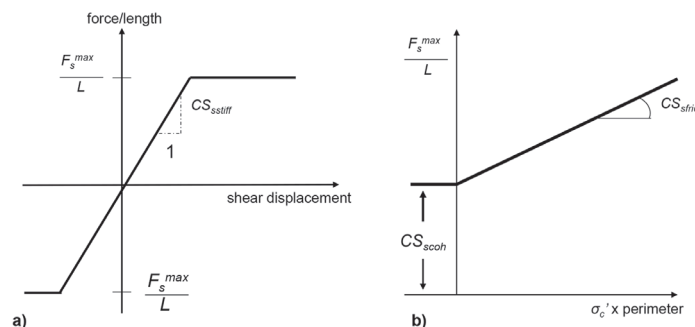


Figure 6—Graphical representation of input parameters associated with grout and the behaviour of the grout-rock interface under pull test loading condition: (a) relationship between shear force and shear displacement, and (b) shear strength criterion for the shear coupling spring of the 'rockbolt' element

Practical considerations in the modelling of resin-grouted rockbolts

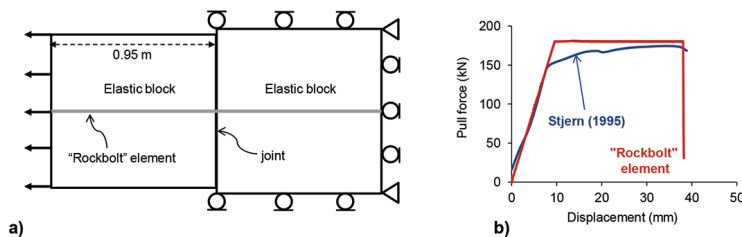


Figure 7—(a) Numerical model of the Stjern's (1995) laboratory pull test on cement-grouted rebar by Bahrani and Hadjigeorgiou (2017); (b) comparison between the results of laboratory test and numerical model of pull test (after Bahrani and Hadjigeorgiou, 2017)

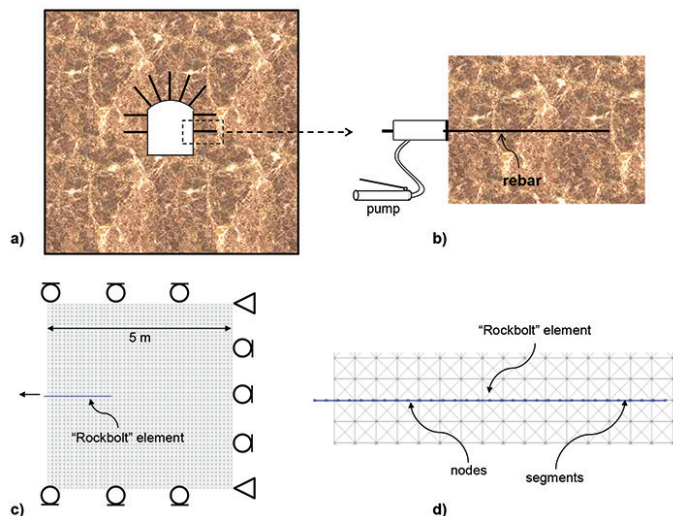


Figure 8—(a) and (b) Schematic of an *in-situ* pull-out test in an underground drift; (c) and (d) numerical model of *in-situ* pull test showing model boundary conditions, mesh size, and the adopted 'rockbolt' element components

developed on the boundaries of the right block was being monitored. The correspondence between the results of laboratory test and numerical simulations presented in Figure 7b suggests that the 'rockbolt' element is a suitable reinforcement model for the simulation of the behaviour of grouted rebar bolts under pull loading conditions.

In practice, *in-situ* pull tests are usually conducted on the sidewalls of mining drifts. Figure 8a and Figure 8b show a schematic of an *in-situ* pull test in a drift. The geometry and the boundary conditions of the UDEC model, including the 'rockbolt' element, are presented in Figure 8c and Figure 8d, respectively. The geometry of the host rock is a 5 m × 5 m elastic block with a 'rockbolt' element protruding 10 cm from the centre of the left boundary. As shown in Figure 8c, the pins and rollers were used for the model corners and sidewalls, respectively, to approximate the *in-situ* condition. The size and shape of the zones (mesh elements) were chosen to align the embedded rockbolt to the mesh elements (Figure 8d).

The pulling action was applied to the last node on the left side of the 'rockbolt' element with a fixed velocity in the negative x-direction, as shown with the arrow in Figure 8c. Forces acting on the rockbolt were recorded directly by summing the internal forces in the x-direction. The summation of reaction forces on the right model boundary was also recorded. A comparison of the two methods acted as a check for errors with the model construction and calculations.

Model calibration and results

For the purpose of this investigation, the model was assigned equivalent continuum rock mass elastic properties, obtained from

the selected pull test reports. During the calibration process, it was noted that the elastic properties of the rock mass have no influence on the load-displacement response of the 'rockbolt' element. Therefore, the rock mass in all the models was assigned an elastic modulus of 40 GPa and a Poisson's ratio of 0.21.

The UDEC model was initially calibrated to the *in-situ* pull test force-displacement curves presented in Figure 4b. As discussed earlier, only the elastic portion of the load-displacement curve of the rebar bolt in the case of the 'good' ground, and the elastic and the initial yielding sections of the load-displacement curve of the rebar bolt in the cases of the 'fair' and 'poor' grounds, were available from the *in-situ* pull test results. Therefore, the model calibration was initially carried out with respect to the elastic stiffness of the force-displacement curve of the *in-situ* pull tests by adjusting the shear coupling spring stiffness of the 'rockbolt' element. Note that the stiffness of the load-displacement curve from an *in-situ* pull test is a function of the bolt-grout contact stiffness, grout stiffness, and the grout-rock mass contact stiffness. Therefore, the value of the shear coupling spring stiffness obtained from the calibration process accounts for all three components.

The calibration was continued by matching the peak load corresponding to the average failure load of the *in-situ* pull tests loaded to failure (presented in Figure 3a) and the rupture displacement obtained from the results of laboratory pull test on resin-grouted rebar bolt reported by Stjern (1995) (shown in Figure 4a and summarized in Table I).

Figure 9a, Figure 9c, and Figure 9e show the load-displacement curves from the *in-situ* pull tests for the three ground conditions (solid lines) and their linear extrapolation

Practical considerations in the modelling of resin-grouted rockbolts

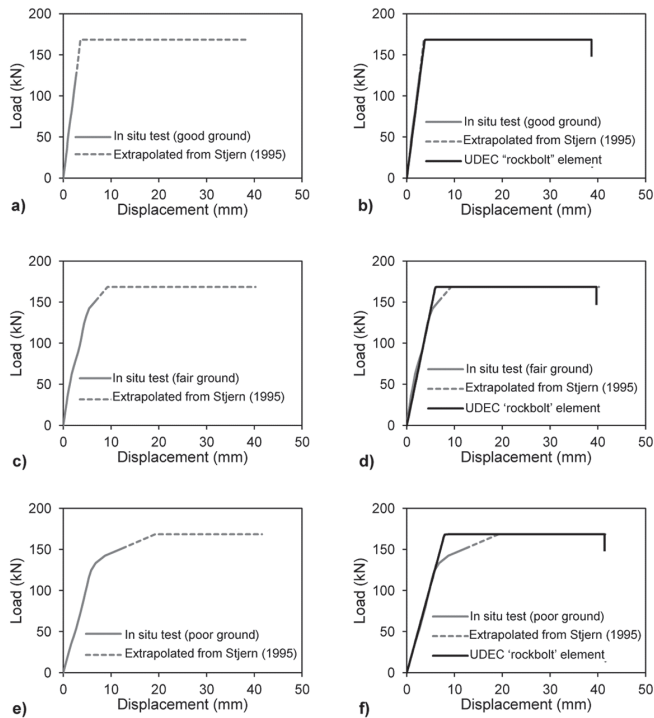


Figure 9—Load-displacement curves of *in-situ* pull test and their extensions to average peak load obtained from an *in-situ* pull test loaded until failure, and rupture displacement obtained from laboratory pull test reported by Stjern (1995) in (a) ‘good’ ground, (c) ‘fair’ ground, and (e) ‘poor’ ground. Corresponding force-displacement curves of the calibrated ‘rockbolt’ element in (b) ‘good’ ground, (d) ‘fair’ ground, and (f) ‘poor’ ground

(dashed lines) to the peak load followed by plastic deformation until bolt rupture at a displacement corresponding to that from the result of laboratory test reported by Stjern (1995). Figure 9b, Figure 9d, and Figure 9f show the force-displacement curves of the calibrated model in comparison with those presented in Figure 9a, Figure 9c, and Figure 9e. In all three cases, the ‘rockbolt’ elements failed at the element node just outside the simulated rock mass, indicating the failure of the steel (Figure 10).

As illustrated in Figures 3 and 4, the load-displacement curves of selected *in-situ* pull tests on 20 mm diameter resin grouted rebar bolts in ‘good’, ‘fair’, and ‘poor’ quality rock show a relatively linear behaviour during the initial loading stages. For the purposes of the numerical models, these were further approximated to an idealized linear behaviour (Figure 9). It is acknowledged that a linear extrapolation of the *in-situ* pull

tests is in effect an approximation. Nevertheless, in light of the relative approximations in all input parameters of the constructed numerical model, this is a reasonable trade-off.

The values of the ‘rockbolt’ element input parameters obtained from the calibration process are listed in Table II. As can be seen from this table, the main difference between the calibration results for the three ground conditions is the value of the shear coupling spring stiffness. In the case of ‘good’ ground, a higher shear coupling spring stiffness value was required to capture the higher initial stiffness of the load-displacement curve compared to those of the ‘fair’ and ‘poor’ grounds.

Further numerical simulations were conducted to investigate the influence of shear coupling spring stiffness ($CSstiff$) on the force-displacement behavior of the ‘rockbolt’ element. For this purpose, two more models were run with different $CSstiff$ -values, as demonstrated in Figure 11.

As can be seen in Figure 11, the slope of the linear section of the force-displacement curve decreases with decreasing value of the shear coupling spring stiffness, the parameter that accounts for the bolt-grout contact stiffness, the grout stiffness, and the grout-rock mass contact stiffness. Assuming that the bolt and grout conditions are constant, it can be concluded that the rock mass quality plays the main role in the behaviour of the force-displacement response of a rebar bolt during *in-situ* pull tests. It is suggested that the results of numerical modeling of *in-situ* pull tests using the ‘rockbolt’ element in terms of their input parameters (presented in Table II and Figure 11) can be used in large-scale continuum elastic models for the simulation of resin-grouted rebar bolts in varying ground conditions.

Conclusions

Although investigations on the influence of ground support on the stability of excavations are increasingly common, they

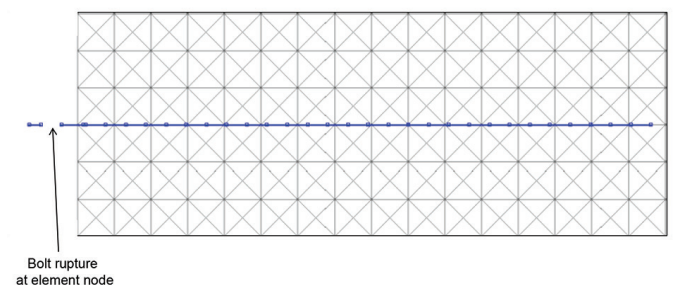


Figure 10—Failure modes of the ‘rockbolt’ element in the simulated *in-situ* pull test

Table II

‘Rockbolt’ input parameters for the calibrated numerical models

Ground condition	‘Good’ ground	‘Fair’ ground	‘Poor’ ground
Bolt cross-sectional area (m ²)	0.00031	0.00031	0.00031
Bolt second moment of area (m ⁴)	7.9×10 ⁻⁹	7.9×10 ⁻⁹	7.9×10 ⁻⁹
Exposed perimeter (m)	0.062	0.062	0.062
Bolt density (kg/m ³)	8×104	8×104	8×104
Bolt elastic modulus (GPa)	200	200	200
Bolt tensile yield strength (kN)	163	163	168.4
Bolt tensile failure strain limit	0.42	0.39	0.38
Plastic moment (kNm)	2	2	2
Shear coupling spring stiffness (GN/m/m)	0.046	0.023	0.016
Shear coupling spring cohesion (kN/m)	2000	2000	2000
Shear coupling spring friction angle (°)	0	0	0
Bolt spacing (m)	1	1	1

Practical considerations in the modelling of resin-grouted rockbolts

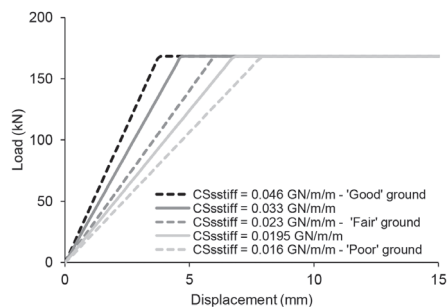


Figure 11—Influence of shear coupling spring stiffness (CSs stiff) on load-displacement curve of 'rockbolt' element

are not matched by efforts to understand the implication of how reinforcement elements are implemented in the numerical models. Another concern is that even when sensitivity studies are employed to identify the implication of recommendations of variation in input data, these are often limited to information on the rock mass condition. The impact of ground support properties, of the same rockbolt type, is often overlooked.

This is illustrated in this paper by focusing on a relatively simple loading mechanism: pull-out testing of a rock reinforcement element. This paper employed numerical models to investigate the behaviour of resin-grouted rebar bolts in a range of ground conditions. It addresses some of the challenges associated with the explicit representation of rock reinforcement elements in stress analysis models. The main focus of the paper is on accounting for the influence of using field and laboratory data as input parameters for the models. For these purposes, we employed *in-situ* pull test data from underground hard-rock mines in Ontario, Canada, as opposed to generic values provided by suppliers. The numerical models captured the load-displacement response and the failure mode of these bolts under axial loading conditions. This work highlights the impact of field data in the simulation of resin-grouted rebar bolts in mine-wide continuum models and has significant implications in the interpretation of the results from numerical modelling.

Acknowledgements

This study was funded by the Ontario Ministry of Labour Research Opportunities Program. The authors acknowledge the participation of the ground control committee of Workplace Safety North Ontario in collecting the field data.

References

- AZIZ, N. and JALALIFAR, H. 2007. Experimental and numerical study of double shearing of bolt under confinement. *Proceedings of the 26th International Conference on Ground Control in Mining*, Peng, S.S., Mark, C., Finfinger, G., Tadolini, S., Khair, A.W., Heasley, K., and Luo, Y. (eds). Morgantown, WV. West Virginia University. pp. 242–249.
- BAHRANI, N. and HADJIGEORGIOU, J. 2018. Influence of stope excavation on drift convergence and support behavior: Insights from 3D continuum and discontinuum models. *Rock Mechanics and Rock Engineering*, vol. 51. pp. 2395–2413.
- BAHRANI, N. and HADJIGEORGIOU, J. 2017. Explicit reinforcement models for fully-grouted rebar rock bolts. *Journal of Rock Mechanics and Geotechnical Engineering*, vol. 9. pp. 267–280.
- BENMOKRANE, B., CHENNOUF, A., and MITRI, H.S. 1995. Laboratory evaluation of cement-based grouts and grouted rock anchors. *International Journal of Rock Mechanics and Mining Sciences & Geomechanics Abstracts*, vol. 32. pp. 633–642.
- BOBET, A. and EINSTEIN, H.H. 2010. Tunnel reinforcement with rockbolts. *Tunnelling and Underground Space Technology*, vol. 26. pp. 100–123.
- CAO, C., REN, T., and COOK, C. 2013. Calculation of the effect of Poisson's ratio in laboratory push and pull testing of resin-encapsulated bolts. *International Journal of Rock Mechanics and Mining Sciences*, vol. 64. pp. 175–180.
- CHEN, Y. 2014. Experimental study and stress analysis of rock bolt anchorage. *Journal of Rock Mechanics and Geotechnical Engineering*, vol. 6. pp. 428–437.

- Ferrero, A.M. 1995. The shear strength of reinforced rock joints. *International Journal of Rock Mechanics and Mining Science & Geomechanics Abstracts*, vol. 32. pp. 595–605.
- GAO, F., STEAD, D., and KANG, H. Numerical simulation of squeezing failure in a coal mine roadway due to mining-induced stresses. *Rock Mechanics and Rock Engineering*, vol. 48. pp. 1635–1645.
- GRASSELLI, G. 2005. 3D behaviour of bolted rock joints: Experimental and numerical study. *International Journal of Rock Mechanics and Mining Sciences*, vol. 42. pp. 15–24.
- GUSTAFSSON, A., SCHUNNASSON, H., TIMUSK, M., and HAUTA, R. 2016. Productivity of rock reinforcement: methodology development. *Journal of the Southern African Institute of Mining and Metallurgy*, vol. 116. pp. 1127–1134.
- HADJIGEORGIOU, J. 2012. Where do the data come from? *Transactions of the Institution of Mining and Metallurgy: Section A: Mining Technology*, vol. 121, no. 4. pp. 36–247.
- HADJIGEORGIOU, J. and TOMASONE, P. 2018. Characterising the behaviour of rock bolts based on *in-situ* pull tests. *Caving 2018 – Proceedings of the Fourth International Symposium on Block and Sublevel Caving*, Vancouver, Canada, 15–17 October 2018. Potvin, Y. and Jakubec, J. (eds.). Australian Centre for Geomechanics. pp. 727–734.
- HADJIGEORGIOU, J. and CHARETTE, F. 2001. Rock bolting for underground excavations. *Underground Mining Methods – Engineering Fundamentals and International Case Studies*. Society of Mining, Metallurgy, and Exploration (SME), Littleton, CO. pp. 547–554.
- HE, L., AN, X.M., and ZHAO, Z.Y. 2015. Fully grouted rock bolts: An analytical investigation. *Rock Mechanics and Rock Engineering*, vol. 48. pp. 1181–1196.
- ITASCA 2014. UDEC – Universal Distinct Element Code, Ver. 6.0. Itasca Consulting Group, Inc., Minneapolis, MN.
- JOUGHIN, W.C. 2017. Dealing with uncertainty and risk in the design of deep and high stress mining excavations. *Deep Mining 2017: Proceedings of the Eighth International Conference on Deep and High Stress Mining*. Wesselo, J. (ed.). Australian Centre for Geomechanics, Perth. pp. 489–507.
- KARAMPINOS, E., HADJIGEORGIOU, J., and PIERCE, M. 2018. Explicit representation of rock reinforcement in 3D DEM models of foliated ground. *Journal of the Southern African Institute of Mining and Metallurgy*, vol. 118. pp. 1243–1250.
- KARAMPINOS, E., HADJIGEORGIOU, J., and TURCOTTE, P. 2016. Discrete element modelling of the influence of reinforcement in structurally controlled squeezing mechanisms in a hard rock mine. *Rock Mechanics and Rock Engineering*, vol. 49. pp. 4869–4892.
- KORZENIOWSKI, W.H., SKRZYPKOWSKI, K., and HEREZY, Ł. 2016. Strain of steel rebar vs. rock bolt elongation on a laboratory stand. *Proceedings of Ground Support 2016*. Luleå, Sweden, 12–14 September. 2016. Nordlund, E., Jones, T., and Eitzenberger, A. (eds). Luleå University of Technology.
- LI, C. and STILLBORG, B. 1999. Analytical models for rock bolts. *International Journal of Rock Mechanics and Mining Sciences*, vol. 36. pp. 1013–1029.
- LI, C., KRISTJANSSON, G., and HØIEN, A.H. 2016. Critical embedment length and bond strength of fully encapsulated rebar rockbolts. *Tunnelling and Underground Space Technology*, vol. 59. pp. 16–23.
- LI, C., STJERN, G., and MYRVANG, A. 2014. A review on the performance of conventional and energy-absorbing rockbolts. *Journal of Rock Mechanics and Geotechnical Engineering*, vol. 6. pp. 315–327.
- LIU, B., HUANG, D., and LI, D.Y. 2012. Analytical formulation on the mechanical behavior of anchorage interface for full-length bonded bolt. *Applied Mechanics and Materials*, vol. 166–169. pp. 3254–3257.
- LORIG, L. and VARONA, P. 2013. Guidelines for numerical modelling of rock support for mines. *Proceedings of the Seventh International Symposium on Ground Support in Mining and Underground Construction*. Brady, B. and Potvin, Y. (eds). Australian Centre for Geomechanics, Perth. pp. 81–106.
- MA, S., NEMCIK, J., and AZIZ, N. 2014. Simulation of fully grouted rockbolts in underground roadways using FLAC2D. *Canadian Geotechnical Journal*, vol. 51. pp. 911–920.
- MA, S., ZHAO, Z., NIE, W., and GUI, Y. 2016. A numerical model of fully grouted bolts considering the tri-linear shear bond-slip model. *Tunnelling and Underground Space Technology*, vol. 54. pp. 73–80.
- MALMGREN, L. and NORDLUND, E. 2008. Interaction of shotcrete with rock and rock bolts – A numerical study. *International Journal of Rock Mechanics and Mining Sciences*, vol. 45. pp. 538–553.
- NEMCIK, J., MA, S., AZIZ, N., REN, T., and GENG, X. 2014. Numerical modelling of failure propagation in fully grouted rock bolts subjected to tensile load. *International Journal of Rock Mechanics and Mining Sciences*, vol. 71. pp. 293–300.
- REN, F.F., YANG, Z.J., CHEN, J.F., and CHEN, W.W. 2010. An analytical analysis of the full-range behaviour of grouted rockbolts based on a tri-linear bond-slip model. *Construction and Building Materials*, vol. 24. pp. 361–370.
- STILLBORG, B. 1993. Rockbolt tensile loading across a joint. *Proceedings of the International Mine Water Association Symposium*, Chililabombwe, Zambia. IMWA, Wendelstein, Germany. pp. 587–604. https://www.imwa.info/docs/imwa_1993/IMWA_1993_Stillborg_587-604.pdf
- STIMPSON, B. 1984. A simple rock bolt pull-out test device for teaching purposes. *International Journal of Rock Mechanics and Mining Science & Geomechanics Abstracts*, vol. 24. pp. 217–218.
- STJERN, G. 1995. Practical performance of rock bolts. PhD thesis, Norwegian University of Science and Technology.
- THOMPSON, A.G., VILLASECUSA, E., and WINDSOR, C.R. 2012. Ground support terminology and classification: An update. *Geotechnical and Geological Engineering*, vol. 30. pp. 553–580.
- WILES, T.D. 2006. Reliability of numerical modelling predictions. *International Journal of Rock Mechanics and Mining Sciences*, vol. 43. pp. 454–472. ◆



The development of a time-based probabilistic sinkhole prediction method for coal mining in the Witbank and Highveld coalfields

J.N. van der Merwe¹

Affiliation:

¹Visiting Professor, School of Mining Engineering, University of the Witwatersrand.

Correspondence to:

J.N. van der Merwe

Email:

nielen@stablestrata.com

Dates:

Received: 15 May 2019

Revised: 1 May 2020

Accepted: 20 Jun. 2020

Published: June 2020

How to cite:

van der Merwe, J.N.
The development of a time-based probabilistic sinkhole prediction method for coal mining in the Witbank and Highveld coalfields. The Southern African Institute of Mining and Metallurgy

DOI ID:

<http://dx.doi.org/10.17159/2411-9717/752/2020>

ORCID ID:

J.N. van der Merwe
<https://orcid.org/0000-0002-3709-5520>

Synopsis

There is a growing need for a method to predict sinkhole occurrence. The paper describes the development of a method to predict the occurrence of sinkholes due to mining, caused by the progressive collapse of underground openings. The shape of the collapse cavity is assumed to be conical. If the top of the cavity reaches or extends beyond the base of weathering, sinkhole development is likely. Progression of the collapse may be terminated by wedging out of the cavity, choking by bulking of the collapsed material, or the presence of a strong layer between the mining horizon and the base of the weathered material. The likelihood of failure of the strong layers is evaluated as a probability of failure based on the frequency distribution of tensile strength derived from more than 800 tests on sandstone samples from the industry. Time is brought into the equation by including the rate at which bord widths increase. As the bords increase, the probability of failure of the strong layers increases. The end result is a method on which to base the probability of sinkhole occurrence with respect to time.

Keywords

sinkhole, collapse cavity, time, bulking, wedging, probability of failure.

Introduction

There is growing concern worldwide about the unexpected appearance of vertical-sided sinkholes, even to the extent where more than one reality television series has recently been devoted to the topic. Well-known examples include the cities of Paris and Rome, certain areas of Wales and England, and the USA.

Sinkholes may be caused by a number of factors, one of which is mining. This paper is concerned with mining-related sinkholes. Mining may result in two main types of surface disturbance, the first of which is shallow trough-shaped subsidence caused by high-extraction mining (in which case the overburden rock is allowed to collapse) or collapse of the support pillars. The second is vertical-sided, deeper sinkholes that may have catastrophic consequences.

The latter phenomenon is the subject of this paper. These sinkholes are caused by progressive collapse of the roof rocks, which may in some cases migrate to the surface, resulting in a sinkhole. It is known that the sinkholes seldom appear at the time of mining. There is a delay that can span several decades or even several centuries, such as the sinkholes in Rome and Paris that are caused by mining two thousand years ago.

The typical profile of a sinkhole-prone area is one where underground mining was by bord and pillar methods and where the mining was shallow, typically less than 30 m below surface.

Worldwide, there are very few examples of sinkholes appearing where mining was deeper than 30 m. In several countries it has become a norm to apply a safety sinkhole-prone of 2 and then to regard areas where mining was less than 60 m deep, as sinkhole-prones. The approach in typical surface disturbance risk assessments is to regard areas where mining was deeper than 60 m as safe from sinkhole risk, and then either declare shallower mining areas as definite risk areas or embark on more detailed investigations.

Over the years, methods to evaluate mining-related sinkhole risk have been developed, but the existing models have two important shortcomings: they result in an evaluation that is either positive or negative without addressing the probability of occurrence of sinkholes, and they do not address the issue of time.

This paper describes the development of a method that attempts to overcome these two shortcomings.

Previous models

Over the years, a number of sinkhole prediction methods have been developed. In this section a number of representative basic methods are briefly discussed. This is by no means a comprehensive discussion of previous work – rather, the papers selected are considered to be representative of certain approaches to the problem.

Depth as a norm

This very basic method is based on observations worldwide that sinkholes very rarely develop in areas

The development of a time-based probabilistic sinkhole prediction method for coal mining

where the depth of the mining horizon exceeds 30 m. To be safe, that depth was doubled to 60 m, and areas where the minimum mining depth was greater than that were considered to be stable and the rest as sinkhole-prone. Another interpretation is that where the mining depth was less than 60 m, further investigation is required, while for the deeper areas no risk is foreseen. This very basic approach does not consider the mechanism of sinkhole development beyond that it is the end result of progressive roof collapse.

Singh (2000) described sinkholes in a number of countries and developed an equation that related the maximum mining depth at which sinkholes can appear to the ratio of overburden depth to mining height. However, the data included sinkholes caused by soil erosion along fault planes (*i.e.* not directly related to underground overburden collapse) and the equation does not take the depth of weathering into account.

Canbulat *et al.* (2017) reported that in Australia the majority of sinkholes appeared at mining depths from 10 to 15 m, the average depth being 15.9 m. Only 23 of the recorded cases (10% of the total) occurred for depths greater than 30 m.

There appears to be general consensus that sinkhole occurrence is limited to shallow mining depths, generally less than 60 m.

Stability graph method

This method, initially developed for caving mining, is described in Potvin, Hudyma, and Miller (1988). It has also been used for sinkhole prediction as the mechanism of roof collapse is common to both. The method essentially rests on the size of the opening underground, which is then compared to the critical size for rock quality. The size of the opening is standardized as the hydraulic radius, which is the circular equivalent of any shape of opening. The rock quality is determined by a modified Rock Mass Rating and the critical size is determined empirically by considering a large number of case histories where collapse did or did not occur.

The method therefore takes cognisance of the size of the opening as well as rock quality (while not directly allowing for layers of different rock quality), but does not address time or the probability of failure. It also stops at the point where the immediate roof does or does not collapse and it does not explicitly address the progression of the collapse.

Methods based on the mechanism of failure and progression of collapse

Canbulat *et al.* (2002) described a method to predict the

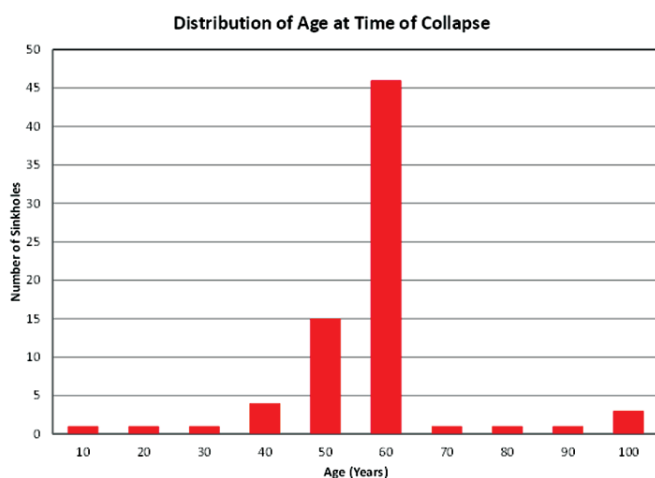


Figure 1 – Incubation time for sinkhole occurrence, based on data in Dyne (1998)

maximum height of roof collapse based on the bulking factor of the collapsed material, the mining height, and bord width. They used a cylindrical model for the collapse cavity. Their method included the possible arresting capability of strong layers in the overlying rock mass, but it was based on the behaviour of a clamped beam as opposed to a plate. As with the other methods described here, there was no consideration of time or the probability of occurrence.

Time of collapse

Dyne (1998) analysed the incubation time of sinkholes treated in a three-year period in Pennsylvania, USA. Based on that data, Figure 1 shows that the most frequent incubation time for the study area was 60 years. Although no attempt was made to develop a method to predict the time of occurrence, the data illustrates that there is a time delay between mining and sinkhole appearance.

Probabilistic approach

Canbulat *et al.* (2017) describe a stochastic method to determine the likelihood of sinkhole occurrence. However, the method does not take the arresting possibility of strong layers in the overburden or time into account, and is fundamentally based on the bulking mode of termination only for a cylindrical shape of the roof collapse.

Proposed methodology

The fundamental methodology that is proposed in this paper is to base the collapse model on a conical shape, and if the height of the collapse cavity reaches or exceeds the weathered rock material, a sinkhole is considered possible. The possible arresting of sinkhole development by strong layers in the overburden is then considered and the probability of collapse is determined based on the distribution of tensile strength of the strong layers. Finally, time is taken into account by incorporating the time-related increase in bord width due to pillar sidewall scaling. The end result is then the determination of the probability of sinkhole occurrence as a function of time.

The progression of the collapse cavity is then terminated by one of two possible mechanisms, namely wedging out due to the conical shape or choking of the cavity due to bulking of the collapsed material.

Figure 2 shows six possible outcomes. Note that the weathered zone is supplemented by a 'safety net', based on the level of confidence in the geological data. The less the confidence, the greater the safety net that should be applied. In the diagram, cases 1 to 3 relate to the wedging mechanism of termination and cases 4 to 6 to the bulking mechanism if it occurs prior to wedging out.

The first step in the process is to determine the maximum height of the collapse cavity, using the equations supplied in van der Merwe (2018). They are repeated here for convenience. The concept and terminology are explained in Figure 3.

For the bulking mechanism,

$$K(\text{Volume } A) = \text{Volume } A + \text{Volume } B + \text{Volume } C \quad [1]$$

or

$$K = 1 + \frac{\text{Volume } B + \text{Volume } C}{\text{Volume } A} \quad [2]$$

where K is the bulking factor.

Then,

$$\begin{aligned} \text{Volume } A &= \frac{1}{3} \left[\frac{\pi (fD_B)^2}{4} z_m - \frac{\pi D_u^2}{4} (z_m - z) \right] \\ &= \frac{\pi}{12} [(fD_B)^2 z_m - D_u^2 (z_m - z)] \end{aligned} \quad [3]$$

The development of a time-based probabilistic sinkhole prediction method for coal mining

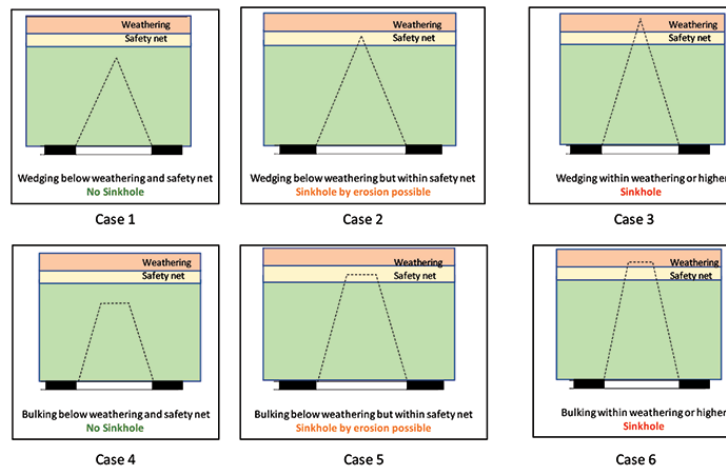


Figure 2—Six possible outcomes for the position of the top of the collapse cavity

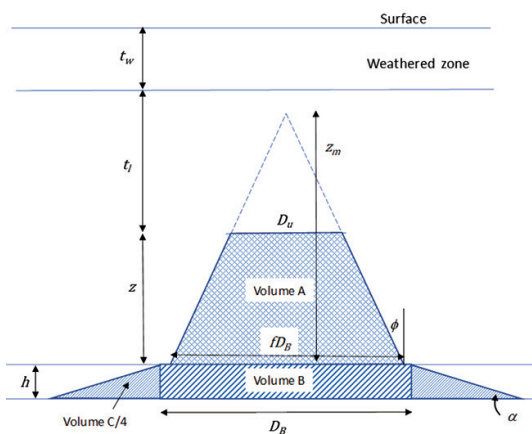


Figure 3—Simplified cross-section through a collapse cavity, illustrating the terminology used for the determination of the maximum height of the cavity (after van der Merwe, 2018)

$$D_u = fD_B - 2z \tan \phi \quad [4]$$

where

f = ratio of bottom of sinkhole diameter to bord width (*i.e.* for sinkhole diameter equal to intersection width, $f = 1.414$)

D_B = bord width

z = height of choked volume

z_m = maximum height of cavity when it wedges out

D_u = diameter of top of choked cavity

ϕ = caving angle, measured off the vertical

$$\text{Volume B} = hD_B^2 \quad [5]$$

where h = mining height

$$\text{Volume C} = 4 \left(\frac{1}{2} h^2 D_B \cot \alpha \right) = 2h^2 D_B \cot \alpha \quad [6]$$

where α = angle of repose of collapsed material measured from the horizontal.

Substitution of Equations [3] to [6] into [2] results in a cubical expression for z , which is easiest found by iteration.

Also,

$$z_m = \frac{fD_B}{2 \tan \phi} \quad [7]$$

The maximum height of the cavity is then the smallest value of z obtained with Equations [2] to [6] – termination by choking, or z_m obtained with Equation [7] – termination by wedging out.

If the outcome of this first step results in either case 1 or case

6 shown in Figure 3, sinkhole development is considered unlikely and further investigation is not required. However, in all other cases there is the possibility that the cavity may be terminated by the presence of a strong layer in the overburden, and further investigation is required.

Failure mode of strong layer

A strong layer in the overburden can conceptually fail in either tension or shear. For shear failure to occur, the shear stress around the edges of a circular disc must be greater than the shear strength.

The shear stress is given by

$$\tau = \frac{\gamma D}{4} \quad [8]$$

In practical terms this means that for a plate of diameter 20 m and loaded by the dead weight of 60 m of overburden rock (*i.e.* beyond the extremes of common coal mining configurations), the shear stress will be 7.5 MPa. This is less than commonly quoted values of shear strength of 15 MPa given by van der Merwe and Madden (2010) or 35 MPa according to Geertsema (2000). The shear mode of failure can thus be ignored for this investigation.

For the tensile failure mechanism, the strong layer is assumed to behave similar to a clamped plate, not a beam as previously used. The beam analogy is valid for a rectangular opening with length much greater than width. The top of a collapse area has been seen to be circular or elliptical in shape and therefore the plate analogy is more acceptable. The tensile stress developed around the edges of a uniformly loaded clamped circular plate is given by

$$\sigma_t = \frac{3\gamma D^2}{16t^2} \quad [9]$$

where

γ = uniformly distributed load

D = diameter of plate

t = thickness of plate

If the tensile strength of the material is denoted by σ_m , the tensile safety factor is

$$SF_t = \frac{16t^2 \sigma_m}{3\gamma D^2} \quad [10]$$

From a deterministic perspective, failure will occur if $SF_t < 1$.

Identification of strong layer

The next step is to determine which of the overburden layers can be considered as 'strong'. Typical coal mining overburden in the Witbank coalfield consists of sedimentary rock types, mainly sandstone, shale, mudstone, siltstone, and laminated shale/sandstone layers.

The development of a time-based probabilistic sinkhole prediction method for coal mining

The results of a great number of tensile strength tests based on the Brazilian test method (UTB) were collected from rock engineers in the Witbank coalfield. The results were loosely grouped as sandstone, shale, coal, and laminated material. It was found that the frequency distributions could be described as lognormal. The results are summarized in Table I.

The cumulative frequency distributions are shown in Figure 4.

It is clear from Table I and Figure 4 that there are distinct differences between the tensile strengths of the different rock types, and that the sandstone and laminated rock are significantly stronger than the others. The sandstone only can then be regarded as the strong layer. The laminated layers should not be included due to the rapid weathering of the shale laminations.

It was found that the cumulative distribution of the tensile strength of sandstone can be expressed by the simplified equation:

$$P_f = \exp(-90.21\sigma_t^{-3.03}) \quad [11]$$

where σ_t is the tensile strength in MPa.

Probability of failure

Equation [11] also expresses the probability of failure of the strong layer. Therefore, instead of calculating a safety factor for the strong layer, the tensile stress can now be used to determine the probability of failure.

The equation for the tensile stress is given by Equation [9].

For clarity, the elements of Equation [9] are given by the following equations. The terminology is explained in Figure 5.

$$\gamma = \rho g H_d \quad [12]$$

where H_d is the depth below surface of the base of the strong layer.

$$D = B - 2H_p \tan\phi \quad [13]$$

where

B = diameter of the bottom of the collapse cavity (typically taken as the intersection width)

ϕ = caving angle measured off the vertical

HP = parting thickness between the roof of the excavation and the bottom of the strong layer.

Probability of sinkhole occurrence

There will invariably be more than one strong layer. A sinkhole can appear only if all the strong layers fail. Therefore, the probability of failure of the system, P_s , is the product of all the individual probabilities of failure. Mathematically,

$$P_s = P_1 \cdot P_2 \cdot P_3 \dots \dots P_n \quad [14]$$

where P_1 to P_n are the probabilities of failure of each of the individual strong layers.

Note that this procedure is dominated by the strongest of the strong layers. A layer with a very high probability of failure (*i.e.* close to 1.0) will not change the outcome, while layers with very low probabilities of failure (close to zero) will have a meaningful impact. If there is only a single layer that does not fail, the system will not fail either and no sinkhole will occur.

This is a simplified approach, as even the weakest of layers will contribute to some extent to stability. This is not taken into account in this proposed procedure as it has been shown that the tensile strength of the sandstone is dominant, and a conservative approach was followed in the investigation. The weaker rock types are also more susceptible to rapid weathering.

The approach can easily be extended to the other rock types by substituting Equation [11] with an equation which is

appropriate for that particular rock type. The rest of the procedure will not require modification.

Extension of the procedure to include time

There are at least two mechanisms that will weaken the system over time. One is weathering of the rock, which will decrease the tensile strength, and the second is widening of the base of the collapse cavity, which will increase the tensile stress of the overlying layers.

Judging from observation of exposed borehole core, rock types like shale or mudstone weather fairly quickly, but sandstone weathering is a much slower process. Weathering also affects one layer at a time – only the exposed layer at the top of the collapse cavity.

Widening of the bord width by sidewall scaling is a much faster process and it affects all the overlying layers at the same time. It is therefore regarded as the dominant mechanism by which the probability of failure will increase over time.

The rate at which the sidewalls scale has been quantified, and by implication the rate at which the probability of failure increases over time can also be quantified. According to van der Merwe (2016) the amount by which pillar width decreases over time, which is the same as the amount by which the bord width increases, is given by

$$d_T = mh^x T^{1-x} \quad [15]$$

Table I

UTB results for different rock types

	Number of samples	Median (MPa)	Mean (MPa)	Std. deviation (MPa)
Coal	47	1.42	1.64	0.99
Shale	118	4.48	4.63	2.13
Laminated	33	5.99	7.19	3.47
Sandstone	2638	6.31	6.72	3.47

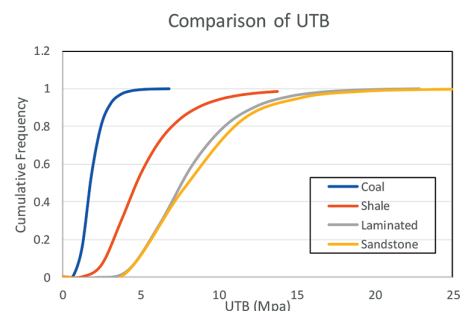


Figure 4—Cumulative frequency distributions for different rock types

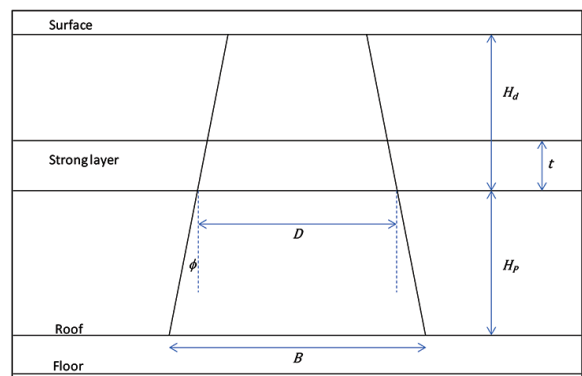


Figure 5—Cross-section through collapse cavity

The development of a time-based probabilistic sinkhole prediction method for coal mining

where

h = mining height

T = time since mining

m = constant, 0.1799 for the Witbank and Highveld coal seams (excluding the No. 5 Seam)

x = constant, 0.7549 for the Witbank and Highveld coal seams (excluding the No. 5 Seam).

The probability of failure at any given point in time can now be obtained by substituting D_B by D_B+d_T in the foregoing equations.

Practical considerations

The procedure outlined in the foregoing paragraphs is sensitive to all the input parameters. For a more complete discussion of the impact of variability of the input parameters, refer to van der Merwe (2018).

There are two classes of input parameters, namely the controllable and uncontrollable ones. At the planning and mining phases, the bord width is the main controllable parameter while the mining height is controllable to some extent.

The remaining parameters are not controllable. In this class, some are easier to determine than others. The lithology is relatively simple to define, although the level of detail contained in older borehole descriptions is not always adequate. The bulking factor and caving angle are more difficult to determine but not impossible. It is essential that local databases should be set up and maintained.

It was shown in Figure 4 that the laminated rock has tensile strength equivalent to that of sandstone, but due to the rapid weathering nature of the shales, should not be considered as strong layers in the context of this type of investigation. Cross-bedded sandstone should also be viewed with suspicion.

Application to case study

The procedure described in the paper was applied to a case study to demonstrate its applicability. The name of the mine is withheld for confidentiality.

At Mine A, two previously mined areas, Sites 1 and 2, were evaluated for the potential of sinkhole occurrence. Table II summarizes the information that was used as input for the conical collapse model at the time, without taking the effect of strong layers or time into account.

The cases are seen to be similar from a mining perspective. In both cases, the potential mode of termination was found to be bulking; the height of the cavity, 25.1 m, reached the weathered zone and the verdict was that sinkholes were likely to occur. The same mitigation methods were then applied to the two areas.

The procedure dealing with the impact of strong layers described in this paper was then applied to the two cases. The base depth and thickness of sandstone in the two areas are indicated in Table III.

Table III shows that although the base depths of the sandstones are similar, the thicknesses are different. It was then found that for Site 1, the probability of sinkhole occurrence at the time of mining was 0.5% while for Site 2 it was 25.3%. The progressions of the probabilities of occurrence over a period of 250 years are shown in Figure 6.

Figure 6 indicates that for Site 2, the probability of occurrence of 50% is reached after 39 years. At that time, the probability of occurrence for Site 1 is only approximately 8%. Taking this additional information into account, it is clear that Site 2 requires much more urgent mitigation and perhaps even a different approach than Site 1.

This case study also highlights the importance of detailed description of borehole logs.

Restrictions and further development

Input accuracy

The most important restrictions to the application of the procedure outlined here relate to the availability and accuracy of the input parameters. This includes the caving angle, bulking factor, the mining geometry, and the borehole log descriptions.

With increasing emphasis on the time-related impact of mining on the environment there is a growing need to evaluate older mining areas for sinkhole potential. In the older areas, where mining was done up to 100 years or more ago, the data is especially suspect. At the time of mining the emphasis on information gathering was on the thickness and depth of economical coal seams, with sparse attention paid to the detail of the overburden rock. In fact, some logs exist that contain three entries only, namely soil, rock, and coal. The mine plans can also sometimes contain inaccurate information.

In cases where sinkhole evaluation of older areas is required now, there are no short cuts to determine more suitable input information and new drilling is required. Where this is to be done, it is strongly advocated that the visual descriptions be supplemented with wireline logging and geotechnical evaluation. The lessons from the past should be heeded and as much information as possible should be gathered when the opportunity arises.

Table II

Input parameters for Mine A

Mine A	Site 1	Site 2
Mining depth (m)	28	28
Depth of weathering (m)	10	10
Bord width (m)	7.5	7.5
Mining height (m)	2.7	2.7
Angle of repose off horizontal (°)	15	15
Caving angle off horizontal (°)	85	85
Bulking factor	1.25	1.25
Ratio of diameter to bord width	1	1
Safety net (m)	2	2

Table III

Characteristics of sandstone at sites 1 and 2

	Site 1		Site 2	
	Base depth (m)	Thickness (m)	Base depth (m)	Thickness (m)
Layer 1	14	0.7	15	0.5
Layer 2	17	3	16	0.8
Layer 3	19	1.9	20	3
Layer 4	23	3.8	21	0.7

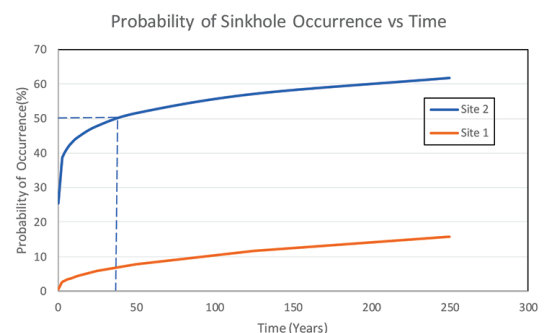


Figure 6—Progression of probability of sinkhole occurrence over a period of 250 years

The development of a time-based probabilistic sinkhole prediction method for coal mining

Rate and extent of pillar scaling

The method is also sensitive to the rate and extent of pillar scaling. This should be re-evaluated at suitable times. It is not only applied to the temporal development of sinkhole occurrence, but is also used for the prediction of the time of failure of coal pillars.

It is also logical that the presence of roof collapse debris in the cavity will restrict the pillar scaling, and *vice versa*. In this paper, quantification of that impact is not attempted. However, it should be borne in mind that for pillar scaling to take place, it is not necessary for the fractured pillar material to be completely detached from the pillars. There just needs to be a fracture.

On the other side of the equation, the bulked and collapsed material will undergo slight compression due to the weight of the overlying collapsed material and this will reduce the bulking factor. This mechanism counteracts the omission of the effect of bulking of the pillar debris, at least to some extent.

The presence of debris can only slow the process down, not terminate it, and therefore not taking it into account at this stage results in a conservative view. This is an area that should be identified for further development of the methodology described here.

Multiple seam mining

The process outlined here is based on the consideration of mining on a single seam only. In the case of multiple seam mining the bottom seam should be analysed first. If it is found that the cavity on the bottom seam does not reach the upper seam, the next highest seam should be analysed as an independent entity. The process should be repeated for the other overlying seams in sequence.

If the cavity on a lower lying seam does reach a higher seam, two scenarios should be investigated. If the mining layouts are not superimposed, the potential for the bottom seam cavity to result in pillar failure of the upper seam should be considered.

If the layouts were superimposed the cavity from the bottom seam will reach an intersection or bord on the upper seam. The upper seam should then be analysed with an adapted Equation [3]. A volume equal to the remaining open void from the bottom seam, V_L , should be added to the volume available for cavity growth on the upper seam.

In mathematical terms, Equation [3] should then be:

$$\text{Volume } A = \frac{\pi}{12} [(fD_B)^2 z_m - D_u^2 (z_m - z)] + V_L \quad [16]$$

Note that as the bottom seam cavity does not impact on the bord width, the equations for evaluating the stability of strong layers will not be affected.

Further development of the model

This model only recognizes the variability of a single input parameter, namely the tensile strength of sandstone layers. Canbulat *et al.* (2017) showed the benefit of a full stochastic approach to the problem, even though the impact of strong layers and the effects of time were not included in their work. The two approaches should be combined.

The resisting effects of the weaker layers should also be incorporated, as should the rate of chemical weathering of the overburden rock types. These two parameters are to some extent mutually compensating, as weathering will reduce the strength and thereby increase the probability of failure, while taking the effect of weak layers into account will reduce the probability of failure.

The extensions will no doubt result in a much more complex model, but certainly not one beyond the reach of commonly available methods of calculation.

Conclusions

The process described in the paper is a further development of the existing models to evaluate the potential for sinkhole occurrence due to shallow mining. The first model that was used was based on the concept of the termination of cavity development by choking of a cylindrical cavity due to bulking of the collapsed roof material. This was subsequently extended to a cavity of conical shape and a second mechanism of termination was introduced, namely wedging out of the cavity.

This model extends the conical model by recognizing the potentially stabilizing effect of strong layers in the overburden on a probabilistic basis. By incorporating the temporal widening of the bord width due to pillar scaling, the probability of sinkhole occurrence is linked to time.

It was shown by the application of the method to a case study that the procedure results in more useful information to evaluate the potential for sinkhole occurrence.

In principle the method in itself is not restricted to coal mining, but the constants that were used for some of the variables restrict the detailed method of calculation to the Witbank and Highveld coalfields with the exception of the No. 5 Seam. By substituting the constants by appropriate ones for other coalfields and even other bord and pillar mining like chrome or platinum, the application of the model can be extended.

The model should be developed further by incorporating the variability of all the input parameters. This will require more data to be gathered and the accuracy of data to be improved.

Acknowledgements

Mr Dave Neal is thanked for his persistent encouragement to develop the model and for gathering the data of UTB tests from all available sources in the industry.

Rock engineers from the mines in the Witbank and Highveld coalfields are acknowledged for sharing the data.

Ms Jeanne Walls reviewed the paper prior to submission.

The paper is published with the permission of South32.

References

- CANBULAT, I., ZHANG, C., BLACK, K., JOHNSTON, J., and McDONALD, S. 2017. Assessment of sinkhole risk in shallow coal mining. *Proceedings of the Tenth Triennial Conference on Coal Mine Subsidence: Adaptive Innovation for Managing Challenges*, Kirkton Park, Pokolbin, 5-7 November 2017. Mine Subsidence Technological Society, Institution of Engineers Australia, Canberra.
- CANBULAT, I., VAN DER MERWE, J.N., VAN ZYL, M., WILKINSON, A., DAEHNKE, A., and RYDER, J. 2002. Task 6.9.1: The development of techniques to predict and manage the impact of surface subsidence. Coaltech, Johannesburg.
- DYNE, L.A. 1998. The prediction and occurrence of chimney subsidence in southwestern Pennsylvania. MSc thesis, Virginia Polytechnic Institute and State University, Blacksburg, VA.
- GEERTSEMA, A.J. 2000. The engineering characteristics of important southern African rock types with emphasis on shear strength of concrete dam foundations. WRC Report No 453/1/00: Water Research Commission, Department of Water Affairs, Pretoria.
- POTVIN, Y., HUDYMA, M., and MILLER, H.D.S. 1988. The stability graph method for open stope design. *Proceedings of the 90th Canadian Institute of Mining AGM*, May 1988. CIM, Montreal. Paper no. 44.
- SINGH, K.B. 2000. Causes and remedial actions of pot-hole subsidence due to coal mining. *Journal of Scientific & Industrial Research*, India, vol. 59, April. pp. 280-285.
- VAN DER MERWE, J.N. 2016. A three-tier method of stability evaluation for coal mines. *Journal of the Southern African Institute of Mining and Metallurgy*, vol. 116, no. 12. <http://dx.doi.org/10.17159/2411-9717/2016/v116n12a14>
- VAN DER MERWE, J.N. 2018. Effects of coal mining on surface topography in South Africa — updates and extensions. *Journal of the Southern African Institute of Mining and Metallurgy*, vol. 118, no. 7. <http://dx.doi.org/10.17159/2411-9717/2018/v118n7a11> ◆

NATIONAL & INTERNATIONAL ACTIVITIES

2021

9–June 2021 — Diamonds – Source to Use – 2020 Conference 2021

'Innovation and Technology'

The Birchwood Hotel & OR Tambo Conference Centre, Johannesburg, South Africa

Contact: Camielah Jardine

Tel: +27 11 834-1273/7

Fax: +27 11 838-5923/833-8156

E-mail: camielah@saimm.co.za

Website: <http://www.saimm.co.za>

13–16 July 2021 — Copper Cobalt Africa The 10th Southern African Base Metals Conference 2021

Avani Victoria Falls Resort, Livingstone, Zambia

Contact: Camielah Jardine

Tel: +27 11 834-1273/7

Fax: +27 11 838-5923/833-8156

E-mail: camielah@saimm.co.za

Website: <http://www.saimm.co.za>

29–30 July 2021 — 5th Mineral Project Valuation Colloquium 2021

Glenhove Events Hub, Melrose Estate, Johannesburg, South Africa

Contact: Gugu Charlie

Tel: +27 11 834-1273/7

Fax: +27 11 838-5923/833-8156

E-mail: gugu@saimm.co.za

Website: <http://www.saimm.co.za>

18–20 August 2021 — Wold Gold Conference 2021

Misty Hills Conference Centre, Muldersdrift, Johannesburg, South Africa

Contact: Camielah Jardine

Tel: +27 11 834-1273/7

Fax: +27 11 838-5923/833-8156

E-mail: camielah@saimm.co.za

Website: <http://www.saimm.co.za>

29 August–2 September 2021 — APCOM 2021 Minerals Industry 4.0 Conference

'The next digital transformation in mining'

Misty Hills Conference Centre, Muldersdrift, Johannesburg, South Africa

Contact: Camielah Jardine

Tel: +27 11 834-1273/7

Fax: +27 11 838-5923/833-8156

E-mail: camielah@saimm.co.za

Website: <http://www.saimm.co.za>

21–22 September 2021 — 5th Young Professionals Conference 2021

'A Showcase of Emerging Research and Innovation in the

Minerals Industry'

The Canvas, Riversands, Fourways, South Africa

Contact: Camielah Jardine

Tel: +27 11 834-1273/7

Fax: +27 11 838-5923/833-8156

E-mail: camielah@saimm.co.za

Website: <http://www.saimm.co.za>

4–6 October 2021 — 8th International PGM Conference 2021

'PGMs – Enabling a cleaner world'

South Africa

Contact: Camielah Jardine

Tel: +27 11 834-1273/7

Fax: +27 11 838-5923/833-8156

E-mail: camielah@saimm.co.za

Website: <http://www.saimm.co.za>

18–20 October 2021 — South African Rare Earths International Conference 2021

'Driving the future of high-tech industries'

Swakopmund Hotel And Entertainment Centre, Swakopmund, Namibia

Contact: Camielah Jardine

Tel: +27 11 834-1273/7

Fax: +27 11 838-5923/833-8156

E-mail: camielah@saimm.co.za

Website: <http://www.saimm.co.za>

26–27 October 2021 — SAMCODES Conference 2021

'Good Practice and Lessons Learnt'

Industry Reporting Standards

Glenhove Events Hub, Melrose Estate, Johannesburg, South Africa

Contact: Camielah Jardine

Tel: +27 11 834-1273/7

Fax: +27 11 838-5923/833-8156

E-mail: camielah@saimm.co.za

Website: <http://www.saimm.co.za>

9–11 December 2020 — Massmin 2020 Eight International Conference & Exhibition on Mass Mining Virtual Conference 2020

Santiago, Chile, Contact: J.O. Gutiérrez

Tel: (56-2) 2978 4476

Website: www.massmin2020.com

2022

17–24 June 2022 — NAT2020 North American Tunneling Conference

Philadelphia

Website: <http://www.natconference.com>

Due to the current COVID-19 pandemic our 2020 conferences have been postponed until further notice. We will confirm new dates in due course.

Company affiliates

The following organizations have been admitted to the Institute as Company Affiliates

3M South Africa (Pty) Limited	Expectra 2004 (Pty) Ltd	MSA Group (Pty) Ltd
AECOM SA (Pty) Ltd	Exxaro Coal (Pty) Ltd	Multotec (Pty) Ltd
AEL Mining Services Limited	Exxaro Resources Limited	Murray and Roberts Cementation
African Pegmatite (Pty) Ltd	Filtaquip (Pty) Ltd	Nalco Africa (Pty) Ltd
Air Liquide (Pty) Ltd	FLSmith Minerals (Pty) Ltd	Namakwa Sands(Pty) Ltd
Alexander Proudfoot Africa (Pty) Ltd	Fluor Daniel SA (Pty) Ltd	Ncamiso Trading (Pty) Ltd
AMEC Foster Wheeler	Franki Africa (Pty) Ltd-JHB	New Concept Mining (Pty) Limited
AMIRA International Africa (Pty) Ltd	Fraser Alexander (Pty) Ltd	Northam Platinum Ltd - Zondereinde
ANDRITZ Delkor(pty) Ltd	G H H Mining Machines (Pty) Ltd	Opermin Operational Excellence
Anglo Operations Proprietary Limited	Geobrug Southern Africa (Pty) Ltd	OPTRON (Pty) Ltd
Anglogold Ashanti Ltd	Glencore	Paterson & Cooke Consulting Engineers (Pty) Ltd
Arcus Gibb (Pty) Ltd	Hall Core Drilling (Pty) Ltd	Perkinelmer
ASPASA	Hatch (Pty) Ltd	Polysius A Division Of Thyssenkrupp Industrial Sol
Atlas Copco Holdings South Africa (Pty) Limited	Herrenknecht AG	Precious Metals Refiners
Aurecon South Africa (Pty) Ltd	HPE Hydro Power Equipment (Pty) Ltd	Ramika Projects (Pty) Ltd
Aveng Engineering	Immersive Technologies	Rand Refinery Limited
Aveng Mining Shafts and Underground	IMS Engineering (Pty) Ltd	Redpath Mining (South Africa) (Pty) Ltd
Axiom Chemlab Supplies (Pty) Ltd	Ingwenya Mineral Processing (Pty) Ltd	Rocbolt Technologies
Axis House Pty Ltd	Ivanhoe Mines SA	Rosond (Pty) Ltd
Bafokeng Rasimone Platinum Mine	Joy Global Inc.(Africa)	Royal Bafokeng Platinum
Barloworld Equipment -Mining	Kudumane Manganese Resources	Roytec Global (Pty) Ltd
BASF Holdings SA (Pty) Ltd	Leco Africa (Pty) Limited	RungePincockMinarco Limited
BCL Limited	Leica Geosystems (Pty) Ltd	Rustenburg Platinum Mines Limited
Becker Mining (Pty) Ltd	Longyear South Africa (Pty) Ltd	Salene Mining (Pty) Ltd
BedRock Mining Support Pty Ltd	Lull Storm Trading (Pty) Ltd	Sandvik Mining and Construction Delmas (Pty) Ltd
BHP Billiton Energy Coal SA Ltd	Maccaferri SA (Pty) Ltd	Sandvik Mining and Construction RSA(Pty) Ltd
Blue Cube Systems (Pty) Ltd	Magnetech (Pty) Ltd	SANIRE
Bluhm Burton Engineering Pty Ltd	MAGOTTEAUX (Pty) Ltd	Schauenburg (Pty) Ltd
Bond Equipment (Pty) Ltd	Malvern Panalytical (Pty) Ltd	Sebilo Resources (Pty) Ltd
Bouygues Travaux Publics	Maptek (Pty) Ltd	SENET (Pty) Ltd
CDM Group	Maxam Dantex (Pty) Ltd	Senmin International (Pty) Ltd
CGG Services SA	MBE Minerals SA Pty Ltd	Smec South Africa
Coalmin Process Technologies CC	MCC Contracts (Pty) Ltd	Sound Mining Solution (Pty) Ltd
Concor Opencast Mining	MD Mineral Technologies SA (Pty) Ltd	SRK Consulting SA (Pty) Ltd
Concor Technicrete	MDM Technical Africa (Pty) Ltd	Time Mining and Processing (Pty) Ltd
Council for Geoscience Library	Metalock Engineering RSA (Pty)Ltd	Timrite Pty Ltd
CRONIMET Mining Processing SA Pty Ltd	Metorex Limited	Tomra (Pty) Ltd
CSIR Natural Resources and the Environment (NRE)	Metso Minerals (South Africa) Pty Ltd	Ukwazi Mining Solutions (Pty) Ltd
Data Mine SA	Micromine Africa (Pty) Ltd	Umgeni Water
Digby Wells and Associates	MineARC South Africa (Pty) Ltd	Verni Speciality Construction Products (Pty) Ltd
DRA Mineral Projects (Pty) Ltd	Minerals Council of South Africa	Webber Wentzel
DTP Mining - Bouygues Construction	Minerals Operations Executive (Pty) Ltd	Weir Minerals Africa
Duraset	MineRP Holding (Pty) Ltd	Welding Alloys South Africa
Elbroc Mining Products (Pty) Ltd	Mintek	Worley
eThekwini Municipality	MIP Process Technologies (Pty) Limited	
Ex Mente Technologies (Pty) Ltd	MLB Investment CC	
	Modular Mining Systems Africa (Pty) Ltd	

APCOM 2021

MINERALS INDUSTRY 4.0



The next digital
transformation
in mining

29 AUGUST - 2 SEPTEMBER 2021

MISTY HILLS CONFERENCE CENTRE
MULDRSDRIFT, JOHANNESBURG,
SOUTH AFRICA

APCOM (Applications of Computers and Operations Research in the Minerals Industries) is a series of well-established, high-quality international scientific conferences which was started in the early 1960s with the aim of sharing technological advances by engineers and computer scientists in all fields relevant to the mining industry. The APCOM events have evolved to become a major driver of innovation in the minerals industry, and over the years, many breakthrough innovations, such as geostatistics and mining process optimization, have been initially discussed at or originated from the APCOM conferences. One of the success factors of APCOM is the intensive, high-quality dialogue that it promotes between industry and academia. Thanks to the personal commitments of APCOM's loyal participants and supporters, the symposia continue to be a thriving success.

The APCOM 2021 Conference, the 40th in the series, will be held at Misty Hills, Muldersdrift, South Africa from 29 August – 2 September 2021. Nestled in the foothills of the Swartkop Mountains on the threshold of the beautiful Kromdraai Valley in Muldersdrift, Misty Hills is one of the most popular hotel and conference venues in Johannesburg. This charming stone-built hotel embodies the ethos of Africa. Set in more than 60 acres of lush botanical gardens, Misty Hills is the ideal venue for functions, conferences, exhibitions, product launches, team-building, getaways, and events. Come and experience the splendour of rich African hospitality in the heart of Gauteng. Johannesburg. An optional tourist visit is planned to the nearby Pilanesberg National Park which presents an opportunity to view the 'Big Five'.

FOR FURTHER INFORMATION, CONTACT:

Camielah Jardine,
Head of Conferencing

E-mail: camielah@saimm.co.za
Web: www.saimm.co.za



SAIMM
THE SOUTHERN AFRICAN INSTITUTE
OF MINING AND METALLURGY

SOUTHERN
AFRICAN

RARE EARTHS

INTERNATIONAL CONFERENCE 2021

18-20 OCTOBER 2021

SWAKOPMUND HOTEL AND ENTERTAINMENT CENTRE,
SWAKOPMUND, NAMIBIA

Driving the future
of high-tech
industries



ABOUT THE CONFERENCE

The global demand for rare earth elements (REEs) and their alloys has increased enormously in the last few decades. REEs are critical materials in high-technology applications due to their unique chemical, catalytic, electrical, magnetic, and optical properties. In particular, REEs are used in emerging and niche technologies such as medical devices, electric vehicles, energy-efficient lighting, wind turbines, rechargeable batteries, catalytic converters, flat screen televisions, mobile phones, and disk drives. In fact, the 4IR-driven digital revolution will not be possible without the critical rare REEs.

The supply security of rare earth metals is of global concern. The need to diversify the supply of REEs thus creates significant opportunities for southern Africa to contribute to the global supply. In fact, as one of the regions with large REE resources, southern Africa can exploit this window of opportunity and significantly contribute to the sustainable supply of these high-tech materials.

The need to fully participate along the REE value chain has also inspired interest in developing downstream capacity for refining, through the Southern African Centralized Rare Earth Refinery (SACREF). Thus, in order to maximize value from the REEs industry in the region, further discussions on optimizing the REE value chain are needed. This conference, focusing on the optimization of the primary production and refining of rare earth metals, is designed to stimulate debate on growth, creating opportunities for the southern African rare earths industry.

**PLEASE NOTE THAT
SPONSORSHIP
OPPORTUNITIES
AND EXHIBITION
SPACE IS
AVAILABLE.**

FOR FURTHER INFORMATION, CONTACT:

Camielah Jardine,
Head of Conferencing

E-mail: camielah@saimm.co.za
Web: www.saimm.co.za



SAIMM
THE SOUTHERN AFRICAN INSTITUTE
OF MINING AND METALLURGY